博士論文

Two-dimensional Superconductivity in $BaBiO_3/BaPbO_3$ Heterostructure

（$BaBiO_3/BaPbO_3$ヘテロ構造における二次元超伝導）

河底　秀幸

Thesis

Two-dimensional Superconductivity in $BaBiO_3/BaPbO_3$ Heterostructure

Hideyuki KAWASOKO

(Supervisor: Hidenori TAKAGI)

Department of Advanced Materials Science,

School of Frontier Sciences, The University of Tokyo

Contents

Chapter 1

Introduction

In this study, we aim at enhancing superconducting properties by utilizing oxide heterostructure. First, we explain factors to determine the superconducting transition temperature. Second, the features about $BaBiO_3$ which is a target material of this work are reviewed, and the problem of disorder in $Ba(Pb_{1-x}Bi_x)O_3$ superconductors is discussed. At last, the developments of physical properties in oxide heterostructures are described as attempts to suppress the effect of disorder.

1.1 Superconductivity

Superconductivity, which is a phenomenon with zero electrical resistance and perfect diamagnetism, has provided great benefits for the condensed matter physics and human life, since H. K. Onnes discovered zero-resistance at 4.2 K in mercury (Hg) in 1911 [1].

Many important theories in condensed matter physics have been established through the researches of superconductivity, such as London theory, Ginzburg-Landau (GL) theory and Bardeen-Cooper-Schrieffer (BSC) theory [2]. The emergence of cuprate superconductors suggests that magnetic interaction between electrons is important for realizing high T_c, and accelerates the investigation about the physics of strongly correlated electrons [3, 4].

On the other hand, in the field of practical applications, superconducting materials are focused as meaningful tools. Magnets made from superconducting materials are one of the strongest electromagnets, which are used in the magnetic resonance imaging (MRI) in the medical region. Josephson junction which is the device consisted of superconductor is useful for a magnetometer, named as SQUID (superconducting quantum interference devices). If the transition temperature rises above room temperature, the zero-resistance state in superconductors will enable the electrical transmission without energy loss, which is the dream of superconductivity [5].

Therefore, the discovery of new superconductors and the enhancement of superconducting transition temperature have significant meanings for not only the progress of fundamental science but also application to the human life.

1.1.1 What Determines Superconducting T_c?

In BCS theory, the formation of cooper pairs by the attractive interaction between electrons is required in order to realize superconductivity. From the BCS framework, the superconducting transition temperature T_c is described as [6]

$$T_c = 1.14\Theta_D \exp(\frac{-1}{N(0)V}) \quad \text{(Eq.1-1)}$$

, where Θ_D is Debye temperature, $N(0)$ indicates density of state near Fermi level, and V shows the electron-phonon coupling. This equation is valid under the assumption of $N(0)V \ll 1$, which is called as a weak coupling region. In this region, high Θ_D, large $N(0)$, and strong V are needed to increase T_c.

This equation is difficult to reproduce higher T_c in materials with $N(0)V \sim 1$ which is classified as a strong coupling region. In this region of strong coupling, McMillan suggests that the equation of T_c is modified like [7]

$$T_c = \frac{\Theta_D}{1.45} \exp\left[\frac{-1.04(1+\lambda)}{\lambda - \mu^*[1+0.62\,\lambda)]}\right] \quad \text{(Eq.1-2)}$$

, where λ is described by $N(0)V$, representing the attractive interaction between electrons, while Coulomb interaction μ^* is expressed by $N(0)U_c$. U_c is named as a Coulomb pseudo-potential.

μ^* is also described like,

$$\mu^* = \frac{\mu}{1 + \mu \ln(E_F/\hbar\omega_D)} \quad \text{(Eq.1-3)}$$

, using screened electron-electron interaction $\mu = N(0)V_c$. This equation indicates that effective Coulomb interaction between electrons is reduced by the value of the denominator. That is

reflected by the difference of time scale between electron-electron interaction and electron-phonon interaction. Generally, μ^* take a value around 0.1.

On the other hand, λ is given by,

$$\lambda = \frac{N(0)\langle I^2 \rangle}{M\langle \omega^2 \rangle} \quad \text{(Eq.1-4)}$$

Here, M is the mass of ion, and I^2 is a parameter of electron-phonon scattering. ω^2 indicates the frequency of phonon.

Materials with large λ can realize high T_c, according to BCS theory. However, T_c is likely to be saturated when λ increases to ~ 1, and the instability of crystal structure emerges at $\lambda > 1$. Therefore, T_c of phonon-medicated superconductor has been considered to have an upper limit about 30 ~ 40 K, which is often called as "BCS wall".

1.1.2 Superconducting Materials

Figure 1-1 shows the history about the development of superconducting materials [8]. Since superconductivity was discovered in Hg, superconducting temperature T_c has been increasing. These superconductors in Fig.1-1 are classified by two types of materials, in term of attractive interaction which generates cooper pairs. One is electron-phonon coupling, and the other is electron-electron coupling such as antiferromagnetic interaction. This kind of magnetic coupling indicates the direct interaction between electrons which is larger than conventional phonon-mediated interaction in BCS theory. Thus, electron-electron interaction is expected to demonstrate higher T_c. In reality, superconductivity of layered cuprates and iron-pnictides is thought to be originated from electron-electron coupling, and realizes high T_c which exceeds a BCS wall, as shown in Fig. 1-1.

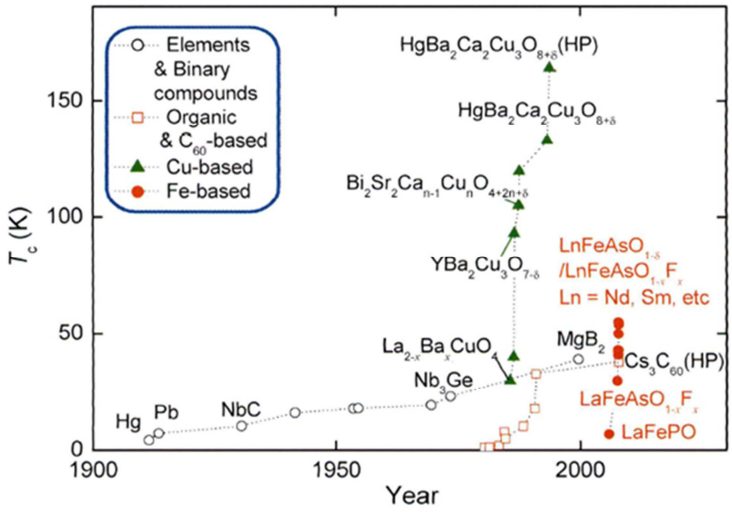

Fig. 1-1. History of superconducting temperatures [8].

In phonon-mediated superconductors, there is considered to be a limitation of BCS as described in the previous section, but some compounds show high T_c which is comparable to a BCS wall. As expressed in Eq. 1-1, high Debye temperature Θ_D and large electron-phonon interaction λ are required to demonstrate high T_c. Generally, light elements and strong covalent bonds realize high Debye temperature, resulting the enhancement of T_c. For example, light elements included MgB_2 and $(Cs_2Rb)C_{60}$ are reported to be T_c = 39 K [9] and 33 K [10], respectively.

Furthermore, T_c is anticipated to rise, with increasing λ. However, too large λ forms the electron pairs in real space, as shown in Fig. 1-2. This stabilizes charge density wave, inductive of an insulating properties. A charge order insulator $BaBiO_3$ shows superconductivity with high T_c = 33 K by K doping [11]. In this superconductor based on $BaBiO_3$, λ is in the strong coupling region [12]. This might indicate that charge order of $BaBiO_3$ is realized due to an enormously large λ. Thus, $BaBiO_3$ has a chance to exhibit higher T_c by melting a charge order without introducing disorder which is different from chemical doping.

These achievements of high T_c throw questions at the existence of a BCS wall in phonon-mediated superconductors. How much T_c of phonon-mediated superconductors can be enhanced in reality is an interesting subject for the development of superconducting materials. In this work, we attracted attentions to the system based on $BaBiO_3$ as a target to increase T_c.

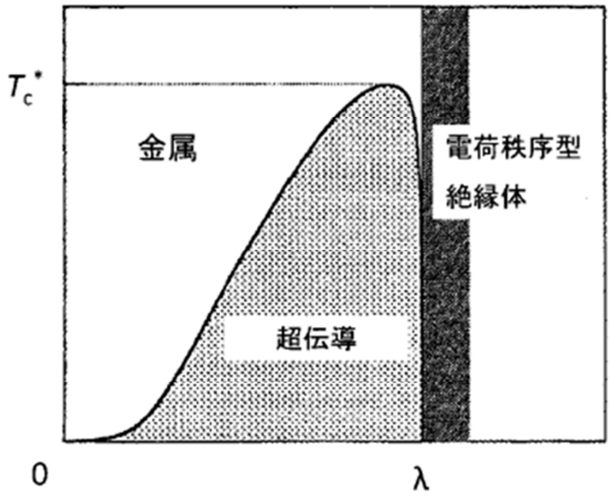

Fig. 1-2. Schematic picture about λ dependence of T_c [8]. “金属”, “超伝導”, “電荷秩序型絶縁体” indicate metal, superconductor, charge order insulator.

1.2 Solid-solution $Ba(Pb_{1-x}Bi_x)O_3$ System

In this work, we draw attention to the solid solutions of $BaBiO_3$ and $BaPbO_3$ which exhibit superconductivity. As described in the previous section, T_c of $BaBiO_3$ increases to 30 K by K doing which is originated from strong electron-phonon coupling. This indicates that $BaBiO_3$ has a potential to demonstrate high T_c. Solid-solutions of $Ba(Pb_{1-x}Bi_x)O_3$ also become superconductors [13], but include the disorder problem which might reduce T_c [14]. Therefore, we considered that the removal of disorder by utilizing $BaBiO_3/BaPbO_3$ heterostructures might enhance T_c.

In this section, first, the intriguing points of superconductivity in $BaBiO_3$ are introduced. Second, crystal structures and physical properties of $Ba(Pb_{1-x}Bi_x)O_3$ are reviewed as a function of x (Bi content). At last, the effect of disorder in $Ba(Pb_{1-x}Bi_x)O_3$ is discussed.

1.2.1 Charge Order and Superconductivity in $BaBiO_3$

Charge order and superconductivity are the most remarkable phenomena in $BaBiO_3$ (BBO). BBO is a perovskite-type compound with the three-dimensional network of octahedral BiO_6 in Fig. 1-3 (a). In BBO, the nominal valence of Bi is 4+, indicating 6s orbital has one electron. From a classical band theory, BBO is expected to show metallic behavior due to the half-filled state of 6s orbital. However, in reality Bi^{4+} is skipped, and the stability of the closed cell realizes Bi^{3+} ($6s^2$) and Bi^{5+} ($6s^0$) states (Fig. 1-4) [15]. In addition, Bi^{3+} and Bi^{5+} form an ordered array which means the charge order state as shown in Fig 1-3 (b). Thus, BBO shows semiconducting properties with energy gap of 2 eV [16]. BBO has been often called as "Valence skipper", after skipped Bi^{4+} [17].

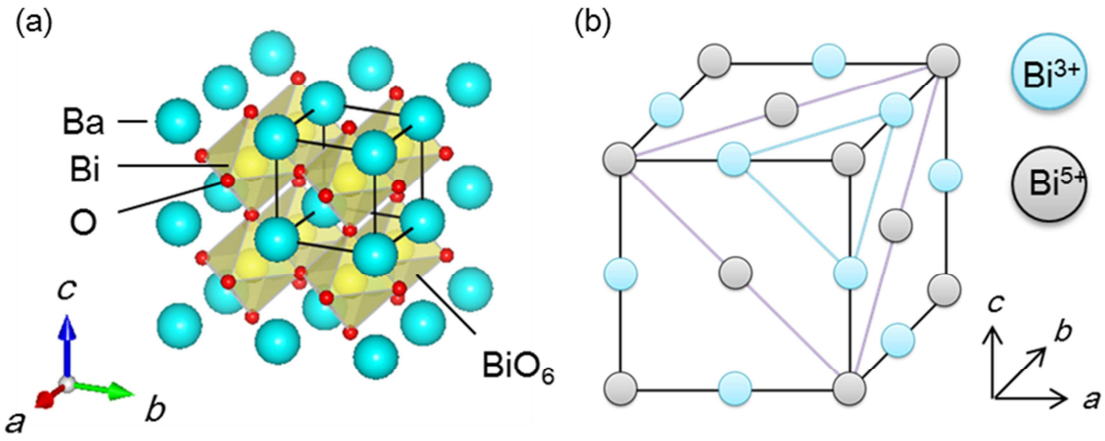

Fig. 1-3. (a) Crystal structure of $BaBiO_3$. Black cubic indicates a unit cell. (a) Displacement of Bi^{3+} and Bi^{5+} in BBO

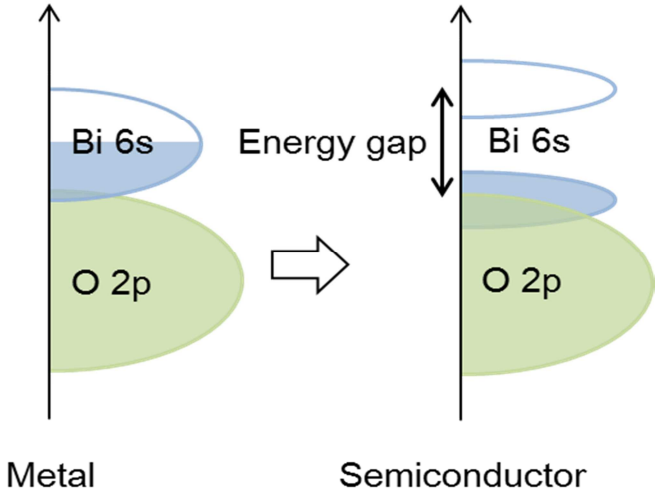

Fig. 1-4. Electronic structure of $BaBiO_3$. Energy gap opens due to the skipping of Bi^{4+} ($6s^1$) state.

The charge order in BBO is suppressed by chemical doping. As a result, a metallic phase of Bi^{4+} ($6s^1$), including superconductivity at low temperatures, appears [11, 13]. This presence of $6s^1$ state has been considered to be a key to demonstrate superconductivity in BBO system. As shown in Fig. 1-5 (a), the highest superconducting transition temperatures is known to be 30 K in $(Ba_{0.6}K_{0.4})BiO_3$. Other example of superconductors related to BBO are the solid solutions $Ba(Pb_{1-x}Bi_x)O_3$ (BPBO) at x = 0.1 ~ 0.35. In BPBO system, the highest transition temperature T_c is known to be 12 K at x = 0.25 (Fig (b) and (c)).

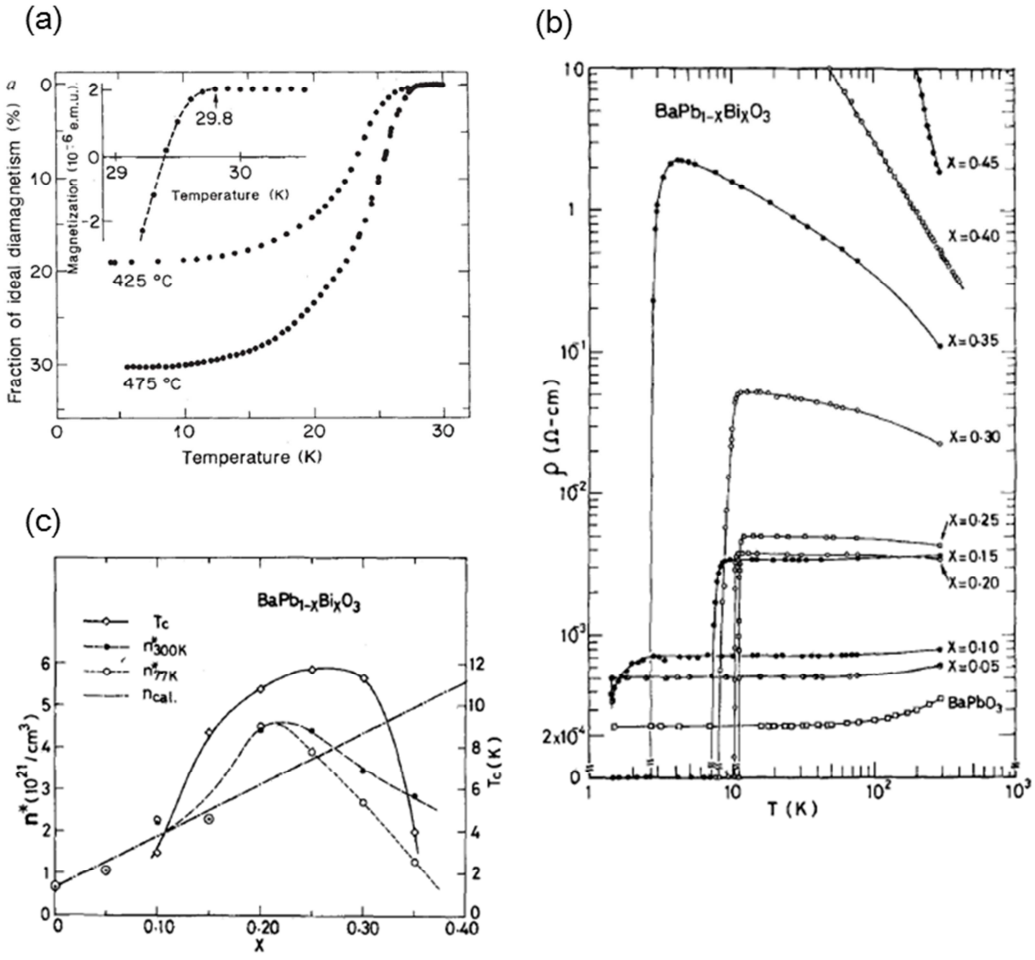

Fig. 1-5. Superconducting properties of BBO. (a) Temperature dependence of superconducting volume fraction in $(Ba_{1-x}K_x)BiO_3$ [11]. (b) Temperature dependence of resistivity in $Ba(Pb_{1-x}Bi_x)O_3$ [18]. (c) Bi composition dependence of carrier density and T_c [18].

In addtion, the charge order state in BBO is considered to be assosiated with breathing distortion of BiO_6 octahedra. BBO also has tilting distortions of BiO_6 octahedra, and the crystal structure of BBO takes a monoclinic symmetry at room temperature. Blow 750-800 K, both of tilting and breathing distortions is reported to exist, while only breathing distortion remains above 750-800 K. mainly [15]. This indicates that the charge order state is thought to exit in BBO at any tempetarue.

The control of crystal distortions might lead to surpress the charge order, resulting superconductivity in BBO. As a way to modulate crystal distortions, there were attempts using an epitaxial strain from substrate of thin films. $(Nd_{0.5}Sr_{0.5})MnO_3$ grown on $SrTiO_3$ is an example in which the physical properties are controlled by an epitaxial strain [19-21].

In an epitaxial thin film of BBO fabricated on MgO substrate [22], the crystal structure holds a cubic symmetry, which is different from monoclinic of BBO in bulk materials. From the X-ray diffraction (XRD) measurement, in BBO films, tilting distortion is found to be suppressed, while, breathing distortion is found to remain. If BBO include tilting distortion, the Bragg peak around 76 degree should be spitted like in Fig 1-6 (a). However, in the thin film of BBO, the splitting of peaks is not observed as shown in Fig 1-6 (b). On the other hand, when there is breathing distortion, the $Bi^{3+}O_6$ and $Bi^{5+}O_6$ octahedra array alternatively, inducing the formation of the superstructure along 111direction. XRD pattern of BBO film shows 333 reflection, which is the superlattice peaks in Fig 1-6 (c). As a result, thin film of BBO shows insulating properties like bulk, implying the epitaxial strain cannot suppress the charge order state of BBO.

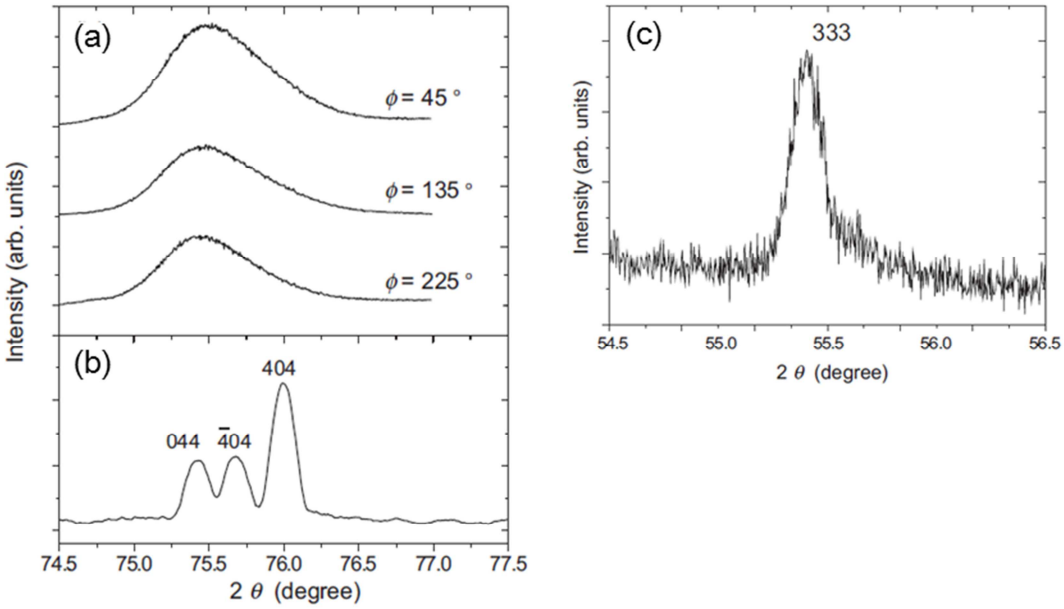

Fig. 1-6. XRD pattern of BBO films fabricated on MgO(001) substrate [22]. (a)-(b) The evidence for the absence of tilting distortion. (a) shows XRD pattern of BBO film, while (b) indicates XRD pattern of bulk BBO. (c) The evidence for the existence of breathing distortion.

1.2.2 Crystal Structure of $Ba(Pb_{1-x}Bi_x)O_3$ System

Evaluation of crystal structure as a function of x is very complicated. $Ba(Pb_{1-x}Bi_x)O_3$ undergoes a clearly unestablished structural phase transitions between tetragonal, orthorhombic, and monoclinic phase at room temperature as a function of the bismuth content. First, Cox and Sleight reported that $Ba(Pb_{1-x}Bi_x)O_3$ exhibit orthorhombic phase for $0 < x < 0.05$, tetragonal phase for $0.05 < x < 0.35$, orthorhombic phase for $0.35 < x < 0.9$, and monoclinic phase for $1 < x < 0.05$ [23]. Some years later, they investigated again to observe a mixture of tetragonal and orthorhombic phase around $x = 0.25$ [24]. This dimorphism was also found by Marx *et al* [25]. Other researchers have conducted the analysis of crystal structure in BPBO as summarized in Fig 1-7, but the general consensus is not obtained.

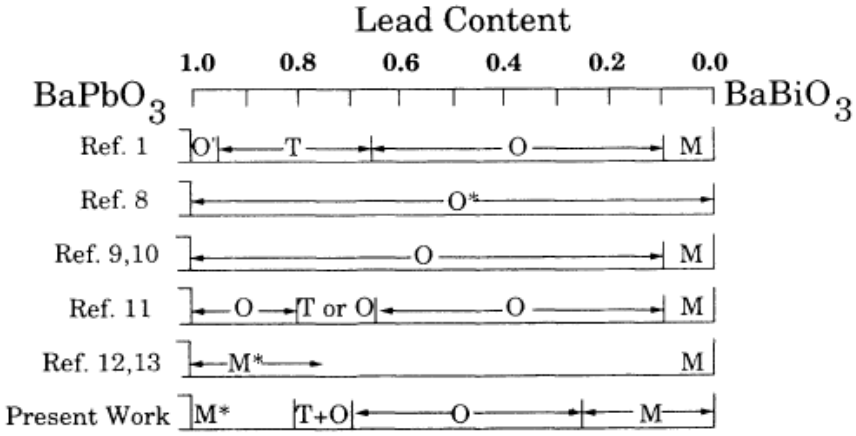

Fig. 1-7. Crystal symmetry of BPBO at room temperature which previous studies suggested [23, 25-30]. T, O, and M indicate tetragonal, orthorhombic, and monoclinic, respectively.

In recent years, the detailed characterizations by X-ray and neutron diffraction also reveal the coexistence of tetragonal and orthorhombic structure in the range of chemical composition showing superconductivity in Fig. 1-8 (a) [31]. This research also suggested that tetragonal phase shows superconductivity, while orthorhombic phase is not superconductor (Fig. 1-8 (b)) [31]. The formation of the nanostructure of tetragonal phase is reported by the analysis of a transparent electron microscopy (TEM) [32].

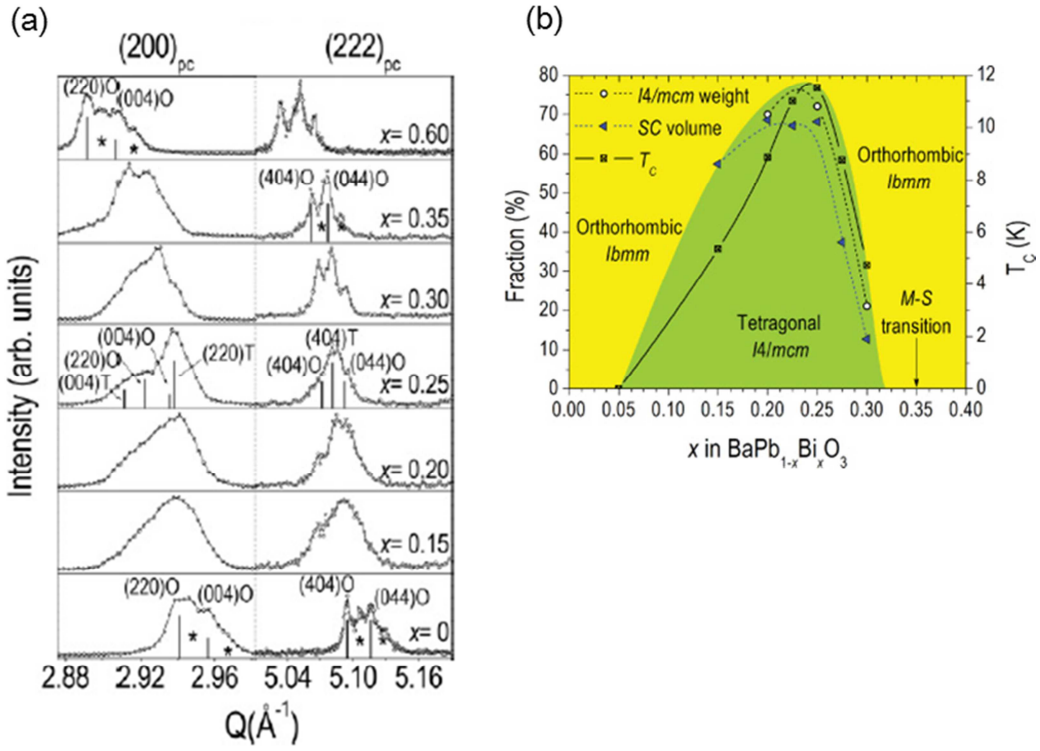

Fig. 1-8. (a) Analysis of XRD patterns in $Ba(Pb_{1-x}Bi_x)O_3$ indicating that tetragonal phase and orthogonal phase coexist [31]. (b) The relationship between superconducting volume fraction and the ratio of exited tetragonal phase [31].

1.2.3 Physical Properties of $Ba(Pb_{1-x}Bi_x)O_3$ System

$Ba(Pb_{1-x}Bi_x)O_3$ solid solutions show interesting properties as a function of x (Bi contents) [33]. They are classified by three regions which are reviewed as below.

A: $0 \leq x \leq 0.20$

In this region, the physical properties are understood by the rigid band model [34]. The hybridization between Pb 6s valence band and O 2p conduction band give rise to a finite density of state near Fermi energy $N(0)$. That leads to a semi-metallic nature in $BaPbO_3$ (BPO). By the

replacement of Pb site for Bi atoms, one 6s electron per atom is doped in the conduction band. The shape of Fermi surface is almost spherical, and the effective mass is lighter than that of free electrons. Optical reflectivity is reasonably fitted by a Drude model, and the reflectivity edges move to the higher frequency region with increasing x [35]. This behavior of reflectivity edges indicates the enhancement of carrier density as a function of x which is understood by the rigid band model. In addition, the experimental data of Hall effect [18] and thermopower [36] are consistent with this rigid band picture. The superconducting transition temperature T_c enhances to around 10 K systematically with increasing x. By the estimation from the McMillan equation, this x dependence of T_c is originated from the enhancement of $N(0)$ and the electron-phonon interaction [37].

B: $0.20 \leq x \leq 0.35$

In this region, BPBO shows superconductivity whose T_c is beyond 10 K, but T_c does not enhance so much with increasing x. T_c take a maximum value of 12 K at x = 0.25, and reduces with increasing to x = 0.35 where the metal-semiconductor transition occurs. In spite of the low $N(0)$, T_c is surprisingly high, suggesting that the electron-phonon coupling is considered to be outstandingly strong. Moreover, transport properties of the normal state exhibit anomalous behavior. For example, the resistivity (ρ) shows a negative temperature (T) dependence, namely, $d\rho/dT < 0$ [18], and the temperature dependence of thermopower is not linear [36]. The optical measurements are also not explained within the framework of normal metallic state. This implies the appearance of a pseudogap in the density of states near Fermi energy $N(0)$ [38]. This pseudogap become larger with increasing x, and a full gap opens at x = 0.35. This depression of the $N(0)$ from x = 0.20 is also supported by the experiments of Hall effect and specific heat [39].

The emergence of a pseudogap is considered to drive the transition into the semiconducting phase. The instability of local CDW is the most reliable origin of the pseudogap, which has been proposed theoretically. This kind of CDW instability is originated from the strong electron-phonon coupling in BPBO [40-42]. Generally, in the system with the strong electron-phonon interaction, the realization of a CDW state often makes the metallic state

unstable. Therefore, a local CDW instability, inductive of a charge disproportionation of Bi^{3+} and Bi^{5+}, is realized even in the metallic BPBO phase, giving a strong influence on the physical properties of BPBO.

C: $0.35 \leq x \leq 1$

In this wide range of Bi content, semiconducting properties are observed. In order to explain the origin of the semiconducting energy gap, some theories has suggested a three-dimensional CDW model [35, 40-42]. In this model, conduction electrons and a breathing-mode phonon are strongly coupled, stabilizing the formation of CDW. However, this model is not consistent with some experimental facts [13, 45-47].

Evidences for the formation of CDW are provided by the optical measurements [38, 46, 47]. In the spectrum of infrared spectroscopy for BBO (x = 1), a characteristic phonon mode is observed. This mode is considered to be associated with a superlattice structure, indicating a three-dimensional ordered arrangement of two kinds of Bi sites. It is confirmed over the whole semiconducting region, supporting the scenario of local CDW. In the measurements of Raman scattering, BBO shows an extremely intensive line which is explained by the breathing phonon. This line in Raman spectrum also suggests the existence of interband excitation across the semiconducting energy gap.

Moreover, the measurements of transport and magnetic properties also support the formation of CDW [33, 48]. These properties are observed in only the semiconducting phase, indicating the demonstration of bipolaronic conduction and the existence of CDW domain walls [48].

1.2.4 Disorder Effect in $Ba(Pb_{1-x}Bi_x)O_3$ superconductors

Disorder is considered to be an essential factor in understanding the physical properties of BPBO. The difference of T_c between BPBO and BKBO is often explained to be originated from disorder by chemical doing. In BKBO, chemical substitutions take place on Ba atoms of BBO, indicating that the effect of conduction electron in Bi is considered to be small. However, in BPBO, Bi atoms which contain conduction electrons are replaced by Pb atoms, leading large disorder effect. Thus, T_c of BPBO is considered to be lower than that of BKBO.

The transport properties of BPBO system as a function of x also indicate the effect of disorder. Resistivity of BBO (x = 1) is the highest value in BPBO system. As decreasing the content of Bi, resistivity become smaller systematically, and BPO (x = 0) show the lowest resistivity in this system, as shown in Fig. 1-5 (b) [18]. Carrier density and superconducting transition temperature form similar dome-shaped phase diagram as a function of x, as Fig. 1-5 (c) indicates. The behavior of carrier density is not related to the x dependence of resistivity, suggesting the effect of disorder by chemical substitutions is a dominant factor to determine the transport properties.

Reduction of Superconducting T_c by Disorder

Electrons move diffusively in the presence of disorder such as the scattering by impurities, indicating that the effective Coulomb repulsion increases. This enhancement of the effective Coulomb interaction weakens the electron-phonon interaction which drives to form cooper pairs in superconductors [49, 50]. That is, disorder has been known to decreases T_c. This disorder dependence of T_c is also demonstrated experimentally [51, 52].

Disorder is known to cause localization. In terms of localization, disorder reduces the density of state (DOS) near Fermi energy. D. Beliz describes DOS like

$$N(\tilde{\omega}) = \frac{N_F}{(Y' + 1)}, \qquad \text{(Eq.1-5)}$$

by introducing Y' as a parameter of disorder [53-55]. Here, $N(\tilde{\omega})$ is the DOS estimated at a characteristic phonon frequency, and N_F is the DOS at Fermi level of the normal metal without disorder. He applies this relationship between the DOS and disorder into the McMillan equation about T_c in strong coupling superconductors, resulting the blow equation,

$$T_c = \frac{\Theta_D}{1.45} \exp\left[\frac{-1.04(1+\tilde{\lambda}+Y')}{\tilde{\lambda}-\tilde{\mu}^*[1+0.62\,\tilde{\lambda}/(1+Y')]}\right] \qquad \text{(Eq.1-6)}$$

where Θ_D is Debye temperature, and μ is the disorder dependent electron-phonon interaction, and λ is the disorder dependent Coulomb pseudopotential. This equation explains the experimental data of T_c well in Pb thin films as shown in Fig. 1-9.

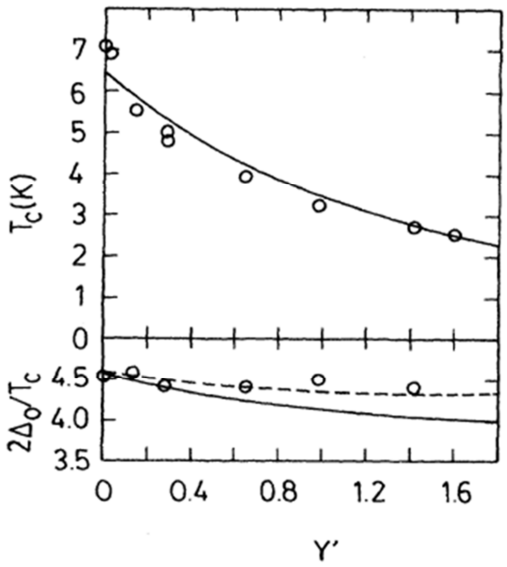

Fig. 1-9. Solid curve are theoretical predictions for the transition temperature and the ratio $2\Delta_0/k_BT_c$ [55]. The dashed curve indicates the theoretical result for $2\Delta_0/k_BT_c$ with am Einstein spectrum. Circles show experimental data of Pb.

Possibility to Enhance Superconducting T_c

The point-contact spectroscopy tunneling measurements are done on BPBO, and the reduction of density of states (DOS) is observed. This suppression of DOS yields the estimation of a disorder parameter *Y*' which is introduced in 1.3.1. Figure 1-8 show that the enhancement of T_c in BPBO is suggested if the disorder can be removed perfectly, namely, $Y' = 0$ [14].

In addition, it is reported that disorder is related to a metal-insulator transition (MIT) in BPBO. This kind of disorder induced MIT is observed in Si-doped Nb and explained by McMillan's scaling theory [56]. The behavior in transport properties and tunneling DOS in BPBO agree with the predictions which are originated from this scaling theory. This transition occurs at $x \sim 0.30$ which is different from $x \sim 0.35$ of realizing charge order state. Thus, MIT at $x \sim 0.30$ is considered to have different origin of charge order, namely disorder [14]. The evidence of disorder induced MIT implies that disorder is an important factor to determine physical properties of BPBO.

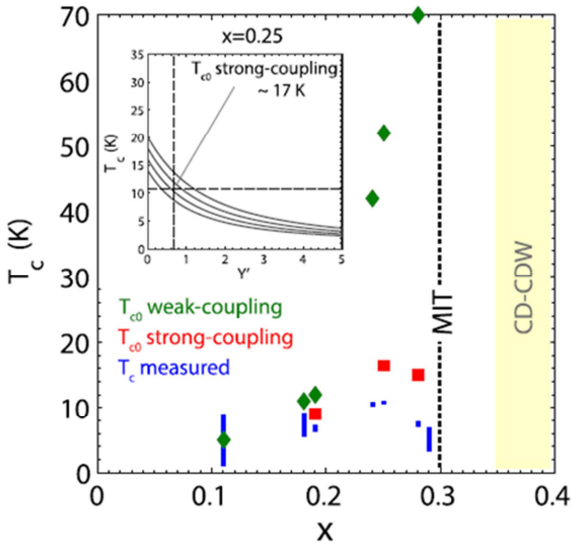

Fig. 1-10. Effect of disorder in superconducting properties of $Ba(Pb_{1-x}Bi_x)O_3$ [14]. Inset indicates *Y*' dependence of calculated T_c.

1.3 Superconductivity at Interface

In order to enhance T_c, high DOS near Fermi level and strong attractive interaction are needed within the framework of BCS theory. Large carrier density means high DOS near Fermi level, and carrier doping is a way to realize high T_c, However, the chemical doping accompanies the introduction of disorder such as impurities and lattice distortion, which is responsible for the drop of T_c.as shown in the section of 1.2. Thus, carrier doping without introducing disorder is more powerful to demonstrate high T_c. In this section, the methods of modulating carrier density without introducing disorder and their applications to control physical properties are reviewed.

1.3.1 Charge Transfer across Oxide Interfaces

The recent development in technique to synthesize materials at atomic-scale enables to design oxide heterostructure with the high crystallinity. This kind of progress accelerates the researches about the surface and the interface state of materials. In particular, the oxide interfaces are focused as a stage to emerge novel physical phenomenon [57-59]. The demonstration of physical phenomenon at oxide interface is a basic concept of this study, and it is originated from the charge transfer at the interface which is carrier-doping without disorder-introducing. So far, superconductivity [60, 61], ferromagnetism [62, 63], and the quantum Hall effect [64, 65] have been reported to emerge at oxide interfaces. In this section, we focus on superconducting transitions among outstanding achievements in oxide interfaces, and reviewed them.

Superconductivity at $LaAlO_3/SrTiO_3$ interface

$LaAlO_3/SrTiO_3$ heterostructures are the most famous systems to demonstrate the interface state. While both of $LaAlO_3$ (LAO) and $SrTiO_3$ (STO) are insulators with a wide energy gap, the interface between LAO and STO become metallic implying the realization of two-dimensional electron gas (2DEG) as shown in Fig. 1-11 [66]. The origin of this 2DEG has

been a subject of discussion since the metallic state at LAO/STO interface was achieved. Despite much effort to reveal the origin of this metallic state, the general consensus has not been reached yet. Some scenarios about the mechanism of charge accumulation at LAO/STO interface are suggested such as the polar catastrophe, the oxygen deficiency, and the cation interdiffusion.

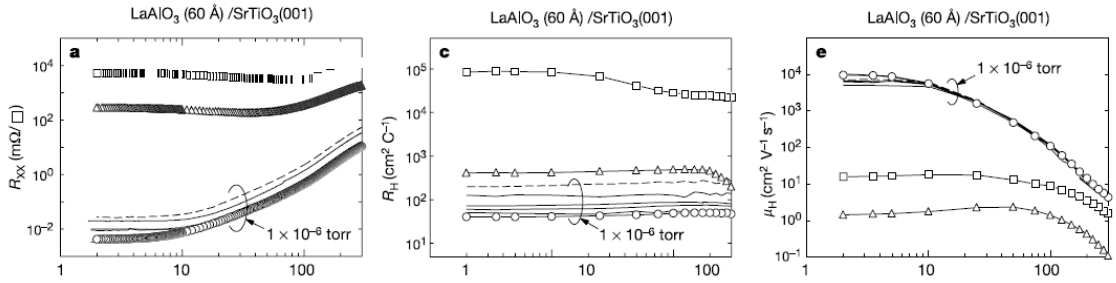

Fig. 1-11. Temperature dependence of transport properties (electrical resistance, Hall coefficient, mobility) at $LaAlO_3/SrTiO_3$ interface [66].

Figure 1-12 (a) indicates that 2DEG at LAO/STO interface undergoes a superconducting transition at $T_c \sim 180$ mK [60], although the phase transition is constrained due to the presence of strong fluctuations. The angular dependence of upper critical field H_{c2} shows anisotropic behavior, indicating superconductivity is confined in a narrow area. When the magnetic field is parallel to the two-dimensional plane, H_{c2} take a maximum value, and H_{c2} reduces systematically with decreasing the angle between magnetic field and the two-dimensional plane, as shown in Fig. 1-12 (b). Detailed analysis of this anisotropy in H_{c2} reveals that superconductivity at LAO/STO is two-dimensional with the thickness of 10 nm [67]. The current-voltage characteristics and the temperature dependence of electrical resistance suggest that this transition into a superconducting state can be understood as a Belezinskii-Kosteliz-Thouless transition, supporting two-dimensional superconductivity [60].

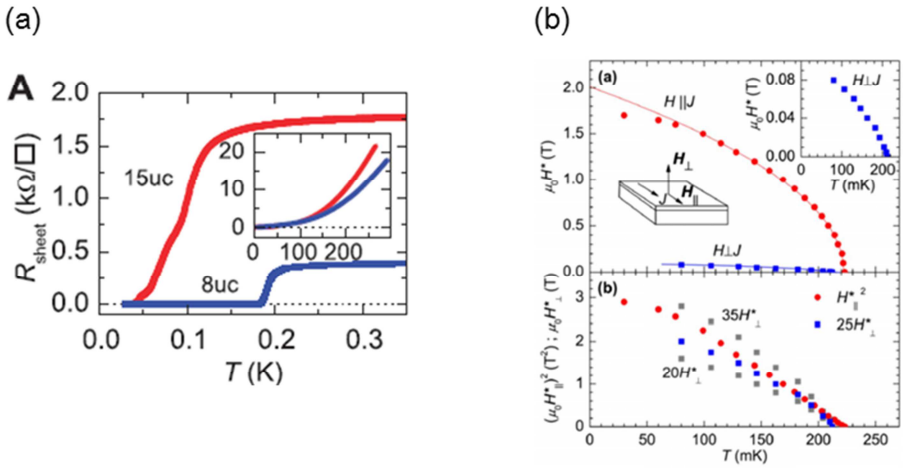

Fig. 1-12. Superconducting properties at LAO/STO interface. (a) Temperature dependence of electrical resistance [60]. (b) The anisotropy of the upper critical field [67].

Superconducting properties at LAO/STO interface was modulated by utilizing a gate voltage (V_G) in a field effect transistor (FET) structure like Fig. 1-13 (a) [68]. $SrTiO_3$ substrate has a large dielectric constant, indicating V_G across the substrate enables to control the carrier density at LAO/STO interface. The V_G dependence of T_c showed the dome-shaped superconducting phase diagram in Fig. 1-13 (b), and a quantum phase transition from a superconducting ground state to an insulating is discussed at LAO/STO interface.

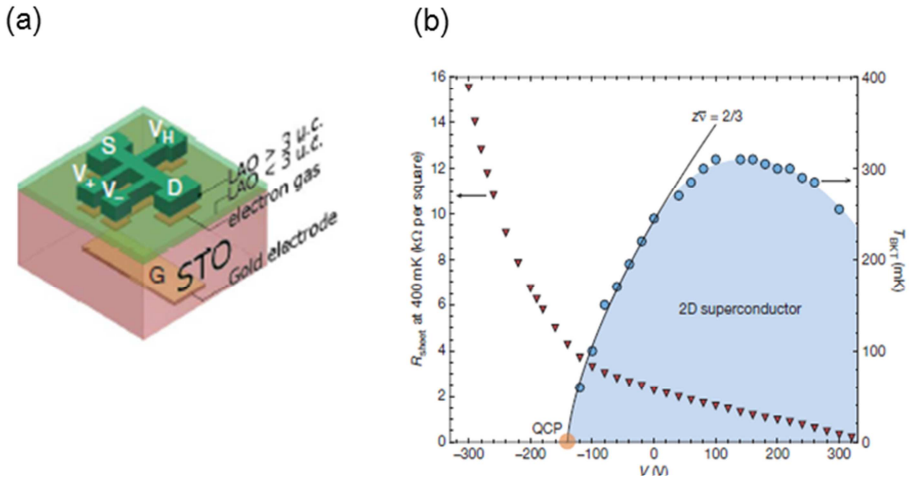

Fig. 1-13. (a) Device structure of a field effect transistor fabricated for LAO/STO interface [68]. (b) V_G dependence of T_c at LAO/STO interface [68].

Cuprate interface

Interface states of layered cuprates which shows high-temperature superconductivity are created. Thin films of heterostructure with single interface between an over-doped metal $(La_{1.55}Sr_{0.45})CuO_4$ and a Mott-insulator La_2CuO_4 was formed to show superconductivity. More interestingly, at the interface between an over-doped metal $(La_{1.55}Sr_{0.45})CuO_4$ and a superconductor $La_2CuO_{4-\delta}$, transition temperature T_c is increased to 50 K, which exceeds the maximum T_c of bulk $(La,Sr)_2CuO_4$ system, as shown in Fig. 1-14 (a) [61]. Atomically sharpe interface was demonstrated from the analysis of scanning transparent eletron microscope (STEM) and electron energy-loss spectroscopy (EELS) in Fig. 1-14 (b), denying that inter-site mixing induce superconductivity [61]. The interface superconductivity was suggested to present even in a single CuO_2 layer [69].

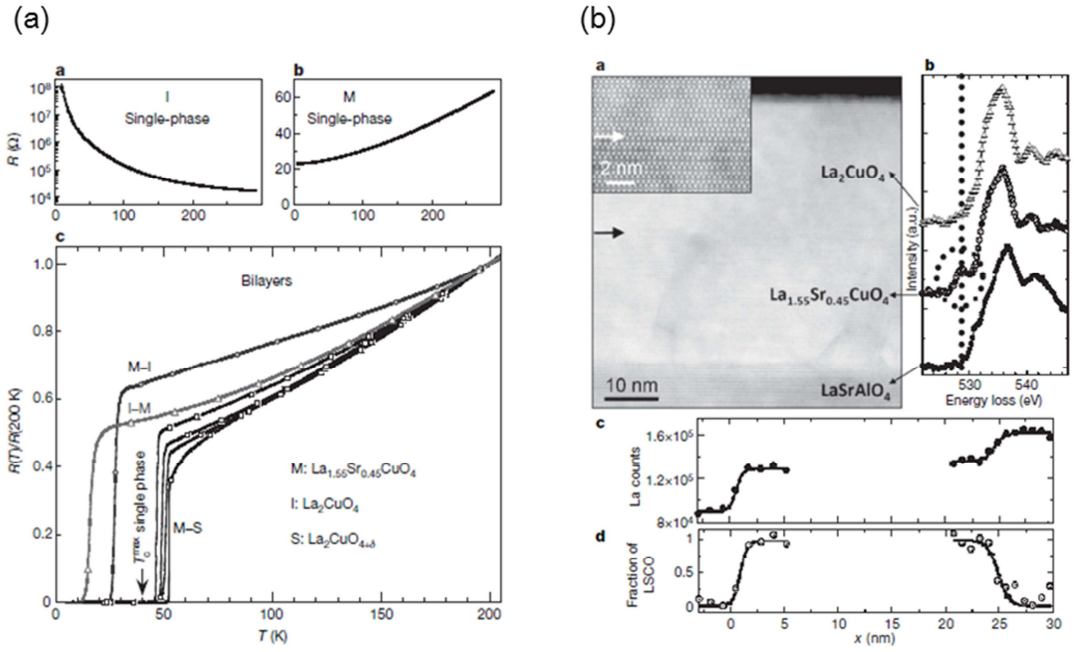

Fig. 1-14. (a) Temperature dependence of resistivity in cuprate heterostructures with single interface [61]. (b) STEM image and EELS spectrum of a cuprate heterostructure with single interface [61].

1.3.2 Electrostatic Doping by Field Effect Transistor

In the conventional metal-oxide-semiconductor felid-effect transistor (MOSFET) structure, the physical properties can be modulated by changing the gate voltage. The control of T_c at LAO/STO interface is one of examples for the FET application, as introduced in the section of 1.2.1. This electrostatic carrier doping demonstrates a high tenability of carrier density, and realizes the absence of disorder which is different from chemical doping [70]. By using the FET configuration, the electric-field-control of superconductivity was performed in cupate thin films [71]. However, superconductivity is not induced by the electrostatic carrier doping in FETs, because the accumulated carrier density at the interface is not enough to demonstrate a superconducting transition.

In recent year, electric double layer transistor (EDLT) which is different from MOSFET structure attracts attentions. In EDLT configuration like Fig. 1-15 (a), ionic conductors such as ion liquid are utilized as gate insulator instead of solid gate dielectrics in MOSFET. At the interface between semiconductor and ionic conductor, an electric double layer is formed with the thickness of a few nanometers. This double layer is considered to be a capacitor composed of a sheet of ions in the electrolyte and another sheet of accumulated image charges on the surface of solid. In these structures, large charge accumulation is realized as a two-dimensional carrier density around 10^{15} cm^{-2} [72]. This value is 1-2 orders of magnitude larger than that induced in MOSFETs. In EDLT structure, the application of gate voltage realized metal-insulator transition with superconductivity at low temperatures, which was observed in $SrTiO_3$ [73] in ZrNCl [74] Furthermore, a superconducting transition was demonstrated in $KTaO_3$ [75] which has never reported to show superconductivity by chemical doping. In cuprate superconductors, the control of T_c is demonstrated [76], and in MoS_2, T_c exceeds bulk values by utilizing EDLT doping [77]. Not only superconductivity but ferromagnetism and metal-insulator transition are performed in Co-doped TiO_2 films [78] and VO_2 film [79], respectively.

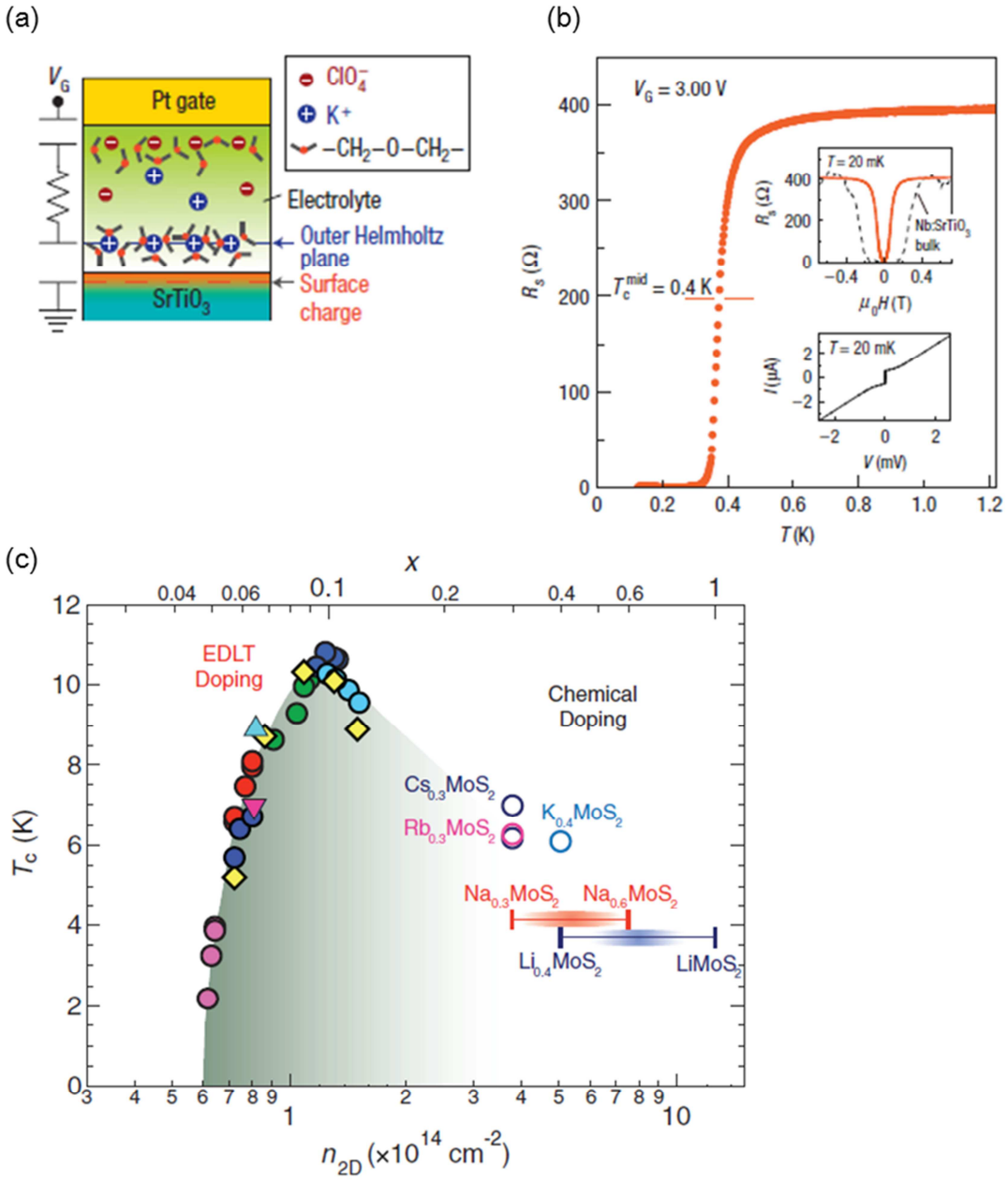

Fig. 1-15. (a) Schematic picture of an EDLT configuration [73]. (b) Electric field induced superconductivity in $SrTiO_3$ [73]. (c) Electric field tuned T_c of MoS_2 [77].

Chapter 2

Purpose

In this chapter, the motivation and the objective of this study are described.

2.1 Enhancement of Superconducting Properties in Oxide Heterostructures

Superconductivity has various potentials in condensed matter physics and practical applications. Superconducting T_c has been increasing due to much effort of scientists. The technique to control the synthesis of materials at an atomic-scale has been developed rapidly. This provides us with the opportunities to investigate the interface state between materials without introducing disorder. Oxide interfaces have demonstrated novel phenomenon such as superconductivity, magnetism, and the quantum Hall effect, as noted in chapter 1.

In this research, we aim at applying the technique of film growth to the superconducting materials. Possible enhancement of a superconducting transition temperature is anticipated. The creation of interface enables to remove disorder of atomic displacement in solid solutions. The removal of disorder provides a chance to increase a transition temperature, but generally, in two-dimensional system like single interface, a phase transition temperature might be suppressed due to the large fluctuation. Therefore, if three-dimensionality is recovered by fabricating superlattice structure, the materials which are introduced interface artificially can realize the higher superconducting transition temperature.

For the enhancement of a superconducting transition temperature, we consider below two steps: First is the realization of the charge transfer and two-dimensional superconductivity at oxide interface without disorder. Second is the enhancement of a superconducting transition temperature by utilizing superlattice structure.

2.2 Possibilities of $BaBiO_3$/$BaPbO_3$ Heterostructures

In order to achieve the purposes described in 2.1, we focus on $BaBiO_3$ (BBO)-$BaPbO_3$ (BPO) systems. The solid solution $Ba(Pb_{1-x}Bi_x)O_3$ (BPBO) of BBO and BPO is known to show superconductivity, as introduced in chapter 1. The superconducting transition temperature T_c is reported to be 12 K at maximum. $(Ba_{1-x}K_x)BiO_3$ (BKBO) where Ba takes place to K in BBO also realizes superconductivity and T_c increases to 30 K. The difference of T_c between BPBO and BKBO is considered to be originated from the chemical substituted site in BBO. In BPBO, disorder is introduced to Bi site which dominates the electrical conduction, while in BKBO disorder by chemical substitution does not affect so much to conduction site. This indicates that BPBO has a potential to increase T_c up to ~ 30 K which is T_c of BKBO, if disorder is removed from the conduction site of Bi. Therefore, in BBO-BPO system, we tried to clarify the relationship between superconductivity and disorder, and enhance the superconducting properties by introducing heterostructures where disorder is eliminated from Bi sites.

2.2.1 Charge Transfer and Two-dimensional Superconductivity at $BaBiO_3$/$BaPbO_3$ Interface

This is a first topic of this study which is discussed mainly from chapter 5 to chapter 7. We aim at demonstrating two-dimensional superconductivity at BBO/BPO interface. The heterojunction of BBO and BPO is expected to occur superconductivity as a result of the charge transfer, implying that 6s electrons move from Bi site to Pb site near BBO/BPO interface. For that, we fabricated thin films with atomically flat BBO/BPO interface in chapter 5. Superconductivity and its dimensionality were confirmed by some measurements of transport properties in chapter 6. Moreover, the characterizations of superconducting BBO/BPO interface were performed and the possibility of cation interdiffusion was argued by comparison with transport properties of solid-solution BPBO in chapter 7.

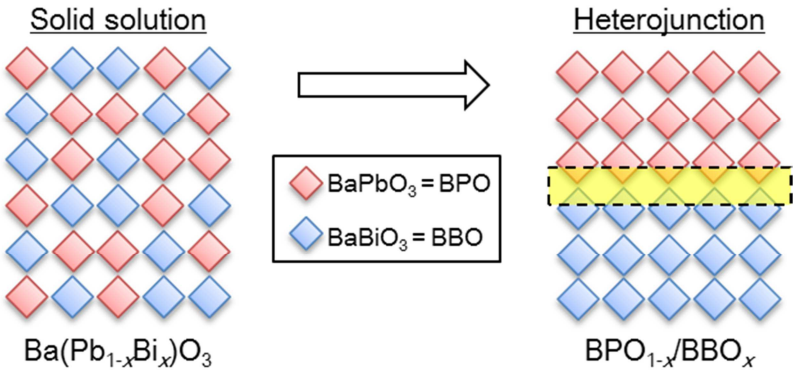

Fig. 2-1. Concept of the introduction of the heterojunction into the solid solution system. BPO/BBO interface has a potential to show superconductivity as a result of charge transfer.

2.2.2 Enhancement of Superconducting T_c in $BaBiO_3/BaPbO_3$ Superlattices

This topic is discussed in chapter 8. In a single BBO/BPO interface, T_c might be suppressed by the thermal fluctuation inherent in two-dimensional systems, even if disorder is removed from BPBO systems. In order to overcome this problem, we focused on superlattice structure, indicating the control of distance between interfaces. In the limit of a long superlattice period, BBO/BPO interfaces do not interact with each other, and the superconducting properties will be the same as the thin film with a single BBO/BPO interface. However, when the distance between BBO/BPO interfaces become smaller, the overlap of interface region might recover three-dimensionality and realize the higher carrier density at the area between interfaces, leading to enhance T_c.

We selected $Ba(Pb_{0.75}Bi_{0.25})O_3$ as a chemical composition of superlattices. At this Bi content, it is known that bulk BPBO shows the highest T_c. To keep this composition, BBO_mBPO_{3m} superlattice was fabricated. The transport properties of BBO_mBPO_{3m} were investigated as a function of m, indicating the distance of interfaces.

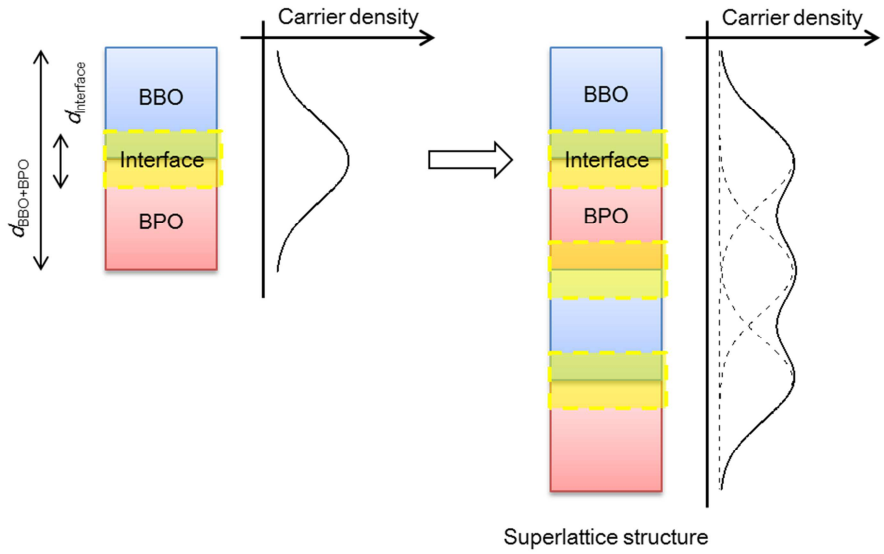

Fig. 2-2. Concept about the formation of superlattice structure at $d_{interface} < d_{BPO+BBO}$. Superconducting properties will be dominated by the BBO/BPO interfaces

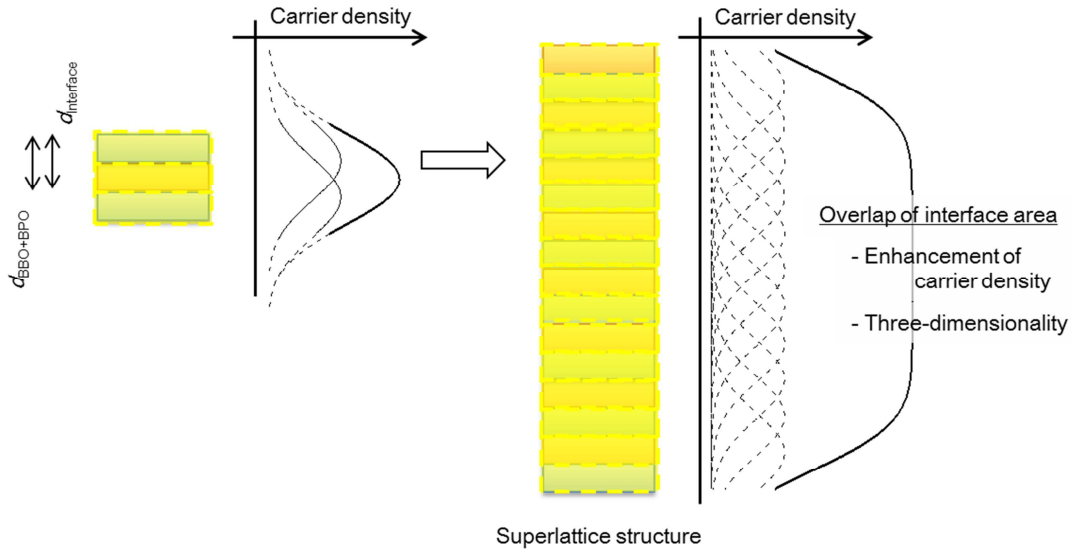

Fig. 2-3. Concept about the formation of superlattice structure at $d_{interface} \sim d_{BPO+BBO}$. T_c is expected to enhance because of the recovery of three-dimensionality and the increase of carrier density.

Chapter 3

Experimental

In this chapter, we summarized equipment and method for experiments of this study.

3.1 Fabrication of Thin Films

Pulsed Laser Deposition Method

The technique of pulsed laser deposition (PLD) has been utilized to fabricate thin films with high quality for a decade or more. In PLD method, a high power pulsed laser is used to evaporate a target material from its surface. This process is called as "ablation" where a plasma plume with atoms composing a target material emerges from the surface of the target. These ablated particles are deposited on an appropriately located substrate, and the thin film grows on the substrate. The process of ablation is usually performed under the ultra-high vacuum or in the presence of gases such as oxygen or nitrogen. The technique of PLD has some advantages as below;

- ✓ It is suitable for fabricating thin films of oxides with a high melting temperature
- ✓ The difference of composition between target materials and thin films is small.
- ✓ Impurities are difficult to be contaminated due to the usage of laser.
- ✓ The growth rate is precisely controllable by changing the number of laser pulses.
- ✓ It is appropriate for the fabrication of heterostructures since the target material are easy to exchange during deposition.

Considering these merits, we synthesized thin films in this study by utilizing a pulsed laser deposition (PLD) technique. Figure 3-1 shows the setup of a PLD system where we used KrF excimer laser (λ = 248 nm) as an ablation laser. MgO (a ~ 4.21 Å) was chosen as the substrate because of the relatively good match with BBO and BPO where the pseudocubic

lattice parameters are ~ 4.36 Å and ~ 4.26 Å, respectively. The repetition rate of the laser was fixed to be 5 Hz, and the growth rate of films was about 10 pulses per one unit cell. The other growth conductions, such as substrate temperature, oxygen pressure were noted in the following chapters. In addition, we consider chemical compositions of target materials due to the high voracity of Ba, Bi, and Bi atoms.

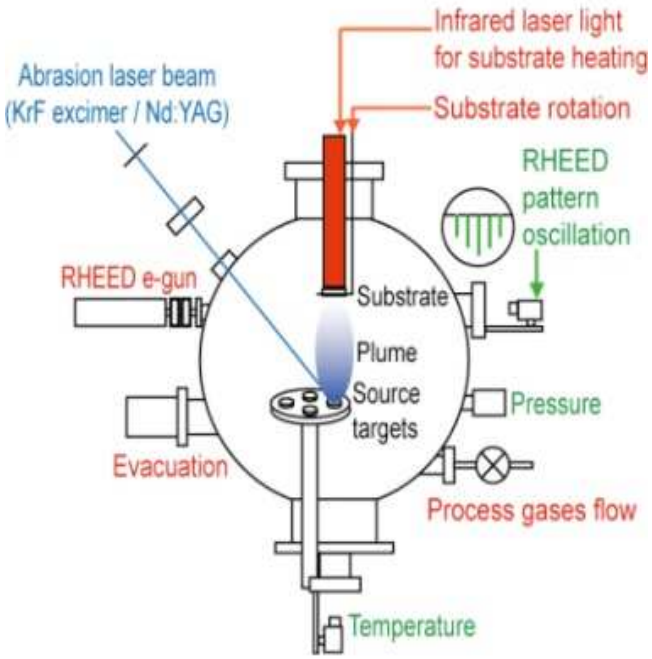

Fig. 3-1. Schematic picture of a PLD system which we used in this study [80].

3.2 Structural and Compositional Analysis of Thin Films

The crystal structures and the thickness of thin films in this study were characterized by X-ray diffraction (XRD) and X-ray reflection (XRR) measurement on a diffractmeter (SmartLab, Rigaku), using Cu Kα radiation. The surface morphology of thin films were evaluated by reflect high energy electron diffraction (RHEED) and atomic force microscopy (AFM; SPA400, SII NanoTechnology). Chemical composition of synthesized films were checked by a scanning electron microscope (SEM, VE-8800, Keyence) equipped with energy dispersive X-ray spectrometry (EDS, INCAPentaFET×3, Oxford Instruments).

In addition, an atomic-resolved EDS mapping of the cross-sectional BBO/BPO interface was performed, using a probe forming aberration corrected scanning transmission electron microscopy STEM (JEM-ARM200F, JEOL), which is equipped with a dual silicon drift detectors (dual-SDD) of EDS. This STEM-EDS observation was done by collaborating with Prof. Ikuhara's group in the University of Tokyo.

All measurements for these kinds of characterization were demonstrated at room temperature. As below, we briefly summarized the features of techniques which were used to characterize thin films fabricated in this study

X-ray Diffraction (XRD)

When X-ray is applied materials, the scattered X-ray indicates the diffraction patterns which reflect atomic position and crystal symmetry. From these diffraction patterns inherent in materials, we can calculate their lattice parameters.

X-ray Reflection (XRR)

X-ray is applied at a very low angle against the surface of thin film. The X-rays are reflected at interfaces such as vacuum/film and film/substrate, and they interfere each other. By changing the angle of incident X-ray, we measure the intensity of reflected X-ray which indicates the oscillation as a function of the angle. This oscillation includes the information about the thickness and the density of thin films which we can estimate.

Reflect High Energy Electron Diffraction (RHEED)

Electron-beam is applied at an extreme low angle against the surface of thin film. Incident electron-beams are diffracted by the atoms on the surface of thin film, and form the diffraction patterns, which give us the information about the surface structure of film. In this study, RHEED measurement was done in a PLD chamber soon after the deposition of thin film *in-situ*.

Atomic Force Microscopy (AFM)

By detecting the force between the tip and the material, we can get the real-space image of the surface of material, and evaluate the surface morphology. Moreover, the surface roughness can be estimated quantitatively from the AFM image.

Energy Dispersive X-ray Spectrometry (EDS)

Characteristic X-rays is emitted by radiating electron beams to materials. The energy of characteristic X-rays is inherent in elements. Thus, we can obtain the chemical composition of materials by analyzing the spectrum of characteristic X-rays. Usually, EDS detectors are equipped with scanning electron microscopes (SEM) and transmission electron microscopes (TEM).

Scanning transmission electron microscope (STEM)

This is a sort of transmission electron microscopes (TEM). As scanning electron-beams focused in the area of sub-nanometer scale, they are applied to materials. Scanning images are obtained by detecting scattered transmission electron-beams. By using a high-angle detector with STEM, we can obtain a high-angle annular dark field (HAADF) image which realizes the contrast depending on atomic numbers.

3.3 Measurement of Transport Properties

Transport properties of thin films were measured on a physical property measurement system (PPMS, Quantum Design). Four-terminal method and Van der Pauw method are used in the measurement of electrical resistance and Hall resistance. Current-voltage measurement was done by a home built apparatus which generates a pulsed electrical current, in order to prevent the thermal effect. Wiring was performed by using gold wires (NIRACO; 25 μm) and silver pastes (Dupont; 4922N). At these measurements, the electric current was flowed to be 5 μA which is enough small for a superconducting critical current ~ 1 mA, which was obtained in chapter 6.

In solid-solution BPBO films, the superconducting transition temperature T_c was determined by the measurement of magnetization on a magnetic property measurement system (MPMS, Quantum design) equipped with a superconducting quantum interference device (SQUID). Applied magnetic field was 10 Oe which is enough small in comparison with the upper critical field. T_c was defined as an onset of the transition of magnetic moment.

Four-terminal method

Four-terminal method enables to measure electrical resistance precisely, by excluding the contribution of contact resistance and wire resistance. When we flow electric current I_{14} from 1 to 4, we measure electrical voltage V_{23} between 2 and 3, and calculate raw electrical resistance R_{raw} as V_{23}/I_{14} (Fig. 3-2). By using R_{raw}, we can estimate the sheet resistance R_s and resistvity ρ as following;

$$R_s = R_{raw}\frac{w}{l}, \quad \rho = d \times R_s \qquad \text{(Eq.3-1)}$$

Where w, l, and d indicate width of film, distance between terminals, and thickness of film. The measurement of current-voltage characteristics was also performed in this configuration.

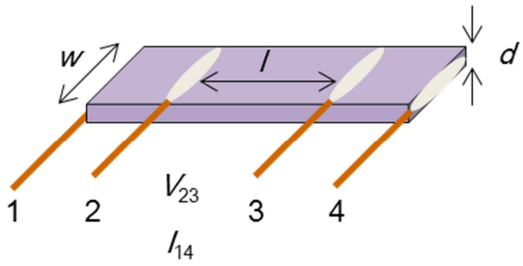

Fig. 3-2. Configuration of four-terminal method.

Van der Pauw method

Van der Pauw method enables to estimate sheet resistance R_s of film. In this method, the shape of sample should be a square, and wire should be attached at the corners as shown Fig. 3-3. When we flow electric current I_{12} from 1 to 2, we measure electrical voltage V_{43} between 4 and 3, and calculate electrical resistance $R_{12,43}$ as V_{43}/I_{12} (Fig. 3-3). In a similar way, we calculate electrical resistance $R_{14,23}$ as V_{14}/I_{23}. R_s is obtained as a solution of below equation, by using $R_{12,43}$ and $R_{14,23}$.

$$e^{-\pi R_{12,43}/R_S} + e^{-\pi R_{14,23}/R_S} = 1 \qquad \text{(Eq.3-2)}$$

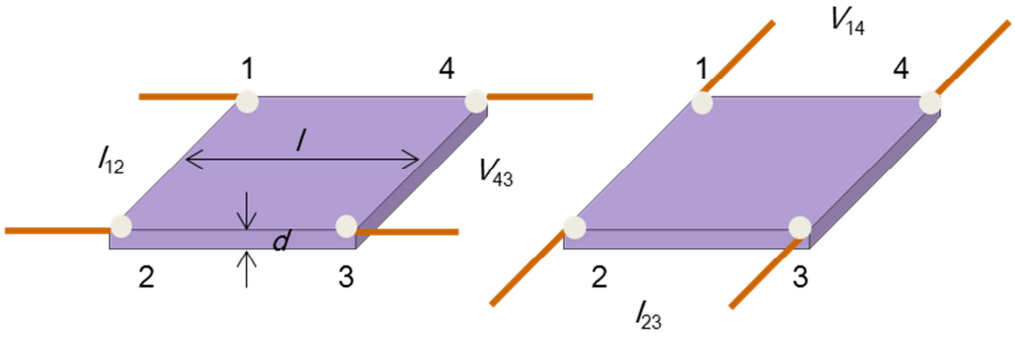

Fig. 3-3. Configuration of Van der Pauw method.

Hall measurement

When magnetic field B is applied perpendicular to the plane and electrical current flow I_x from 2 to 4, electrical field E_y emerge by Lorenz force, as shown in Fig 3-4 (a). E_y is given by,

$$eE_y = eBv_x \quad \text{(Eq.3-3)}$$

R_H is defined as Hall coefficient like,

$$R_H = \frac{E_y}{j_x B} = \frac{E_y}{(env_x)B} = \frac{1}{en} \quad \text{(Eq.3-4)}$$

where e and n indicate elementary charge and carrier density. In addition, R_H is described by,

$$R_H = \frac{E_y}{j_x B} = \frac{V_y}{I_x B} z = \frac{R_{xy}}{B} z \quad \text{(Eq.3-5)}$$

$$\frac{R_{xy}}{B} z = \frac{1}{ezn} \quad \text{(Eq.3-6)}$$

where z is the thickness of sample and R_{xy} is defined by V_y/I_x. Thus, we can evaluate carrier density n, by estimating R_H or R_{xy}.

In experiment, we use the configuration of Van der Pauw method as shown in Fig 3-4 (b). By flowing the electrical current $I_x = I_{24}$, we measure $V_y = V_{31}$, and plot the slopes of line about B dependence of R_{xy} as a function of temperature.

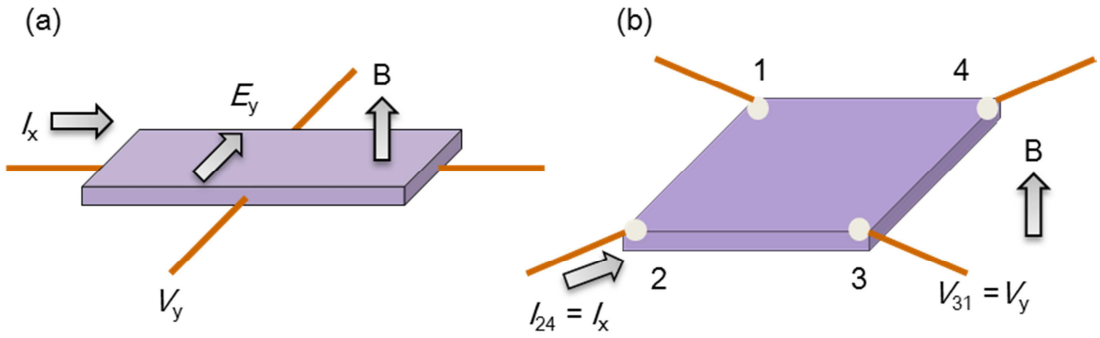

Fig. 3-4. (a) Principle of Hall effect. (b) Configuration of Hall measurement.

Chapter 4

Optimal Growth Conditions and Physical Properties of $Ba(Pb_{1-x}Bi_x)O_3$ Films

Epitaxial thin films of BBO and BPO are useful for the fabrication of BBO/BPO heterostructures. In order to realize the epitaxial growth, the growth condition such as oxygen pressure, substrate temperature should be optimized. Stoichiometry of fabricated thin films should also be considered because of the high voracity of Ba, Pb, and Bi atoms. In this chapter, we aim at clarifying the best condition for the epitaxial growth of solid-solution BPBO [= $Ba(Pb_{0.75}Bi_{0.25})O_3$], BPO, and BBO, and investigating their physical properties. Furthermore, we preformed the characterization of BPO_{25}/MgO and BBO_{75}/MgO. They are constituents of BBO/BPO heterostructures with single interface, which were used from chapter 5 to chapter 7.

4.1 $Ba(Pb_{0.75}Bi_{0.25})O_3$ Films

First, the growth conditions of oxygen pressure and substrate temperature were optimized in the fabrication of solid-solution $Ba(Pb_{0.75}Bi_{0.25})O_3$ films. Superconducting properties of films were also investigated.

4.1.1 Fabrication by Using a Stoichiometric Target Material

The material with the nominal composition of $Ba(Pb_{0.75}Bi_{0.25})O_3$ was prepared as a target compound for a laser ablation of PLD. $BaCO_3$, PbO_2, and Bi_2O_3 powders were mixed to be Ba:Pb:Bi = 1:0.75:0.25, and sintered at 800 °C for 2 days. The obtained materials were pelletized for the PLD target and were heated again at 800 °C by using a spark plasma sintering (SPS) method.

Figure 4-1(a) shows 2θ-θ scan of XRD pattern in BPBO films, which were fabricated at the oxygen pressure of 30 mTorr and 190 mTorr, keeping the substrate temperature at 600 °C. The total thickness of both films was estimated to be about 250 nm by XRR measurement. In XRD pattern, all peaks except for MgO contribution are considered to be originated from the reflection of perovskite-type structure with out-of-plane lattice parameters about 4.28 Å ~ 4.30 Å. These value are comparable to those of bulk $Ba(Pb_{0.75}Bi_{0.25})O_3$. However, the epitaxial growth along [001] direction was not realized. The number of peaks depended on oxygen pressure. The BPBO film deposited at 190 mTorr had the peaks from 00*l* and 0*ll* reflection, while the BPBO film with oxygen pressure of 30 mTorr included various kinds of Bragg peaks This oxygen pressure dependence indicates that higher oxygen pressure is needed to realize BPBO films with high orientation.

Full width at half maximum (FWHM) of ω scan around 002 reflection at 30 mTorr and 190 mTorr were 1.1° and 0.52°, respectively. Since this FWHM is a parameter of crystallinity, the lower value of FWHM at 190 mTorr suggests higher quality of BPBO films. In addition, a coherent epitaxial film generally has FWHM of ω scan with less than ~ 0.1°. This implies that the effect of epitaxial strain could be negligibly weak in these BPBO films.

This difference in crystallinity was also confirmed by electrical resistance of films which was measured at room temperature by a circuit tester. Electrical resistance of films fabricated at 30 mTorr and 190 mTorr were ~ 10 kΩ and ~ 0.2 kΩ, respectively. Low electrical resistance generally suggests the high crystallinity, since the amount of impurity and the effect of domain boundary is considered to be small. These data about 2θ-θ scan, FWHM of ω scan, and the value of electrical resistance indicates that high oxygen pressure is a merit for the film growth. In the following fabrications, oxygen pressure was fixed at 190 mTorr.

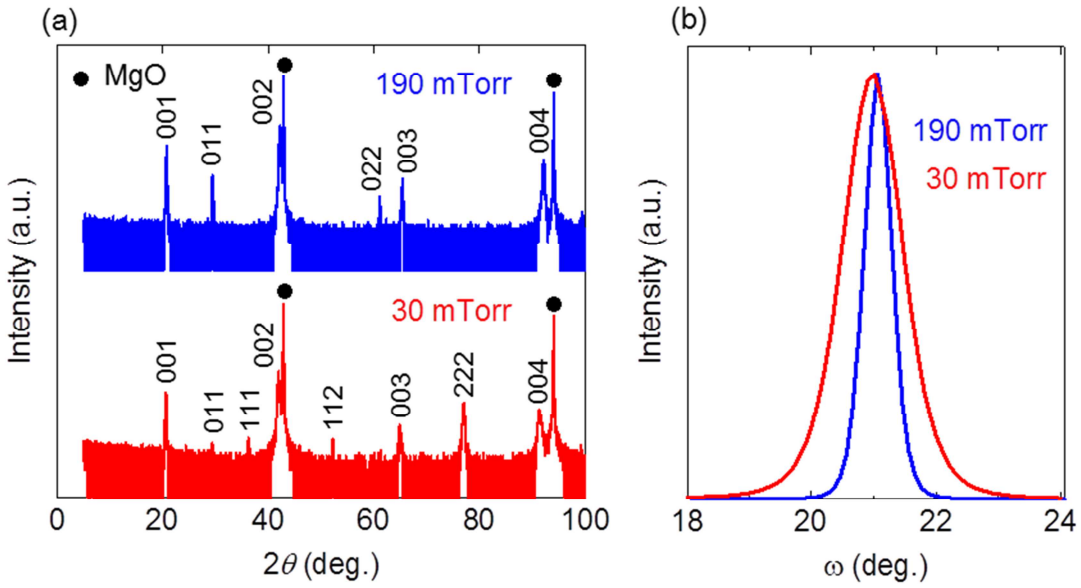

Fig. 4-1. XRD measurement of BPBO solid solution films, fabricated under several oxgen pressures. (a) 2θ–θ scan. (b) ω-scan around 002 reflection peak.

Next, the substrate temperature (T_s) during deposition was controlled at 550 °C ~ 800 °C. Figure 4-2 indicates XRD pattern of 2θ-θ scan in obtained BPBO films. XRR measurement determined that the thickness of all films was about 250 nm. At T_s = 550 °C ~ 650 °C, the peaks of XRD pattern were not assigned by only 00*l* reflection of a perovskite compound. Above T_s = 700 °C, BPBO films showed epitaxial growth along [001] direction. With further increase of temperature, the peak of 004 reflection became broader and its peak positon shifted to the lower angle at T_s = 800 °C. In addition, the film synthesized at T_s = 800 °C was too insulating to measure its electrical resistance at room temperature by a circuit tester. These behaviors of 2θ-θ scan in XRD and electrical resistance at T_s = 800 °C might be originated from the introduction of defects. Low T_s are not good for the epitaxial growth, although BPBO films deteriorate at high T_s. Therefore, T_s around 700 °C is considered to be the best temperature for realizing the epitaxial growth of BPBO films.

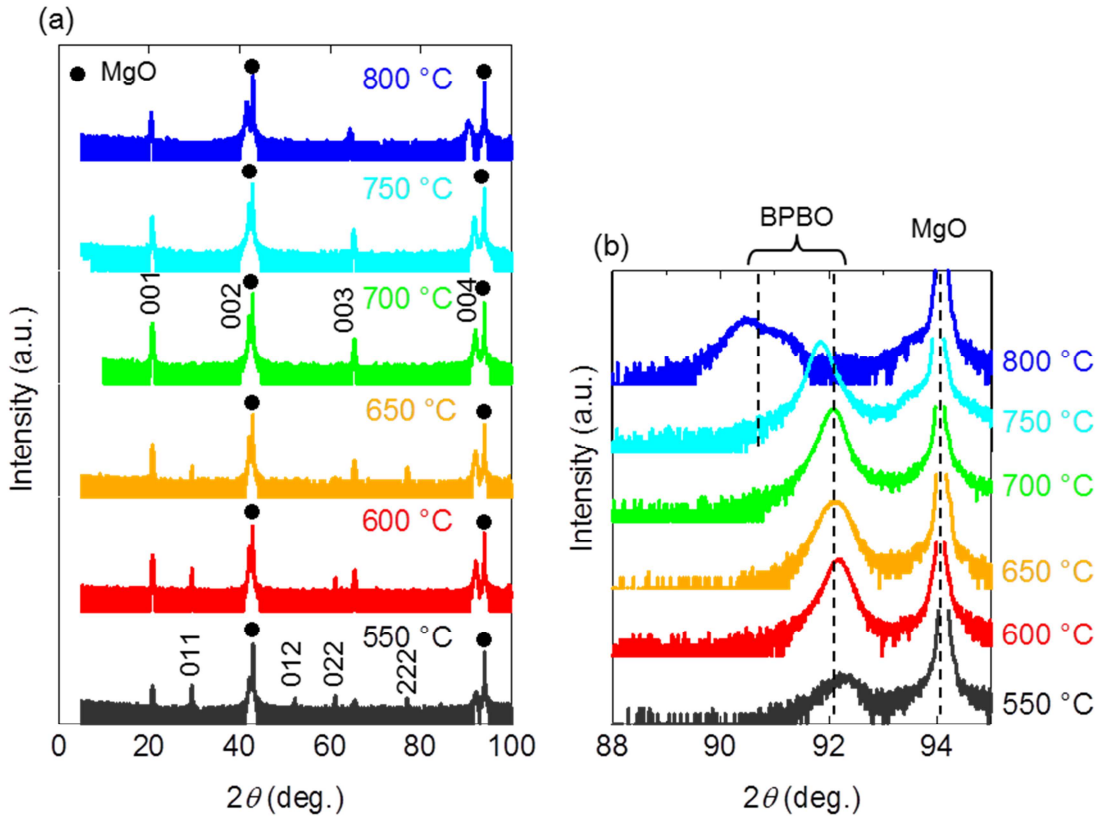

Fig. 4-2. XRD measurement of BPBO solid solution films, fabricated under several substrate temperatures. (a) Whole figure of 2θ-θ scans. (b) Expanded figure around 004 reflection peak.

Generally, thinner films are sensitive to the orientation of substrate in terms of free energy. In order to demonstrate epitaxial growth below T_s = 700 °C, BPBO film with the thickness of ~ 50 nm, ~125 nm, and ~250 nm were fabricated at T_s = 650 °C and P_{O2} = 190 mTorr (P_{O2}: oxygen pressure). Figure 4-3 shows XRD pattern of 2θ-θ scan in obtained BPBO films. The epitaxial growth of BPBO film on MgO substrate was realized at the thickness of 50 nm, while other BPBO films with the thickness of ~125 nm and ~250 nm included the peaks other than 00*l* reflections. The lattice parameter of an epitaxial BPBO film with 50 nm is estimated to be 4.277 Å from the 004 reflection. This value is comparable to the lattice parameter of bulk BPBO, suggesting that the epitaxial strain is negligibly small. Thus, at the thickness below 50 nm, epitaxial BPBO films might be obtained even at T_s lower than 700 °C.

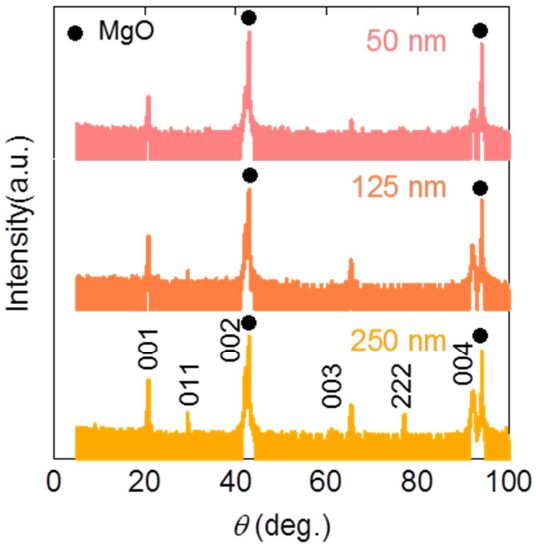

Fig. 4-3. 2θ-θ scan in XRD measurement of BPBO solid solution films. BPBO films were prepared by changing the thickness.

As Fig. 4-4 (a) indicates, the superconducting transitions were observed below T_s = 650 ℃ in the temperature dependence of magnetization. Superconducting transition temperature T_c was defined by the onset of a superconducting transition. T_c of BPBO films were smaller than the bulk value of $Ba(Pb_{0.75}Bi_{0.25})O_3$ with T_c = 12 K. In the temperature dependence of resistivity, zero resistance states inductive of superconductivity were also observed, as shown in Fig. 4-4 (b) and (c).

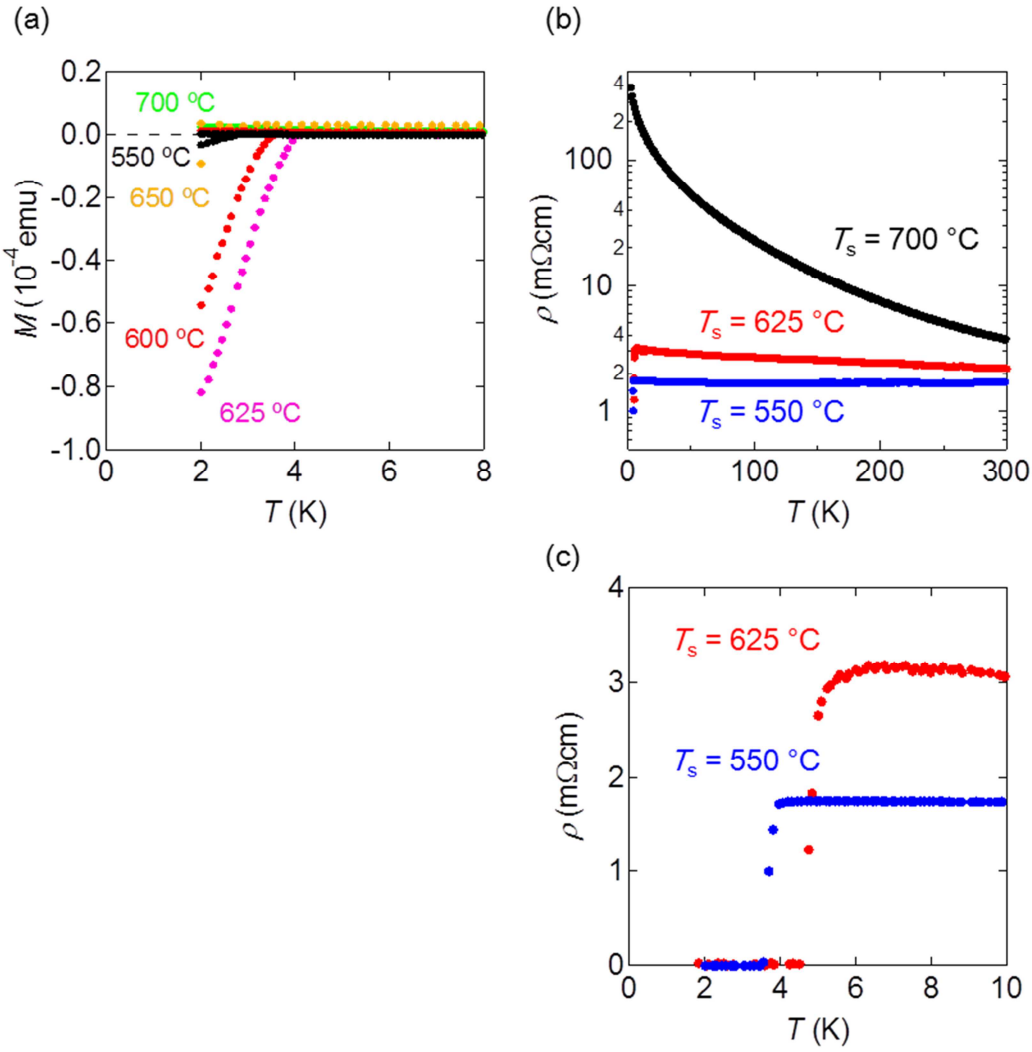

Fig. 4-4. (a) Temperature dependence of magnetic moment for BPBO films. (b), (c) Temperature dependence of resistivity for a BPBO film fabricated.

The chemical composition of BPBO films depends on T_s, as shown in Fig. 4-5 (a). In this chemical composition, we consider only Ba, Pb and Bi atoms, because the contribution of O atoms in MgO substrate was found in the SEM-EDS spectrum. Pb atoms tended to re-evaporate easily with increasing T_s. At T_s = 800°C, the ratio of Ba, Pb and Bi is quite different from the aimed value of Ba:Pb:Bi = 1:0.75:0.25, indicating there are many deficiencies in the BPBO film. This off-stoichiometry at T_s = 800°C could be the origin of high electrical resistance and the peak shift in 2θ-θ scan.

Figure 4-5 (b) shows that T_s dependence of T_c is considered to be explained partially by the chemical composition of BPBO films. That is, x, which is the ratio of Bi in the total amount of Pb and Bi, should be around 0.25 in order to realize superconductivity. However, even though x was almost 0.25, T_c at T_s = 550 °C was about 3 K which is smaller than the bulk value of $Ba(Pb_{0.75}Bi_{0.25})O_3$. This smaller T_c of BPBO films cannot be understood in terms of the Bi contents, suggesting that there are other factors to determine T_c of BPBO films.

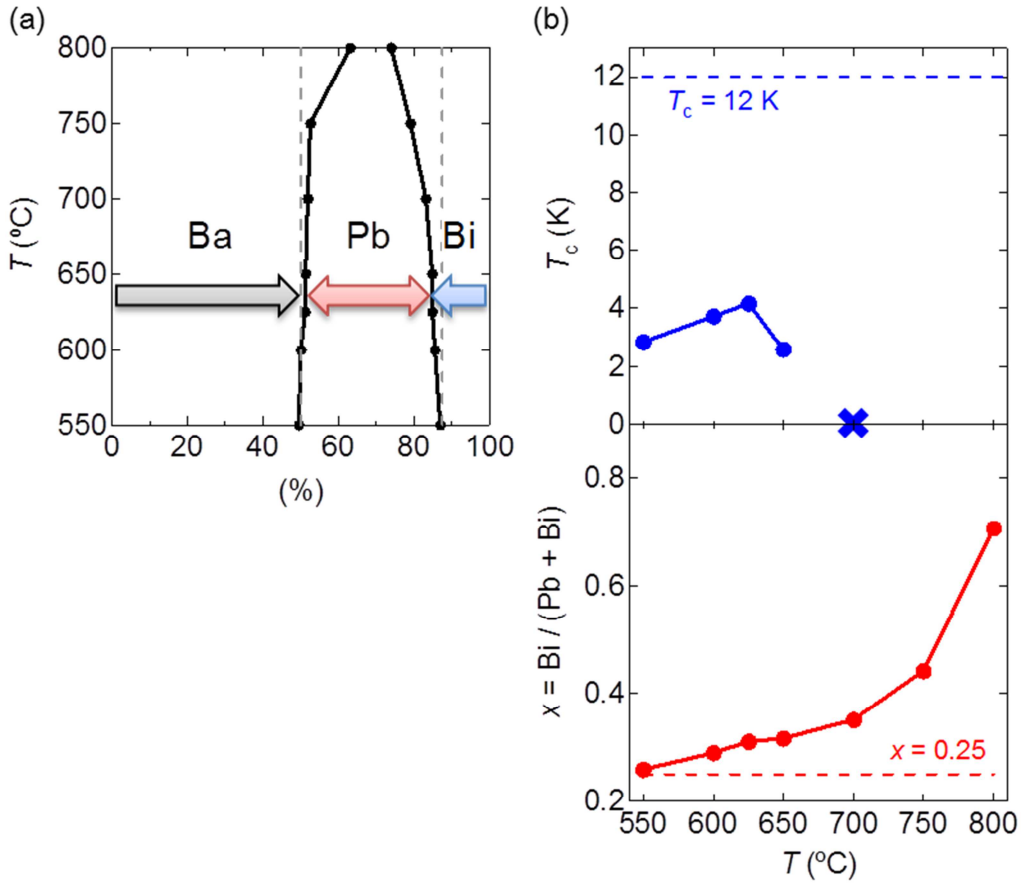

Fig. 4-5. (a) The ratio of Ba. Pb, and Bi in BPBO films. (b) Substrate temperature dependence of Bi-content x and a superconducting transition temperature T_c.

4.1.2 Fabrication by Using a Pb-rich Target Material

In order to investigate the effect of the chemical composition to superconducting properties of BPBO films further, the composition of a PLD target was changed to be $Ba(Pb_{0.75\times(1+0.22)}Bi_{0.25})O_3$, indicating 22% excess of Pb. The mixture of $BaCO_3$, PbO_2, and Bi_2O_3 powders were heated at 800 °C for 2 days. The obtained materials were pelletized for a PLD target, sintering again at 800 °C by SPS method.

BPBO films were fabricated at T_s = 550 °C ~ 700 °C by using a Pb-rich PLD target. Figure 4-6 shows 2θ-θ scan of XRD pattern for BPBO films synthesized at T_s = 650 °C and 700 °C. The thickness of these films was estimated to be ~ 50 nm. At T_s =700 °C epitaxial growth was observed, while the peak of 011 reflection was included at T_s = 650 °C. This trend at T_s = 650°C was not found in the BPBO films fabricated by using a $Ba(Pb_{0.75}Bi_{0.25})O_3$ target. This indicates that the compositional change of films might prevent from the epitaxial growth. The peak position of BPBO films around 004 reflection was the almost same at T_s = 650 °C and 700 °C. The out-of-plane lattice constants were estimated to be 4.277 Å, which is similar to that of bulk $Ba(Pb_{0.75}Bi_{0.25})O_3$. Thus, we need not consider the effect of epitaxial strain, as in the previous section.

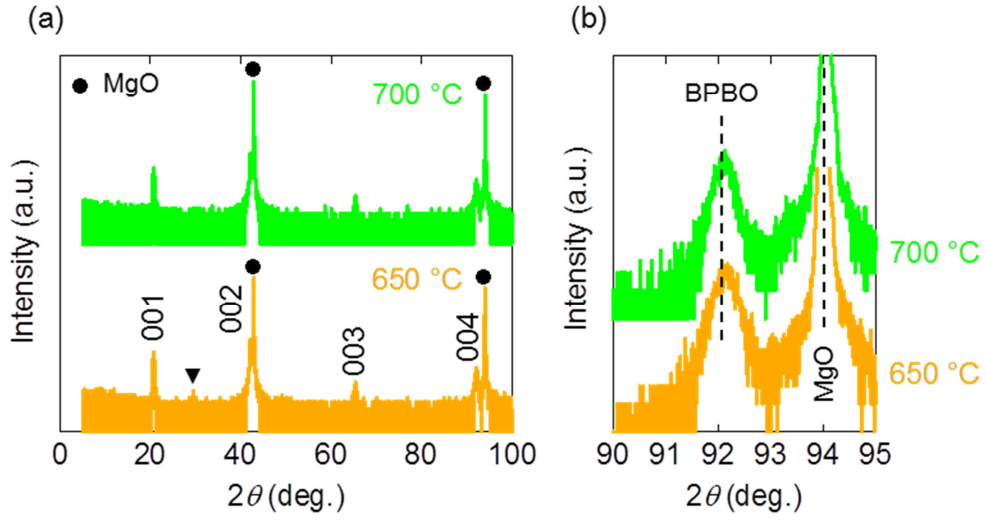

Fig. 4-6. 2θ-θ scan in XRD measurement of BPBO solid solution films using a target with the nominal composition of $Ba(Pb_{0.79\times(1+0.22)}Bi_{0.21})O_3$. (a) Whole figure of 2θ-θ scans. (b) Expanded figure around 004 reflection peak.

All BPBO films showed a superconducting transition in the temperature dependence of magnetization, as shown in Fig. 4-7 (a). While large diamagnetism was not observed at T_s = 650 °C, zero-resistance was observed in Fig. 4-7 (b), indicating the demonstration of superconductivity.

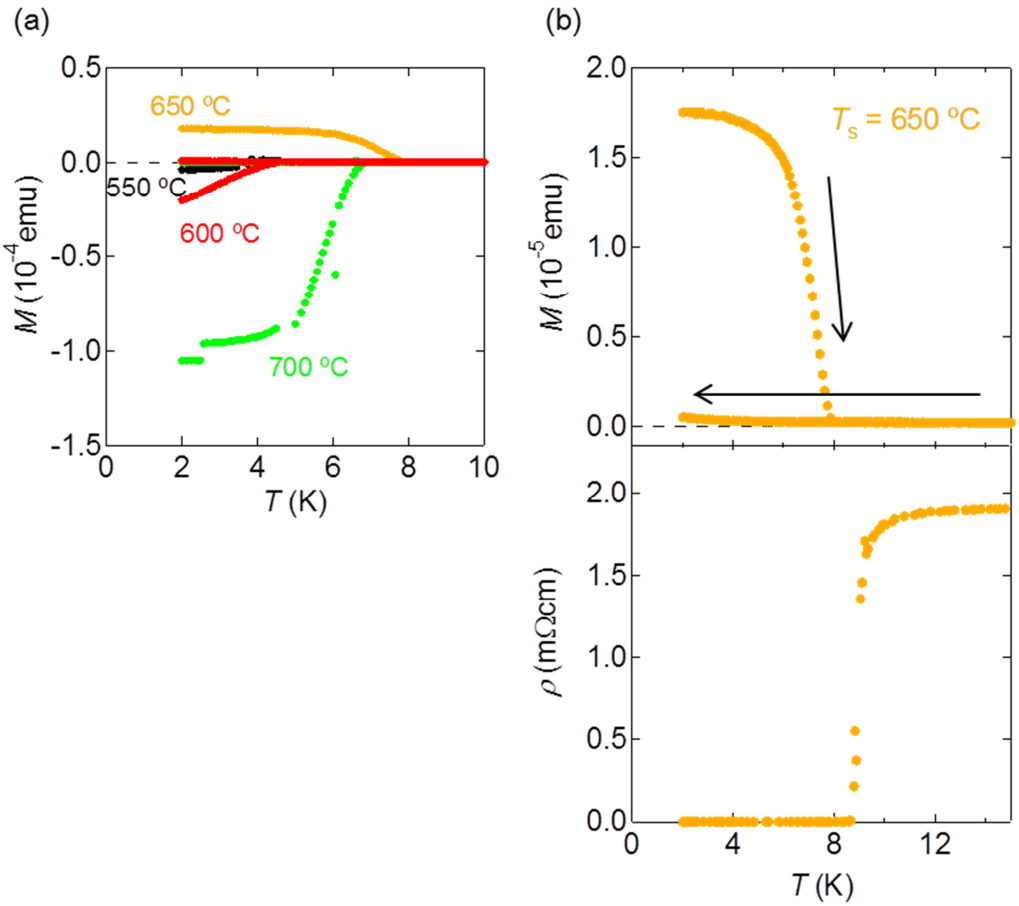

Fig 4-7. (a) Temperature dependence of magnetic moment for BPBO films (b) Temperature dependence of magnetic moment and resistivity for a BPBO film fabricated at T_s = 650 °C.

Figure 4-8 summarizes T_s dependence of the chemical composition and the superconducting properties for fabricated BPBO films. Here, T_c was defined as the onset of a superconducting transition in the magnetization. At T_s = 650°C and 700°C, the Bi content shifted to be around x = 0.25 in BPBO films which were synthesized with a Pb-rich target. At T_s = 650°C, T_c increased to 7.9 K from 2.6 K, and at T_s = 700°C, superconductivity recovered with T_c = 6.9 K. In BPBO films at other T_s, T_c was found to enhance. These enhancements of T_c indicate that the chemical composition is one of the factors to determine superconducting

properties. In addition, T_c of T_s = 650°C with a Pb-rich target is higher than that of T_s = 550°C with a stoichiometric target, while the values of x are close to 0.25 in both of BPBO films. This suggests that the epitaxial growth might realize high T_c from the comparison of XRD patterns between Fig. 4-2 and Fig. 4-6.

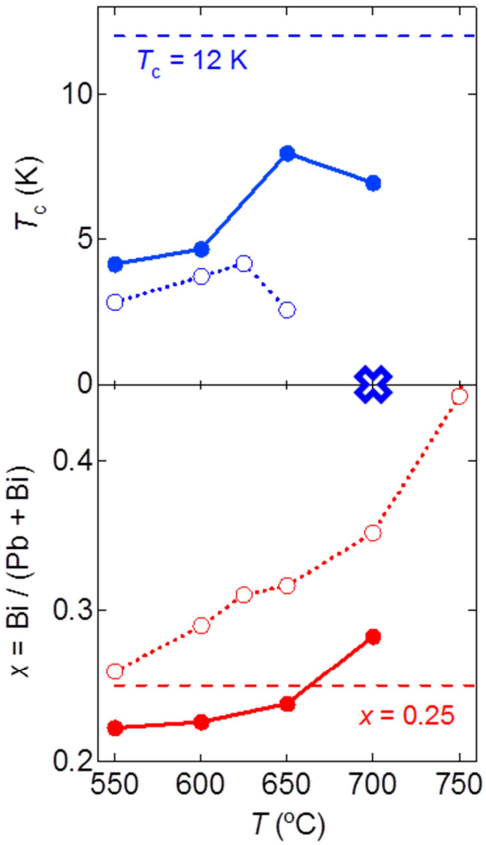

Fig. 4-8. Substrate temperature dependence of Bi-content x and a superconducting transition temperature T_c. Solid line indicates the BPBO films fabricated from Pb-rich target, while broken line show the BPBO films synthesized from stoichiometric target.

4.2 $BaPbO_3$ Films

In this part, the growth conditions of $BaPbO_3$ films were considered by referring the condition to fabricate solid-solution BPBO films as discussed in the section of 4.1. This intends to be the preparation for the fabrication of BBO/BPO heterostructures.

4.2.1 Fabrication by Using a Stoichiometric Target Compound

The target material for PLD method was prepared to be stoichiometric. Stoichiometric mixture of $BaCO_3$ and PbO_2 powder were sintered at about 800 °C for 2 days. An obtained material was pelletized and heated at 800 °C again by SPS method.

BPO films were fabricated by changing T_s from 550 °C to 750 °C. During the deposition, oxygen pressure was fixed to be 190 mTorr. Figure 4-9 indicates 2θ-θ scan of XRD pattern for fabricated BPO films with the thickness of ~ 50 nm. Epitaxial growth of a perovskite compound along [001] direction was observed above T_s = 700 °C, while the films included the peaks of 0*ll* reflection below T_s = 650 °C. This kind of temperature dependence was also found in the fabrication of BPBO films. Below T_s = 700 °C, the positions of 004 peak did not depend on T_s. This indicate that the out-of-plane lattice constant of BPO showed a constant value of 4.259 Å from T_s = 550 °C ~ 700 °C. However, at only T_s = 750 °C, the peak shifted to the lower angle, implying the out-of-plane lattice constant elongated to be 4.272 Å. FMHW of ω scan around 002 reflection did not depend on T_s, and the values of FMHW were estimated to be 1.3 ~ 1.7 ° which is relatively large. This indicates that the crystallinity of BPO films was not high at T_s = 550 °C ~ 750 °C. Thus the elongation of out-of-plain lattice constant at T_s = 750 °C is not considered to be originated from epitaxial strain.

Figure 4-10 shows T_s dependence of electrical resistance and chemical composition for BPO films. Electrical resistance of BPO film at T_s, = 750 °C measured by a circuit tester was one-order magnitude larger than at other T_s. In the chemical composition, we considered the contribution of Ba and Pb atoms, because the SEM-EDS spectrum included the contribution of O atoms in MgO substrate. Then, the ratio of Pb in BPO films was calculated as the amount of

Pb was divided by the total amount of Pb and Ba. Pb composition was almost 50 % below 600 °C, inductive of stoichiometry, but above 600 °C, the ratio of Pb decreased with increasing T_s, suggesting Pb is easy to re-evaporate at higher temperatures. This off- stoichiometry is considered to be origin of the high electrical resistance and the elongation of lattice constant at T_s = 750 °C.

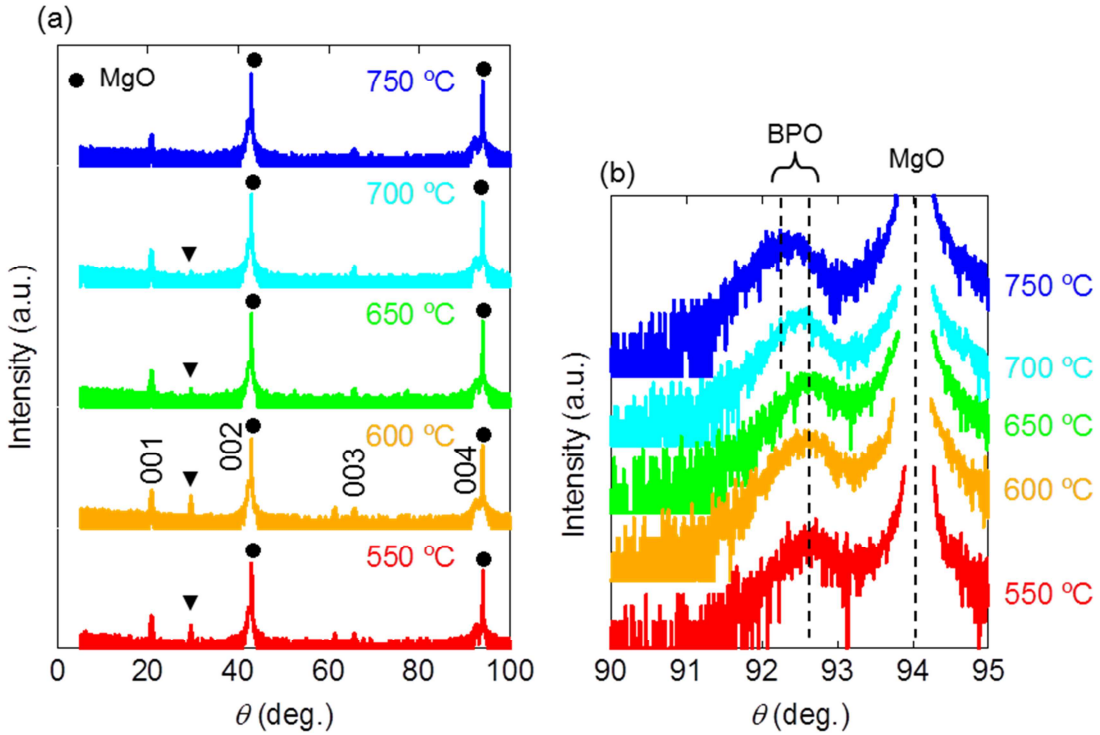

Fig. 4-9. XRD measurement of BPO films, fabricated under several substrate temperatures. (a) Whole figure of 2θ-θ scans. (b) Expanded figure around 004 reflection peak.

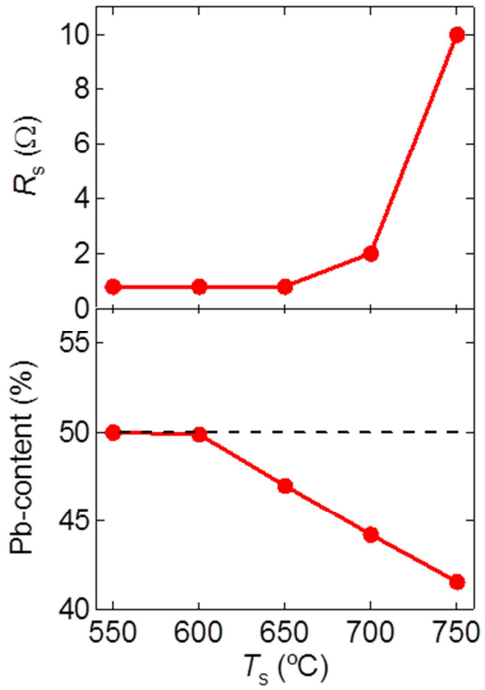

Fig. 4-10. T_s dependence of electrical resistance for BPO films. and Pb-content in BPO films.

4.2.2 Preparation for Fabrication of $BaBiO_3/BaPbO_3$ Heterostructure with Single Interface

Here, the condition of BPO film growth was considered for the fabrication of BBO/BPO heterostructure with single interface. From previous section, it was found that Pb atoms were easier to re-evaporate than Ba atoms. In order to compensate the rack of Pb atoms, the target of BPO where the amount of Pb is rich should be prepared. The nominal compositions of PLD targets were set to be Ba:Pb = 1:1.11 ($BaPb_{1.11}O_{3+\delta}$) and Ba:Pb = 1:1.25 ($BaPb_{1.25}O_{3+\delta}$). Both of target materials were prepared by sintering the mixture of $BaCO_3$ and PbO_2 powder at 800 °C for 2 days. Sintered materials of $BaPb_{1.11}O_{3+\delta}$ and $BaPb_{1.25}O_{3+\delta}$ were pelletized and heated again by SPS method at 700 °C and 650 °C, respectively.

BPO films were synthesized at several T_s, by using $BaPb_{1.11}O_{3+\delta}$ and $BaPb_{1.25}O_{3+\delta}$ targets. During deposition, oxygen pressure was fixed to be 190 mTorr. Figure 4-11 shows the

the XRD patterns of 2θ-θ scan for BPO films which were fabricated from a $BaPb_{1.09}O_{3+\delta}$ target, These BPO films had the thickness of ~ 20 nm. At T_s = 600 °C ~ 700 °C, BPO films performed the epitaxial growth along [001] direction, while BPO film fabricated at T_s = 750 °C included the peaks of 011 reflection. BPO films were found to demonstrate the epitaxial growth around T_s = 650 °C, given the thickness of ~ 20 nm. The position of peaks around 002 reflection depended on T_s. At T_s = 650 °C ~ 750 °C, The positions of peak were almost the same, while the position shifted to higher angle at T_s = 600 °C. From these peak positions, the out-of-plane lattice constants of BPO films were calculated to be 4.290 Å at T_s = 650 °C ~ 750 °C and 4.263 Å at T_s = 600 °C. The out-of-plane lattice parameter at T_s = 600 °C was almost the same with bulk value of BPO, indicating that there was not the epitaxial stain effect from MgO substrate. The elongation of lattice constants at T_s = 650 °C ~ 750 °C is considered to be originated from the degradation of films rather than the epitaxial stain. The epitaxial stained films generally have a high crystallinity, but FWHM of ω scan around 002 reflection is about 1.0 ° at T_s = 650 °C ~ 750 °C which is larger than 0.12 at T_s = 600 °C.

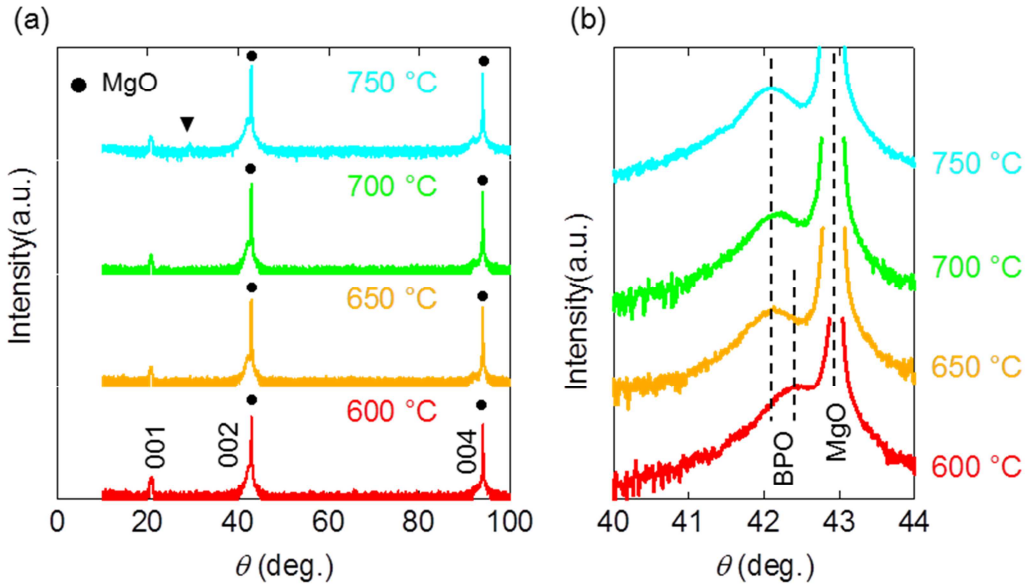

Fig. 4-11. XRD measurement of BPO films, fabricated under several substrate temperatures by using $BaPb_{1.09}O_{3+\delta}$ target. (a) Whole figure of 2θ–θ scans. (b) Expanded figure around 002 reflection peak.

Electrical resistance measured by a circuit tester become larger at higher T_s, as observed in the films fabricated by using stoichiometric target as mentioned in the section of 4.2.1. At T_s = 600 °C ~ 700 °C electrical resistance is about 10 kΩ, and the film at T_s = 750 °C was highly insulating to measure electrical resistance.

Figure 4-12 shows the 2θ-θ scan of XRD pattern for the BPO films which were synthesized from a $BaPb_{1.25}O_{3+\delta}$ target. The fabrication was done at T_s = 675 °C ~ 750 °C, and oxygen pressure was kept at 190 mTorr. The thickness of all BPO films was estimated to be ~ 40 nm which was twice longer than that of films fabricated from a $BaPb_{1.11}O_{3+\delta}$ target. All BPO films did not realize the epitaxial growth along [001] direction, including the peaks of 011 reflection. The intensity of Bragg peak which was assigned by 011 reflection enhanced relatively in comparison with the peak of 001 reflection, as T_s increased. This temperature dependence of peak intensity indicates that the BPO films with high orientation are easy to be obtained at higher T_s. The position of peaks around 002 reflection did not depend on T_s. Then the out-of-plane lattice constant of BPO films was almost the same value at T_s = 675 °C ~ 750 °C. These lattice constants of BPO films were estimated to be 4.266 Å which was similar to bulk value, indicating that epitaxial stain from substrate can be neglected. Electrical resistance of BPO films which were measured by a circuit tester increased from 0.5 kΩ to 2 kΩ with rising T_s. This T_s dependence of electrical resistance is similar to that of BPO films which were fabricated by using other target materials of $BaPbO_3$ and $BaPb_{1.11}O_{3+\delta}$.

At last, we estimated Pb content in the total amount of Ba and Pb for obtained BPO films. In this estimation, the amount of O atoms was not considered for the reason described in the section of 4.2.1. At all T_s, the content of Pb increased from BPO films fabricated by using stoichiometric $BaPbO_3$ target, as shown in Fig 4-13. This indicates the compensation of re-evaporation of Pb atoms. However, the chemical composition of BPO films showed similar value and temperature dependence in $BaPb_{1.11}O_{3+\delta}$ and $BaPb_{1.25}O_{3+\delta}$. That is surprising because the different composition of target materials were used during the deposition of films.

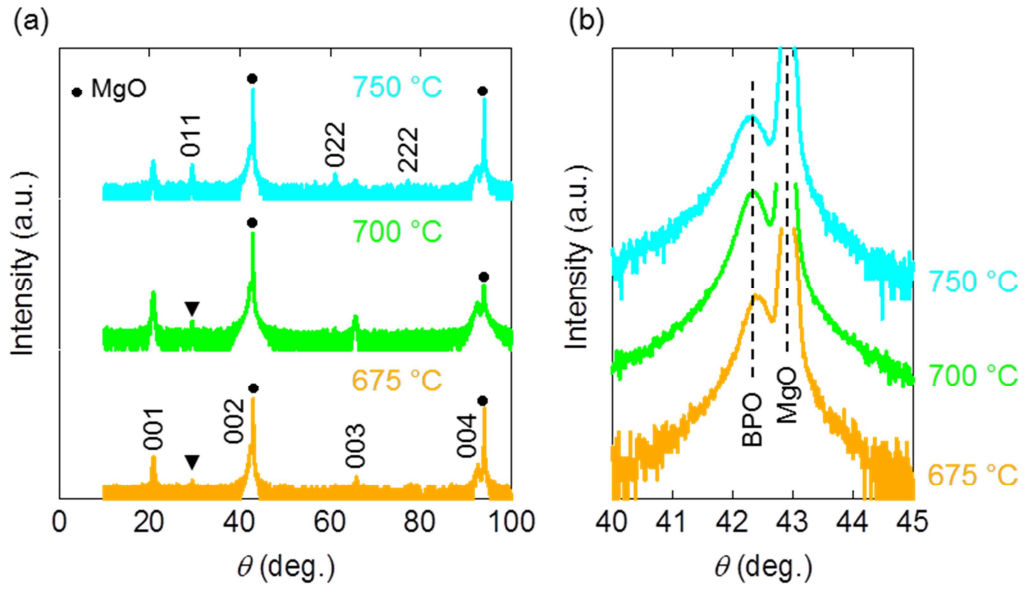

Fig. 4-12. XRD measurement of BPO films, fabricated under several substrate temperatures by using $BaPb_{1.25}O_{3+\delta}$ target. (a) Whole figure of 2θ–θ scans. (b) Expanded figure around 002 reflection peak.

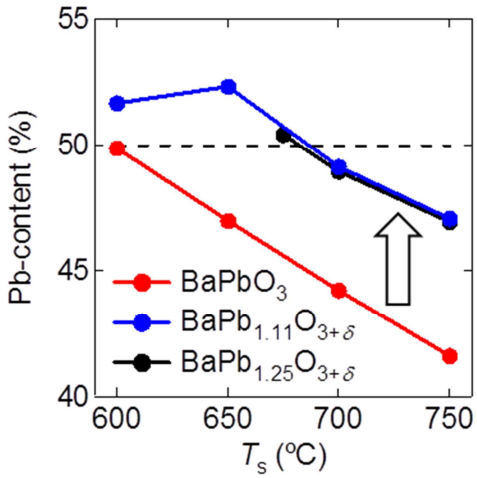

Fig. 4-13. T_s dependence of Pb contents in BPO films. Red line, blue line, and black line correspond to films fabricated from the targets of $BaPbO_3$, $BaPb_{1.11}O_{3+\delta}$ and $BaPb_{1.25}O_{3+\delta}$, respectively.

4.2.3 Preparation for Fabrication of $BaBiO_3/BaPbO_3$ Superlattice Films

For the growth of BBO/BPO superlattices, we used the PLD chamber which was different from that used in the fabrication of BBO/BPO heterostructures with single interface. In this section, the fabricating condition for of BPO films and was optimized again in order to synthesize BBO/BPO superlattices.

In the previous sections of 4.2.1 and 4.2.2, we confirmed that Pb atoms were easy to re-evaporate in BPO films. In order to compensate the rack of Pb atoms, the targets of BPO which contained the excess amount of Pb were prepared. The nominal composition of PLD target was set to be Ba:Pb = 1:1.11 ($BaPb_{1.11}O_{3+\delta}$) and Ba:Pb = 1:1.20 ($BaPb_{1.20}O_{3+\delta}$). Both of target materials were prepared by heating the mixture of $BaCO_3$ and PbO_2 powder at 800 °C for 2 days. Sintered materials of $BaPb_{1.11}O_{3+\delta}$ and $BaPb_{1.20}O_{3+\delta}$ were pelletized and sintered again by SPS method at 700 °C and 750 °C, respectively.

BPO films were synthesized at several T_s, by using $BaPb_{1.11}O_{3+\delta}$ and $BaPb_{1.20}O_{3+\delta}$ target. During the fabrication, the oxygen pressure was fixed to be 190 mTorr. Figure 4-14 shows the XRD patterns of 2θ-θ scan for BPO films which were fabricated from $BaPb_{1.11}O_{3+\delta}$. In a $BaPb_{1.11}O_{3+\delta}$ target, the thickness of all BPO films was estimated to be about 50 nm. At T_s = 600 °C ~ 700 °C, BPO films did not perform the epitaxial growth, including the peaks of 011 reflection. The position of peaks around 004 reflection did not depend on T_s, indicating that the out-of-plane lattice constant of BPO films did not change at T_s = 600 °C ~ 700 °C. The values of out-of-plane lattice constant were calculated to be 4.254 Å which agree with the bulk data of BPO. This indicates that the effect of epitaxial strain is negligibly small, like BPO films in previous sections.

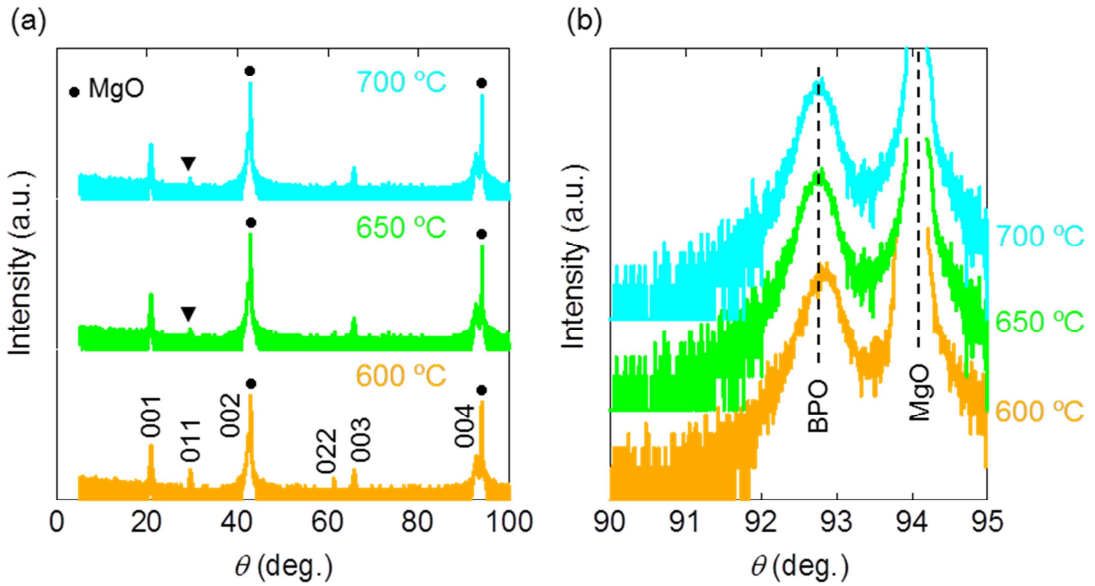

Fig. 4-14. XRD measurement of BPO films, fabricated under several substrate temperatures by using $BaPb_{1.11}O_{3+\delta}$ target. (a) Whole figure of 2θ-θ scans. (b) Expanded figure around 004 reflection peak.

Figure 4-15 indicates the XRD patterns of 2θ-θ scan for the BPO films which were fabricated from $BaPb_{1.20}O_{3+\delta}$. All of these BPO films had the thickness of ~ 50 nm. At T_s = 650 °C and 700 °C, BPO films demonstrated the epitaxial growth, while BPO film at T_s = 600 °C included the peaks of 0*ll* reflections. The positions of peaks around 004 reflection depended on T_s. At T_s = 650 °C, the peak of 004 reflection was the sharpest, and the out-of-plane lattice constant was calculated to be 4.259 Å which is the almost same value as bulk. On the other hand, at T_s = 600 °C and 700 °C, the peaks became broader, indicative of lower crystallinity, and their position moved to the lower angle region, implying that out-of-plane lattice constants were elongated to be 4.277 Å and 4.275 Å, respectively.

The Pb content increased from that of BPO films fabricated with a stoichiometric $BaPbO_3$ target, indicating the compensation of re-evaporation of Pb, as shown in Fig 4-16. However, the chemical composition of BPO films, which were synthesized from target materials of $BaPb_{1.11}O_{3+\delta}$ and $BaPb_{1.20}O_{3+\delta}$, showed similar value with the same T_s dependence. That is surprising, because the composition of target materials were different. In the section of 4.2.2, we also observed this trend that the chemical composition of films did not depend on some target materials.

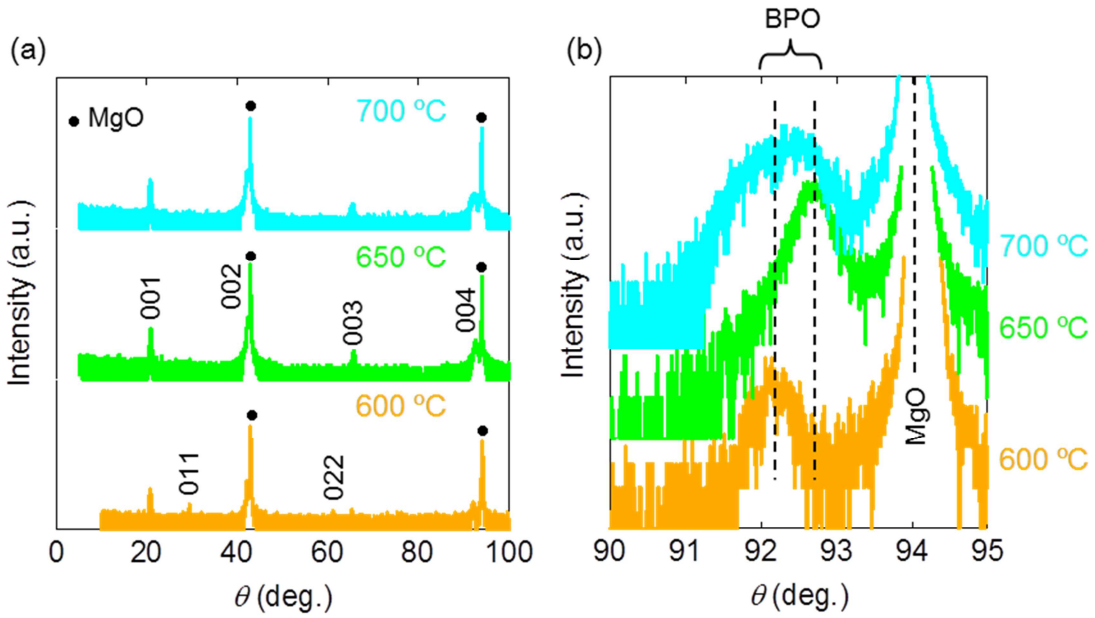

Fig. 4-15. XRD measurement of BPO films, fabricated under several substrate temperatures by using $BaPb_{1.20}O_{3+\delta}$ target. (a) Whole figure of 2θ-θ scans. (b) Expanded figure around 004 reflection peak.

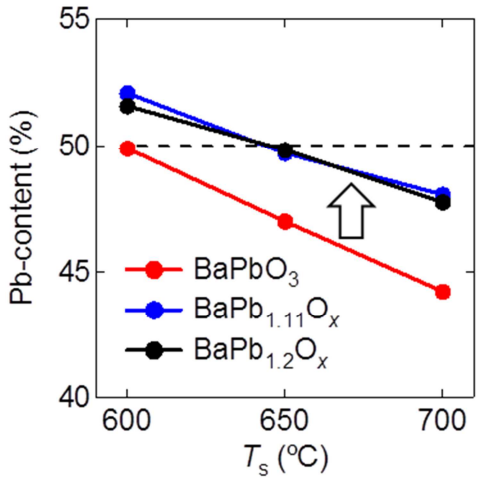

Fig. 4-16. T_s dependence of Pb contents in BPO films. Red line, blue line, and black line indicates Pb contents of BPO films fabricated from the targets of $BaPbO_3$, $BaPb_{1.11}O_{3+\delta}$ and $BaPb_{1.2}O_{3+\delta}$ respectively.

4.3 $BaBiO_3$ Films

In this section, the fabricating conditions for BBO films were optimized in order to synthesize BBO/BPO heterostructures. By consulting the growth conditions of BPBO and BPO films, we investigated the conductions of synthesizing BBO films.

4.3.1 Fabrication by Using a Stoichiometric Target Compound

The target material for the fabrication of BBO films was prepared to be stoichiometric. Stoichiometric mixture of $BaCO_3$ and Bi_2O_3 powders was sintered around 800 °C for 2 days. Sintered material was pelletized and heated again at 600 °C by SPS method.

BBO films were fabricated by controlling T_s from 550 °C to 750 °C, and oxygen pressure was set to be 190 mTorr. Figure 4-17 indicates XRD pattern of 2θ-θ scan for fabricated BBO films whose thickness was estimated to be ~ 50 nm. Below T_s = 700 °C, the Bragg peaks, except for those of MgO substrate, are considered to be associated with 00l reflections of perovskite-type structure. At T_s = 750 °C, other extra peaks around 001 reflection were appeared in addition to the peaks from a [001] oriented perovskite-type compound. The positions of 004 peaks depended on T_s. Below 650 °C, the peak positions of the 004 reflection were the almost same, indicating the out-of plane lattice constant of BBO films showed a constant value of 4.335 Å which is similar to the bulk value of BBO. The peaks shifted to the lower angle area with increasing T_s. This change in the peak positions indicates the elongation of out-of plane lattice constant, whose values were 4.344 Å at T_s = 700 °C and 4.365 Å at T_s = 750 °C. FWHM of ω scan around 002 reflection were ~ 0.6° at T_s = 550 °C ~ 750 °C, implying the crystallinity did not depending on T_s. Thus, the change of lattice constant at T_s = 750 °C is considered to be originated from not the epitaxial stain from MgO substrate, but the degradation of film quality. Extra peaks around 001 reflection might suggest the appearance of impurity phases.

All BBO films were too insulating to measure electrical resistance by a circuit tester. This large resistance is thought to be originated from the charge order state formed in BBO films. The impurity phases at T_s = 750 °C was also considered to show insulating properties.

The chemical composition of BBO films depended on T_s, as shown in Fig. 4-18. In analysis of the chemical composition, we took care about only Ba and Bi atoms, since the contribution of O atoms in MgO substrate was observed in the SEM-EDS spectrum. The ratio of Bi was calculated to divide by the total amount of Bi and Ba. BBO films took apart from stoichiometry at T_s = 550 °C ~ 750 °C, and Ba atoms were easy to re-evaporate at higher temperatures. It is still not clear that the elongation of out-of-plane lattice constant and the sudden presence of impurity phase were related to this off-stoichiometry of BBO film at T_s = 750 °C.

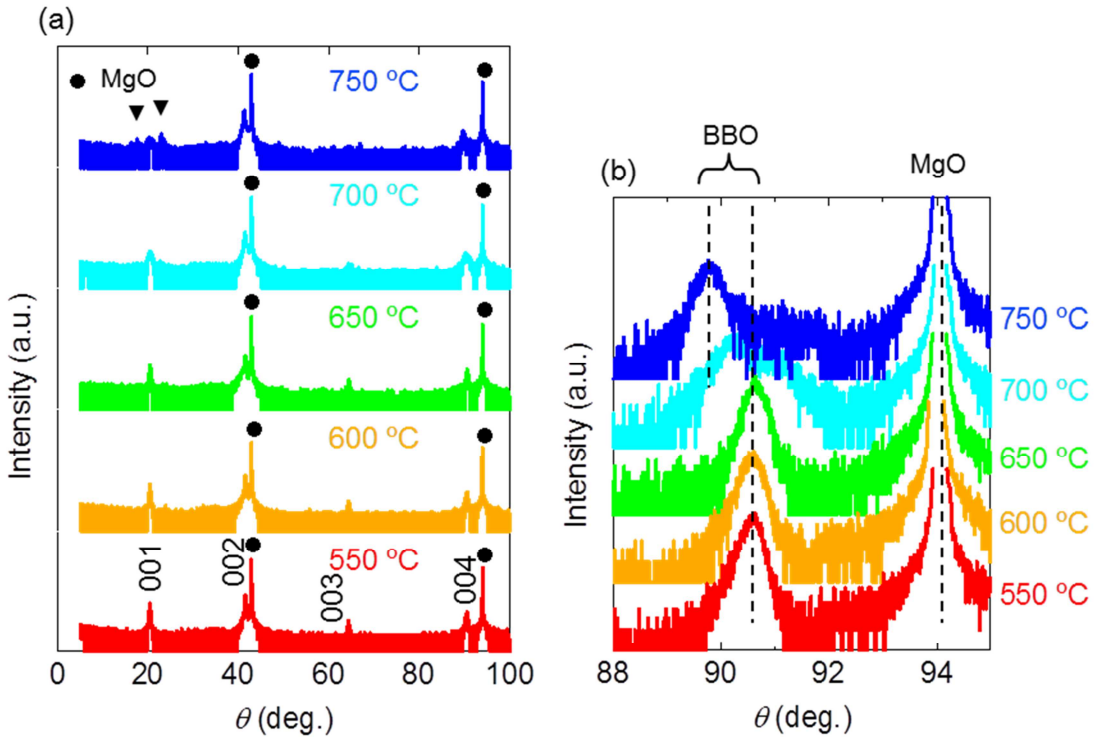

Fig. 4-17. XRD measurement of BBO films, fabricated under several substrate temperatures T_s. (a) Whole figure of 2θ-θ scans. (b) Expanded figure around 004 reflection peak.

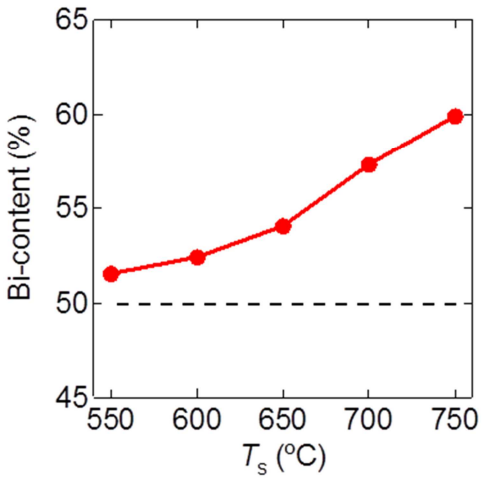

Fig. 4-18. T_s dependence of Bi content in BBO films.

4.3.2 Preparation for Fabrication of $BaBiO_3/BaPbO_3$ Heterostructures with Single Interface

The growth condition of BBO films should be optimized in order to fabricate BBO/BPO heterostructures with single interface. From the previous section, it was found that Ba atoms were easy to re-evaporate in the deposition of BBO films. For the compensation of the rack of Ba atoms, the target materials in the synthesis of BBO films should include excess Ba atoms. The nominal composition of a PLD target was set to be Ba:Bi = 1.12:1 ($Ba_{1.12}BiO_{3+\delta}$). The target material was prepared by sintering the mixture of $BaCO_3$ and Bi_2O_3 powders at 600 °C for 2 days. Sintered materials were pelletized and heated again at 700 °C by SPS method.

BBO films were synthesized by changing T_s from 600 °C to 750 °C. Figure 4-19 shows the XRD patterns of 2θ–θ scan for the BBO films which were fabricated from $Ba_{1.12}BiO_{3+\delta}$ The thickness of all BBO films was fixed ~ 40 nm. At T_s = 600 °C ~ 750 °C, BBO films performed the epitaxial growth along 001 direction. The position of Bragg peak of 004 reflection did not depend on T_s. This indicate that the out-of- plane lattice constants in BBO films took the same value which were estimated to be 4.336 Å. This lattice parameter is close to

that of bulk BBO, suggesting that the epitaxial strain can be ignored as in the BBO films grown by using a stoichiometric BBO target. In addition, there were no extra peak 001 reflection at T_s = 750 °C which was different from the BBO film synthesized from a stoichiometric BBO target. All BBO films were too insulating to measure electrical resistance by a circuit tester. This indicates that the charge order state was stabilized in BBO films as fabricating with a stoichiometric BBO target.

Figure 4-20 shows T_s dependence of Bi composition. In the analysis of the chemical composition by SEM-EDS, the obtained spectrums included the contribution from MgO substrate. The amount of oxygen is considered to be unreliable when the compositions of BBO were evaluated, as mentioned in the previous section. Thus, we dealt with the ratio of Bi in the total amount of Ba and Bi. The Bi content decreased at all T_s from that of BBO films fabricated with stoichiometric $BaBiO_3$ target, implying that BBO films were close to being stoichiometric. This compensation for re-evaporation of Ba atoms might be related with disappearance of peaks near 001 reflection at T_s = 750 °C.

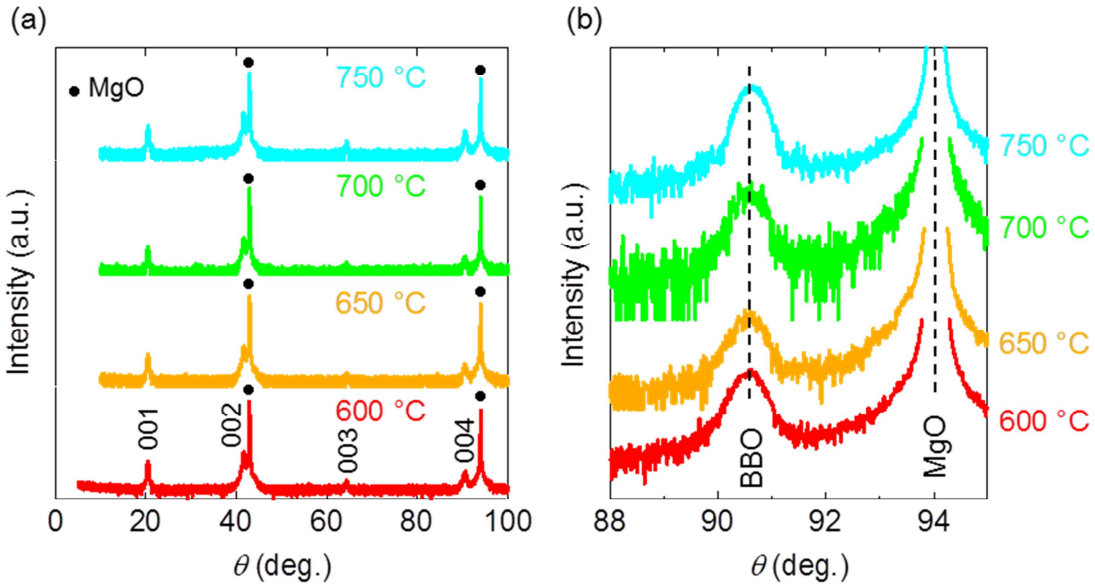

Fig. 4-19. XRD measurement of BBO films, fabricated under several substrate temperatures by using $Ba_{1.12}BiO_{3+\delta}$ target. (a) Whole figure of 2θ-θ scans. (b) Expanded figure around 004 reflection peak.

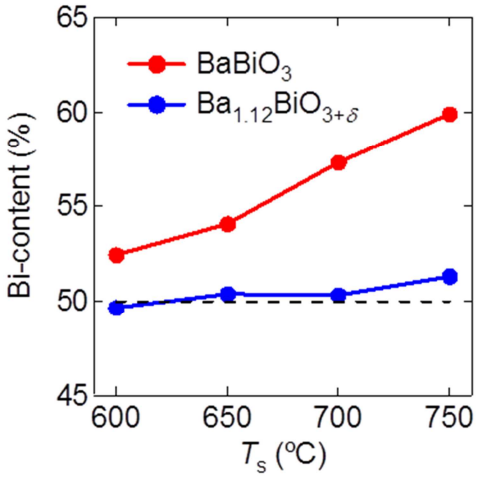

Fig. 4-20. T_s dependence of Bi contents in BBO films. Red line, and blue line shows Bi content of BBO films fabricated from the target of $BaBiO_3$ and $Ba_{1.12}BiO_{3+\delta}$ respectively.

4.3.3 Preparation for Fabrication of $BaBiO_3/BaPbO_3$ Superlattice Films

For the growth of BBO/BPO superlattices, we used the PLD chamber which was different in the fabrication of BBO/BPO heterostructures with single interface, as noted in the section of 4.2.3. In this section, the fabricating condition for BBO films was optimized again in order to synthesize BBO/BPO superlattices.

In the section of 4.3.1, we found that Ba atoms were easy to re-evaporate in the growth process of BBO films. In order to compensate the rack of Ba atoms, the target materials of BBO with the rich amount of Ba were prepared. The nominal compositions of PLD targets were set to be Ba:Bi = 1.09:1 ($Ba_{1.09}BiO_{3+\delta}$) and Ba:Bi = 1.15:1 ($Ba_{1.15}BiO_{3+\delta}$). Both of target materials were prepared by sintering the mixture of $BaCO_3$ and Bi_2O_3 powder at 800 °C for 2 days. Sintered materials were pelletized and heated again at 600 °C by using SPS method.

BBO films were deposited at T_s = 550 °C ~ 700 °C, by ablating $Ba_{1.09}BiO_{3+\delta}$ and $Ba_{1.15}BiO_{3+\delta}$targets. In the fabrication of BBO films, oxygen pressure was fixed to be 190 mTorr. Figure 4-21 indicates the XRD patterns of 2θ-θ scan for the BBO films which were

synthesized from $Ba_{1.09}BiO_{3+\delta}$. In $Ba_{1.09}BiO_{3+\delta}$ target, the thickness of all BBO films was ~ 50 nm. At all T_s, BBO films performed the epitaxial growth. The position of peaks around 004 reflection did not depend on T_s, and the out-of-plane lattice parameters were estimated to be 4.336 Å in all BBO films. This lattice constant of BBO films was similar to the reported bulk data, indicating that BBO films were not affected by the epitaxial strain from MgO substrate.

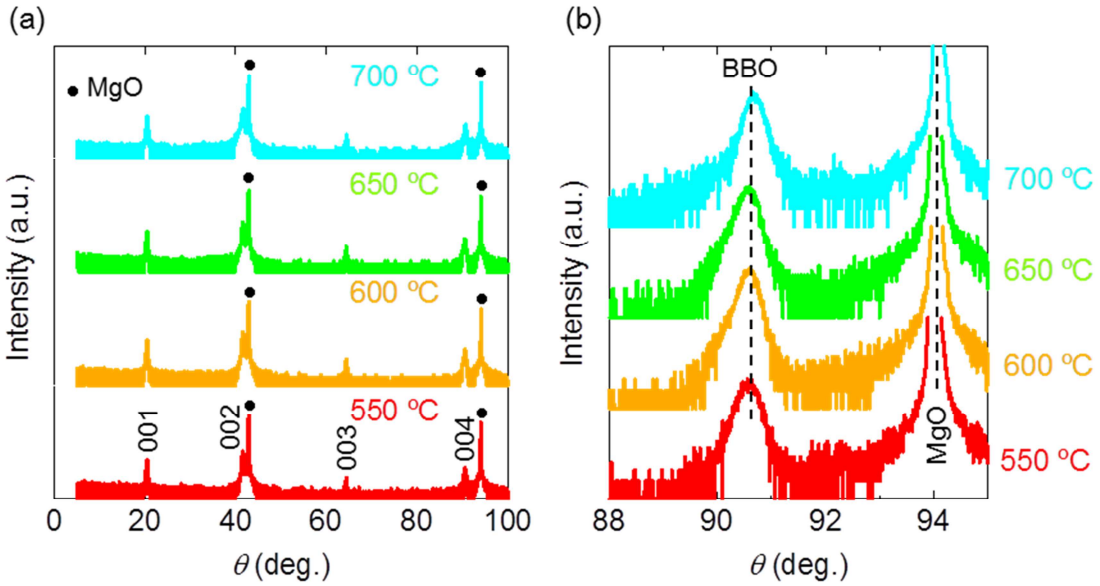

Fig. 4-21. XRD measurement of BBO films, fabricated under several substrate temperatures by using $Ba_{1.09}BiO_{3+\delta}$ target. (a) Whole figure of 2θ–θ scans. (b) Expanded figure around 004 reflection peak.

Figure 4-22 shows the XRD patterns of 2θ-θ scan for the BBO films which were fabricated from $Ba_{1.15}BiO_{3+\delta}$. In $Ba_{1.15}BiO_{3+\delta}$ target, the thickness of all BBO films was ~ 50 nm. At T_s = 600 °C and 650 °C, BBO films demonstrated the epitaxial growth. and the peaks around 004 reflection were located at the same positions. This indicates that the out-of plane lattice constant of BBO film did not change at T_s = 600 °C and 650 °C. The value of lattice constant was estimated to be 4.339 Å. This lattice constant of BBO films was close to the bulk value of BBO, implying that the effect of epitaxial strain could be ignored as in other BBO films fabricated from different target materials.

All BBO films fabricated from $Ba_{1.09}BiO_{3+\delta}$ and $Ba_{1.15}BiO_{3+\delta}$ targets were too insulating to measure electrical resistance by a circuit tester. These highly insulating properties suggest that the charge order state was realized in BBO films, like in bulk BBO.

In addition, we investigated the chemical composition of BBO films by estimating the ratio of Bi in the total amount of Ba and Bi. In this evaluation, the content of O atom was ignored, and the reason was descried in the previous sections. As shown in Fig. 2-23, T_s dependence of Bi composition did not depend on the used PLD targets, indicating that Ba is easy to re-evaporate at high T_s. By changing the composition of target materials, Bi content decreased systematically. This implies that the compensation of re-evaporation of Ba atoms was performed.

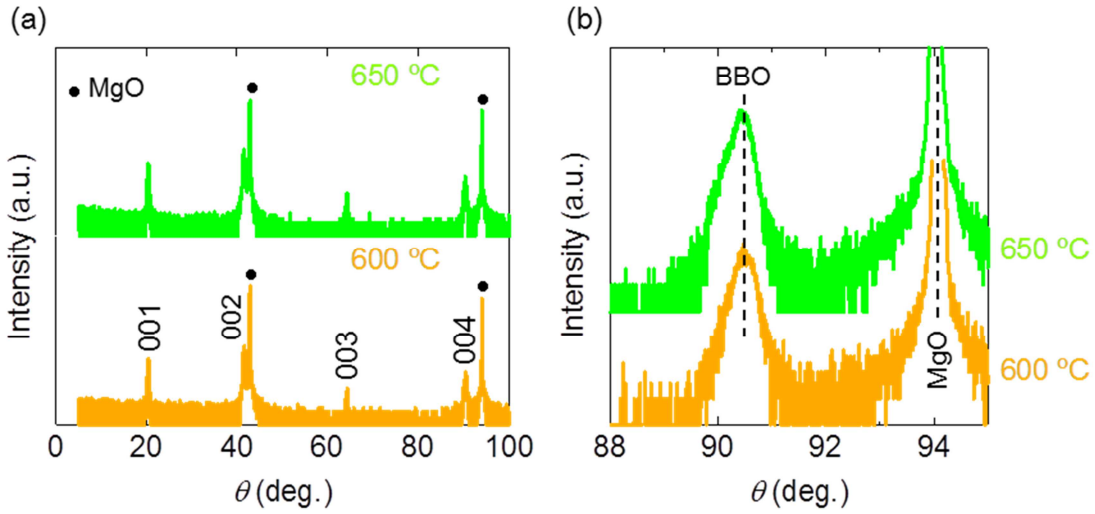

Fig. 4-22 XRD measurements of BBO films, fabricated under several substrate temperatures by using $Ba_{1.15}BiO_{3+\delta}$ target. (a) Whole figure of 2θ–θ scans. (b) Expanded figure around 004 reflection peak.

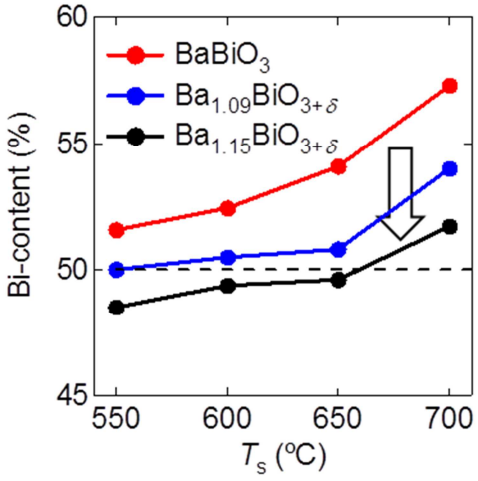

Fig. 4-23. T_s dependence of Bi contents in BBO films. Bi contents of BBO films fabricated from the target of $BaBiO_3$, $Ba_{1.09}BiO_{3+\delta}$ and $Ba_{1.15}BiO_{3+\delta}$ are indicated by red line, blue line, and black line, respectively.

4.4 Characterization of BBO_{75} Film and BPO_{25} Film

Before the investigation of BBO/BPO interface states, we clarified crystal structures and physical properties of BPO_{25} (25 unit cells ~ 11 nm)/sub and BBO_{75} (75 unit cells ~ 33 nm)/sub which are components of BBO/BPO heterostructures with single interface as discussed in chapter 5.

The XRD pattern of 2θ-θ scan indicates that BPO_{25} and BBO_{75} films were epitaxial grown on MgO(001) substrate. In Fig. 4-24(a), the Bragg peaks, except for those of MgO substrate, are considered to be originated from 00*l* reflections of perovskite-type structure. From the peaks of 004 reflection, the out-of-plane lattice constants of BBO and BPO were calculated to be 4.338 Å and 4.264 Å, respectively. These values are comparable with those of bulk materials of BBO and BPO, indicating that these films are thought to perform the fully relaxed growth.

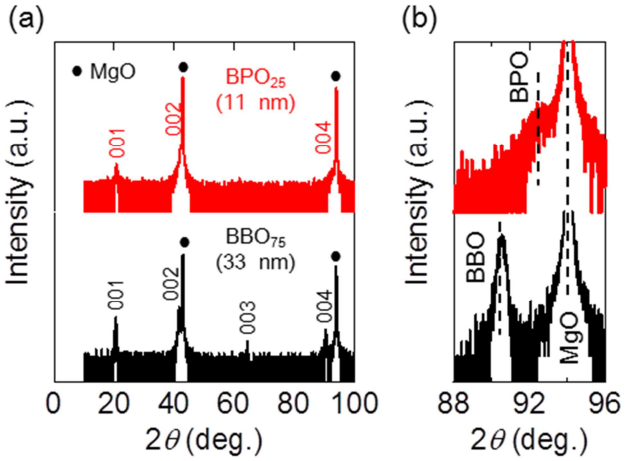

Fig. 4-24. XRD patterns of 2θ–θ scan for BPO_{25}/sub (red line) and BBO_{75}/sub (black line). (a) Wide range of 2θ–θ scan. (b) Peaks from 004 reflection.

BPO_{25} film did not show superconductivity above 2.0 K, and the resistivity is higher than that of bulk BPO, which is reported to be a semi-metal with the resistivity ~ 0.3 mΩcm at room temperature [18], as shown in Fig. 4-25. The low temperature logarithmic increase of resistivity as a function of temperature in BPO_{25} film (inset of Fig. 4-25) is likely ascribed to the effect of localization which is often discussed in two-dimensional metal [81]. BBO_{75} film did not show a superconducting transition, either. The resistivity of BBO_{75} film was too high to measure, implying that charge order state is preserved in the thin film of BBO.

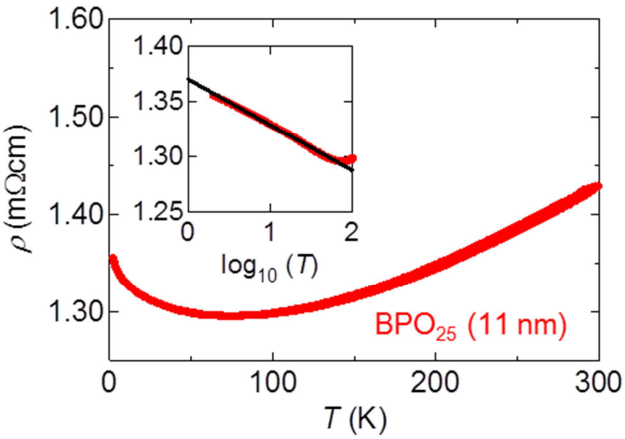

Fig. 4-25. (a) Temperature dependence of resistivity for BPO_{25} (11 nm). Inset of (a) shows a log plot of resistivity below 10 K.

4.5 Summary of This Chapter

In the fabrication of BPBO films, high oxygen pressure was found to increase the quality of films. Oxygen pressure during deposition is fixed to be 190 mTorr in the following fabrication of films. The chemical composition of BPBO films depended on T_s, and affected the superconducting properties. By changing the chemical composition of target materials, the composition of BPBO films was modulated, inducing that superconducting T_c was enhanced in BPBO films. The highest T_c was observed to be 7.9 K in solid solution BPBO films of this study. This T_c is smaller than that of bulk materials of $Ba(Pb_{0.75}Bi_{0.25})O_3$.

In BPO films, it was difficult to realize the epitaxial growth on MgO(001) substrate. Epitaxially grown BPO films were obtained when the thickness was less than 20 nm and T_s was around 700 °C. The content of Pb decrease with rising T_s, indicating that Pb atoms were easy to re-evaporate in BPO films. By increasing the amount of Pb in PLD targets, the re-evaporation of Pb atoms were compensated at some degree.

All BBO film fabricated on MgO substrate in this study demonstrated the epitaxial growth along [001] direction. In BBO films, Ba atoms were easy to re-evaporate, and the ratio of Bi atom enhanced as T_s increased. By using PLD targets which were rich in Ba atoms, the re-evaporation of Ba atoms were systematically compensated in BBO films.

BPO_{25} (~ 11 nm) and BBO_{75} (~ 33 nm) demonstrated epitaxial growth on MgO substrate along [001] direction. In BPO_{25}/sub, localization effect was observed by the analysis of temperature dependence of resistivity. On the other hand, BBO_{75} was considered to preserve charge order, because of highly insulating properties. These characterizations of BPO_{25}/sub and BBO_{75} are the preparation of chapter 5.

Chapter 5

Fabrication of $BaBiO_3/BaPbO_3$ Heterostructures with Single Interface

The atomically flat BBO/BPO interface might demonstrate charge transfer, resulting two-dimensional superconductivity. Since a charge order semiconductor BBO has much higher resistance than that of a semi-metal BPO, the difference of electrical resistance between BPO_m/sub and BBO_n/BPO_m/sub [*m* (*n*) unit cells of BPO (BBO)] approximately provides the resistance of BBO/BPO interface (sub: MgO(001) substrate).

In this chapter, BBO_{75} (33 nm)/BPO_{25} (11 nm)/sub with a bilayer structure was fabricated on MgO(001) substrate. In order to clarify the relationship between transport properties and the quality of interface, the fabrication of BPO_{25} (11 nm)/BBO_{75} (33 nm)/sub also were performed. The quality of BBO/BPO was suggested from the surface morphology on BBO_{75}/sub and BPO_{25}/sub.

5.1 Growth conditions for $BaBiO_3/BaPbO_3$ Heterostructure with Single Interface

From the discussion of chapter 4, the nominal composition of target materials were set to be Ba:Bi = 1.12:1 ($Ba_{1.12}BiO_{3+\delta}$) and Ba:Pb = 1:1.25 ($BaPb_{1.25}O_{3+\delta}$), in order to compensate the re-evaporation of Ba and Pb. During the deposition, the substrate temperature and oxygen pressure were kept at 650 ~ 675 °C and at 190 mTorr, respectively.

5.2 $BaBiO_3/BaPbO_3/MgO$

Figure 5-3 shows XRD pattern of BPO_{25} (11 nm)/sub and BBO_{75} (33 nm)/BPO_{25} (11 nm)/sub. In Fig. 5-3, the peaks except for the contribution of MgO in both of films were assigned with perovskite-type structure without impurities, indicating the realization of the epitaxial growth along [001]. In addition, 002 reflection peaks from BPO and BBO were clearly separated. The out-of-plane lattice constants of BBO and BPO in BPO_{25}/sub and BBO_{75}/BPO_{25}/sub were estimated to be 4.348 Å and 4.265 Å respectively. These values are almost the same length with the bulk values, implying that the epitaxial strain to BBO and BPO from MgO substrate is negligibly small.

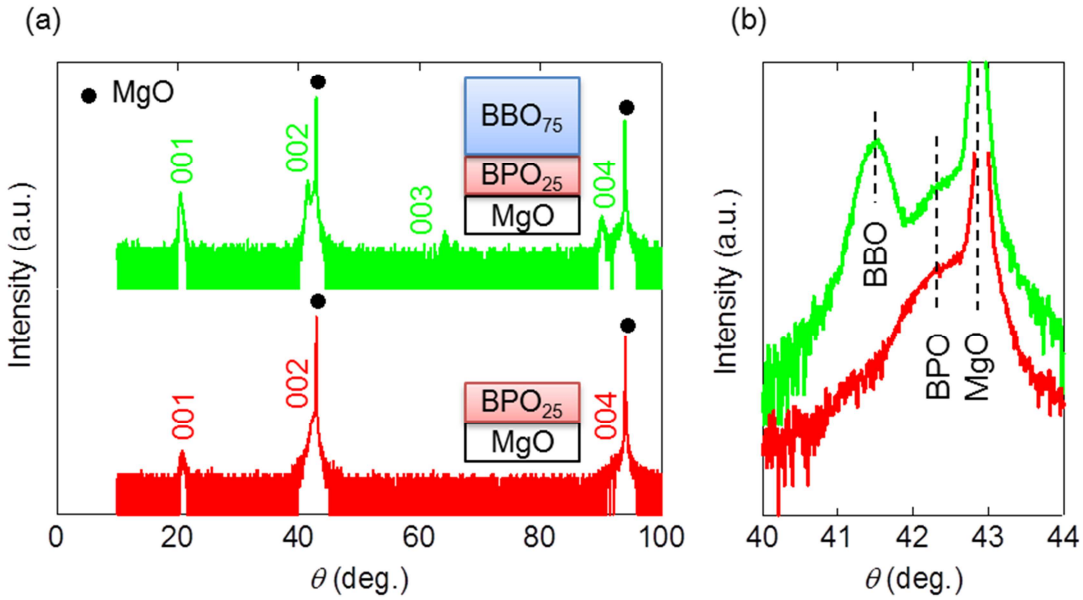

Fig. 5-1. XRD pattern of 2θ–θ scan for BBO_{75}/BPO_{25}/sub and BPO_{25}/sub. (a) Wide range of 2θ–θ scan. (b) Peaks from 002 reflection.

5.3 $BaPbO_3/BaBiO_3/MgO$

BBO/BPO interface was also realized in BPO_{25} (11 nm)/BBO_{75} (33 nm)/sub with a bilayer structure, where BPO was deposited on top of BBO film grown on MgO(001) substrate. In Fig. 5-2 (a), four peaks beside the reflection from MgO substrate are consistent with the epitaxial thin film of a [001] oriented perovskite-type compound without impurities. The peaks near 004 reflection of MgO are clearly separated as shown in Fig. 5-2 (b). The out-of-plane lattice constants are estimated to be 4.354 Å, and 4.258 Å, corresponding to that of BBO and BPO, respectively. These lattice constants are comparable to the values of bulk BBO and BPO, implying that the epitaxial strain from MgO substrate is negligibly small in BPO_{25}/BBO_{75}/sub, like in BPO_{25}/sub and BBO_{75}/sub.

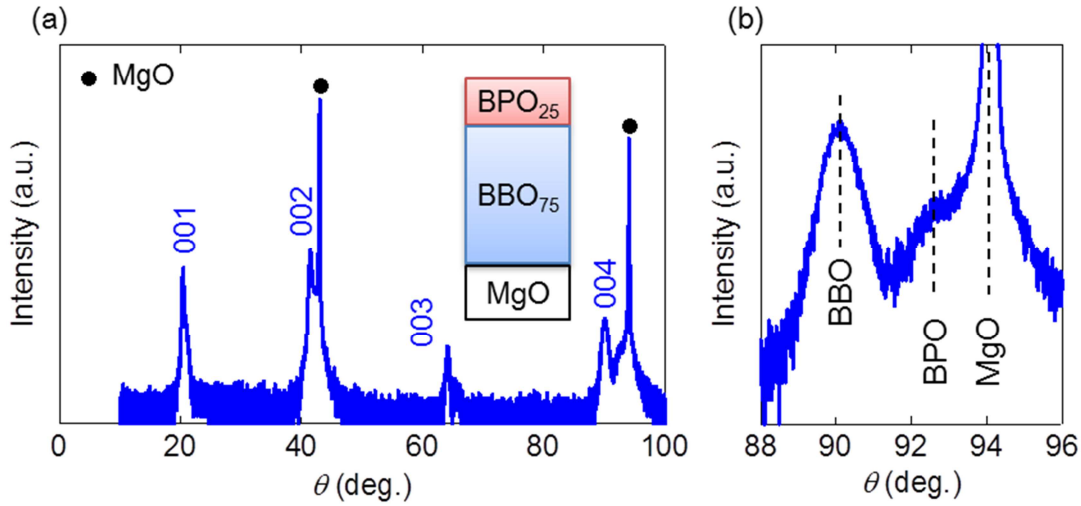

Fig. 5-2. XRD pattern of $2\theta-\theta$ scan in BBO_{75}/BPO_{25}/sub. (a) Wide range of $2\theta-\theta$ scan. (b) Peaks around 004 reflection

5.4 Quality of $BaBiO_3/BaPbO_3$ Interface

In order to realize superconducting interface by charge transfer, the higher quality of BBO/BPO interface is needed. The surface morphology of BBO_{75}/sub and BPO_{25}/sub is important for the demonstration of atomically flat BBO/BPO interface.

The difference of surface morphology was confirmed by RHEED image, which contains the information about the surface structure of material. Figure 5-3 (a) and (b) show the RHEED patterns of BBO_{75}/sub and BPO_{25}/sub, respectively. In BPO_{25}/sub dot-like pattern was observed, while BBO_{75}/sub showed streak pattern, implying that BBO_{75}/sub demonstrated a smoother surface.

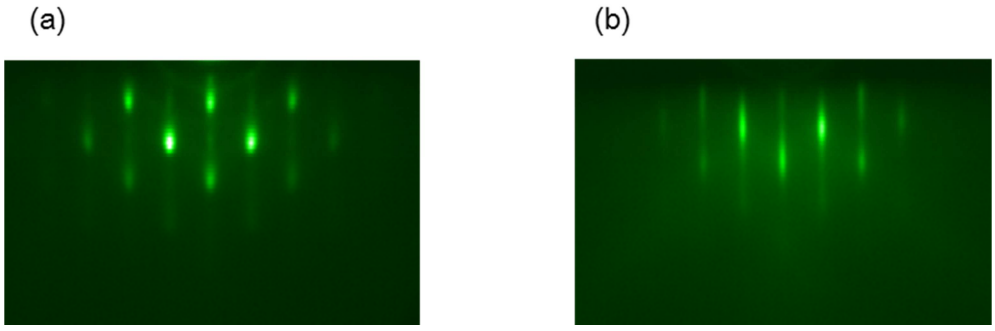

Fig. 5-3. RHEED patterns of (a) BPO_{25}/sub and (b) BBO_{75}/sub.

This trend about the surface roughness was also checked by AFM measurement. Figure 5-4 (a) and (b) shows the surface images of BBO_{75}/sub and BPO_{25}/sub observed by AFM observation. The roughness of root mean square (RMS) were estimated to be 0.97 nm on BPO_{25} (11 nm)/sub and 0.34 nm on BBO_{75} (33 nm)/sub. These RMS were obtained by the averaging values which were measured at five different places with the area of 5000 nm × 5000 nm. This indicates that the surface of BBO_{75}/sub was flatter than that of BPO_{25}/sub. Generally the fully relaxed film is difficult to realize flat surface, but it is surprising that RMS of 0.35 nm on BBO was less than one unit cell of BBO (~ 0.43 nm). Moreover, the surface of BBO_{75}/sub had the smaller domain structure than that of BPO_{25}/sub, as shown in Fig. 5-5. The maximum height difference (R_{max}) on the surface of BBO_{75}/sub and BPO_{25}/sub were estimated to be 3.6 nm and 11 nm in the region of 5000 nm × 5000 nm, respectively. These values of R_{max} support the

formation of larger domain on the surface of BPO_{25}/sub quantitatively. Therefore, BPO_{25}/BBO_{75}/sub has a possibility to realize higher quality of BBO/BPO interface, which is expected to be superconducting.

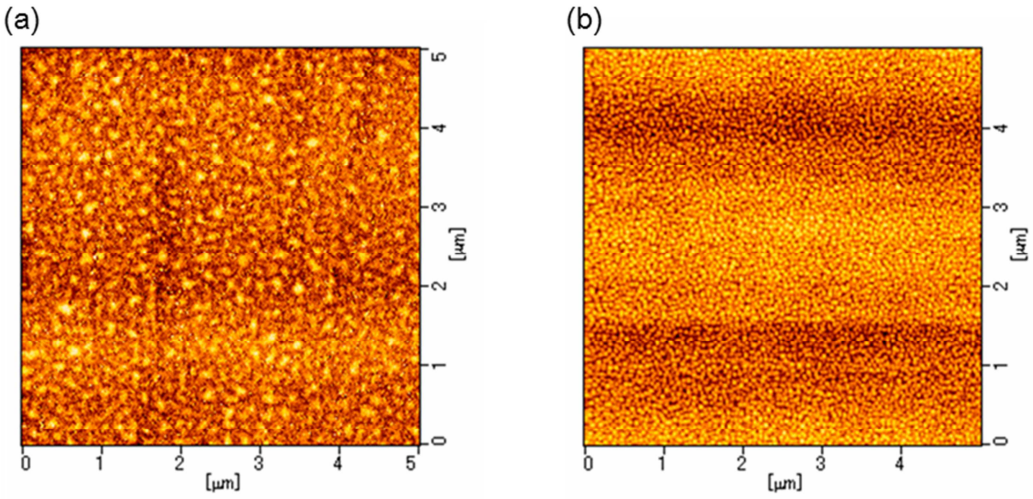

Fig. 5-4. Surface images obtained by AFM. (a) Surface of BPO_{25} (11 nm)/sub. (b) Surface of BBO_{75} (33 nm)/sub.

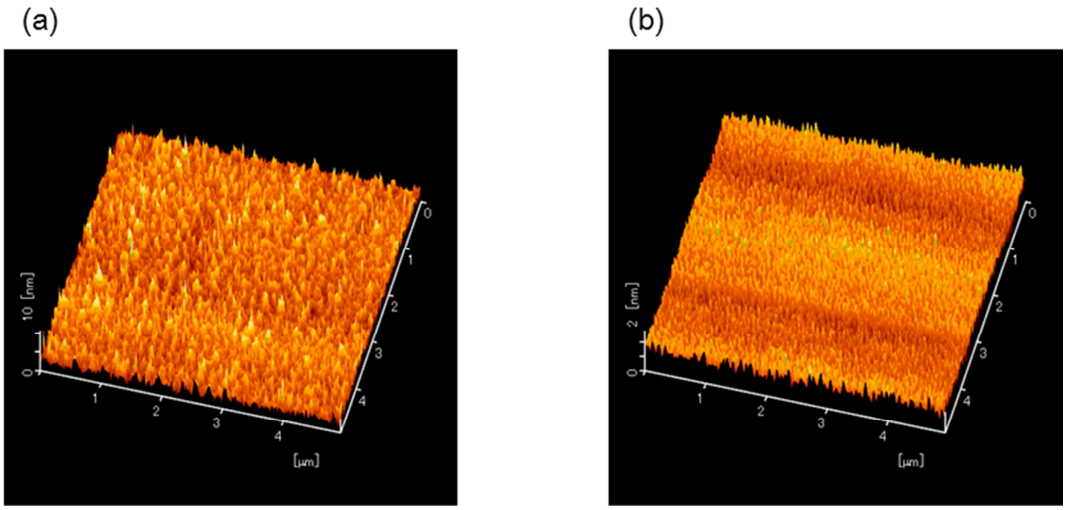

Fig. 5-5. Three-dimensional views of the surface structure. (a) Surface of BPO_{25} (11 nm)/sub. (b) Surface of BBO_{75} (33 nm)/sub.

5.5 Summary of This Chapter

In this chapter, BBO/BPO interface was fabricated in the films of BBO_{75}/BPO_{25}/sub and BPO_{25}/BBO_{75}/sub with a bilayer structure. From the analysis of XRD pattern, these films demonstrated a [001] oriented perovskite structure without impurities. The peaks in 2θ–θ scan of XRD were separated, implying the contribution from only BBO and BPO. Out-of-plane lattice parameters of BBO and BPO in BBO_{75}/BPO_{25}/sub and BPO_{25}/BBO_{75}/sub, which were close to that of bulk data, suggest the negligibly small effect of epitaxial strain, as summarized in Table 5-1.

In order to evaluate the quality of interface in these heterostructures indirectly, the surface roughness of BPO_{25}/sub and BBO_{75}/sub was focused. AFM measurement and RHEED image suggested the surface of BBO_{75}/sub was flatter than that of BPO_{25}/sub. This indicates that BPO_{25}/BBO_{75}/sub might realize the sharper BBO/BPO interface than BBO_{75}/BPO_{25}/sub.

	BPO	BBO
BPO_{25}/MgO	4.264 Å	-
BBO_{75}/MgO	-	4.338 Å
BBO_{75}/BPO_{25}/MgO	4.265 Å	4.348 Å
BPO_{25}/BBO_{75}/MgO	4.258 Å	4.354 Å
cf. Bulk [13]	4.26~ 4.27 Å	4.34~ 4.35 Å

Table 5-1. Out-of-plane lattice parameters of BPO and BBO in BPO_{25}/sub, BBO_{75}/sub, BBO_{75}/BPO_{25}/sub, and BPO_{25}/BBO_{75}/sub.

Chapter 6

Superconductivity at $BaBiO_3/BaPbO_3$ Interface

In this chapter, we evaluated transport properties of BBO_{75} (33 nm)/BPO_{25} (11 nm)/sub and BPO_{25} (11 nm)/BBO_{75} (33 nm)/sub, and discussed that BBO/BPO interface demonstrate superconductivity or not. The dimensionality of superconductivity is important to proof that a superconducting transition occur at BBO/BPO interface. If detailed characterization reveals two-dimensional nature of superconductivity, the interface is considered to realize a superconducting transition. Angular dependence of upper critical field depends on the dimensionality of superconductors. A Berenizinskii-Kosterlitz-Thouless transition which is characteristic for two-dimensional system can be checked on a current-voltage measurement and a temperature dependence of electrical resistance.

6.1 Superconducting transition in $BaPbO_3/BaBiO_3/MgO$

Figure 6-1 indicates the temperature dependence of electrical resistance (a) and Hall resistance (b) for BPO_{25}/sub and BBO_{75}/BPO_{25}/sub. The electrical resistance of BBO_{75}/BPO_{25}/sub was smaller than that of BPO_{25}/sub around room temperature in Fig. 6-1 (a), probably because of conducting BBO/BPO interface. The change in temperature dependence of electrical resistance from BBO_{75}/BPO_{25}/sub to BPO_{25}/sub implies semiconducting behavior of BBO/BPO interface. This semiconducting behavior might be originated from carrier-doped BBO due to the charge transfer across BBO/BPO interface. The absolute value of Hall resistance also decreased in BBO_{75}/BPO_{25}/sub, as shown in Fig. 6-1 (b). The amount of carriers is expected to be increased by introducing BBO/BPO interface. These behaviors of transport properties support the charge transfer at BBO/BPO interface. In spite of clear signature of charge transfer at BBO/BPO interface, superconductivity did not appear in BBO_{75}/BPO_{25}/sub.

The temperature dependence of electrical resistance in BPO_{25}/BBO_{75}/sub was quite weak and showed the zero-resistance indicative of a superconducting transition below T_c = 3.6

K (#1), as shown in Fig. 6-2. Considering that neither BPO_{25}/sub nor BBO_{75}/sub is a superconductor as described in the section of 4.4, superconductivity is realized at BBO/BPO interface. Figure 6-2 also indicates the temperature dependence of electrical resistance for a different sample of BPO_{25}/BBO_{75}/sub (#2). In #2, electrical resistance was almost similar to that in #1, and zero-resistance was observed below T_c = 2.5 K which is smaller than that in #1. This suggests that T_c depends on samples, and is considered to have the range from 2.5K to 3.6 K.

In Fig. 6-1 (a), the value of electrical resistance in BPO_{25}/BBO_{75}/sub is smaller than that in BBO_{75}/BPO_{25}/ sub. Temperature dependence in BPO_{25}/BBO_{75}/sub showed a less semiconducting behavior than that in BBO_{75}/BPO_{25}/sub. In the absolute value of Hall resistance, BPO_{25}/BBO_{75}/sub showed the lowest value as shown in Fig. 6-1 (b). This implies that the more carriers are accumulated on BBO/BPO interface in BPO_{25}/BBO_{75}/sub than BBO_{75}/BPO_{25}/sub. The differences in electrical resistance of Hall resistance imply that BPO_{25}/BBO_{75}/sub has the higher quality of BBO/BPO interface, enhancing the amount of the charge transfer. These differences between BBO_{75}/BPO_{25}/sub and BPO_{25}/BBO_{75}/sub might be related with the quality of BBO/BPO interface, inferred in the section of 5.4.

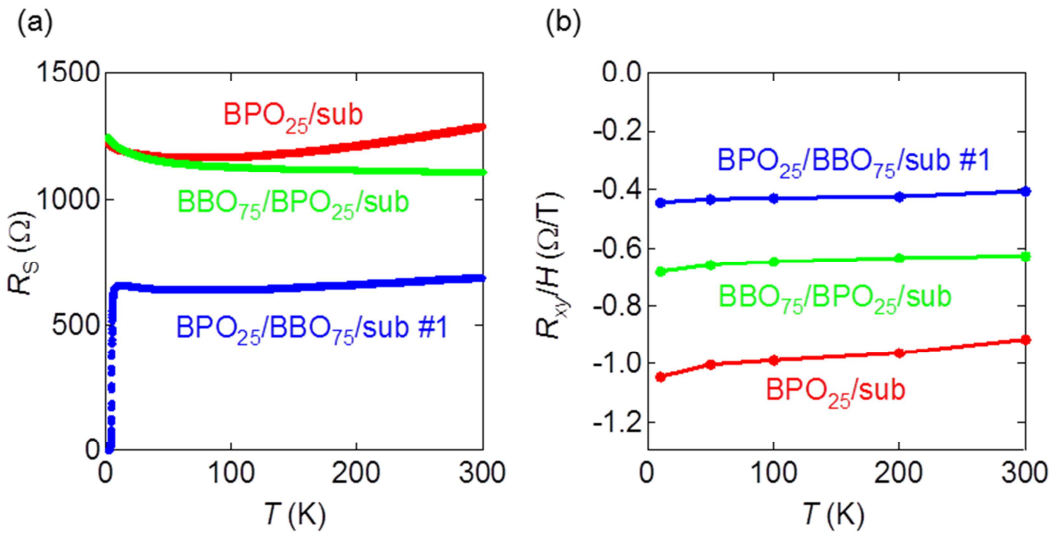

Fig. 6-1. Temperature dependence of transport properties for BBO_{75}/BPO_{25}/sub (green), BBO_{75}/BPO_{25}/sub (blue), and BPO_{25}/sub (red). (a) Electrical resistance. (b) Hall resistance.

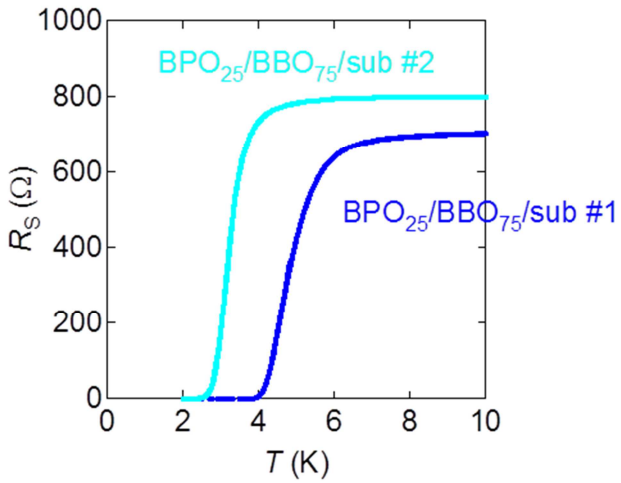

Fig. 6-2. Temperature dependence of electrical resistance of BBO_{75}/BPO_{25}/sub in the range from 10 K to 0 K. Zero resistance was observed below 3.6 K in #1 and 2.5 K in #2.

6.2 Dimensionality of Superconductivity in $BaPbO_3/BaBiO_3/MgO$

6.2.1 Criterions for Two-dimensional Superconductivity

Before the identification of dimensionality of superconductivity, it is introduced physical phenomena which are expected in two-dimensional system.

Tinkham Model

Superconductivity is destroyed by magnetic field. The magnetic field to break superconducting state perfectly is called as the upper critical field H_{c2}. The angular dependence of H_{c2} reflects the anisotropy of superconductivity, which is associated with the dimensionality of crystal structures or artificially fabricated structures not the symmetry of cooper pair. When superconductors have three-dimensional structure without anisotropy, H_{c2} from Ginzburg-Landau (GL) equation is given by

$$H_{c2} = \frac{\Phi_0}{2\pi\xi^2}, \qquad \text{(Eq.6-1)}$$

where, ξ is the superconducting coherence length and Φ_0 is the quantum flux.

Considering the anisotropy in three-dimensional superconductors, the anisotropic effective mass of electrons m is often introduced. m is known to be proportional to $1 / \xi$ within GL theory. In particular, two-dimensional system has the anisotropy about two directions, indicating that effective masses of electrons are described as m_{ab} in two-dimensional plane and m_c perpendicular to the plane. Taking into account for this kind of mass anisotropy into GL equation, $H_{c2,para}$,which is H_{c2} at magnetic field parallel to the plane, is expressed as

$$H_{c2,para} = \frac{\Phi_0}{2\pi\xi_{ab}\xi_c}. \qquad \text{(Eq.6-2)}$$

On the other hand, at magnetic field applied perpendicular to the plane, $H_{c2,per}$ is described as

$$H_{c2,per} = \frac{\Phi_0}{2\pi\xi_{ab}^2}. \qquad \text{(Eq.6-3)}$$

In quasi two-dimensional system, conduction carriers are confined in the plane, implying that m_c is heavier than m_{ab}. That is, ξ_c is smaller than ξ_{ab}. Thus we can observe the anisotropy of H_{c2} like $H_{c2,para} > H_{c2,per}$. The angular dependence of H_{c2} is shown in below equation.

$$\left(\frac{H_{c2}(\theta)\cos\theta}{H_{c2}^{per}}\right)^2 + \left(\frac{H_{c2}(\theta)\sin\theta}{H_{c2}^{para}}\right)^2 = 1 \qquad \text{(Eq.6-4)}$$

This model is called as the anisotropic GL model [82]. In this relationship, $\theta = 0$ means the magnetic field is applied in the plane.

The situation changes in the system with highly two-dimensional character like thin film superconductors. In particular, when the thickness of film d is shorter than ξ_c, the anisotropic GL model is not applicable to describe the angular dependence of H_{c2}. In superconductors confined in a very narrow region, the angular dependence of H_{c2} is discussed by M. Tinkham [83]. When GL equation is solved assuming that the locations of film edges are $\pm d / 2$ and the vector potential is used as $(0, -Hz, 0)$, the angular dependence of H_{c2} is given by

$$\left|\frac{H_{c2}(\theta)\cos\theta}{H_{c2}^{\mathrm{per}}}\right| + \left(\frac{H_{c2}(\theta)\sin\theta}{H_{c2}^{\mathrm{para}}}\right)^2 = 1. \quad \text{(Eq.6-5)}$$

This model is named by Tinkham model, yielding the estimation about the thickness of the superconducting layer d_{Tinkham} like

$$d_{\mathrm{Tinkham}} = \sqrt{\frac{6\Phi_0 H_{c2}^{\mathrm{per}}}{\pi (H_{c2}^{\mathrm{para}})^2}}. \quad \text{(Eq.6-6)}$$

The big difference of the anisotropic GL model and Tinkham model is the behavior around 0 degree. As fig. 6-3 indicates, Tinkham model has a cusp at 0 degree, while there is no cusp in the anisotropic GL model.

Using these two models, the dimensionality of some superconductors is classified experimentally. In a layered perovskite superconductor Sr_2RuO_4, the angular dependence of H_{c2} is described the anisotropic GL model (Fig. 6-4 (a)), indicating this compound is an anisotropic three-dimensional superconductor [84]. The example demonstrating Tinkham model is an artificially fabricated delta-doped structure of $SrTiO_3$ (Fig. 6-4 (b)) [85]. In this case, two-dimensional superconductivity is realized, and d_{Tinkham} agree with the thickness of Nb-doped layer. More interestingly, in a high-Tc superconductor $Bi_2Sr_2CaCu_2O_8$ which has two-dimensional crystal and electronic structure, the crossover from two-dimension to three-dimension is observed as a function temperature (Fig. 6-4 (c)) [86]. Due to the temperature dependence of ξ_c, the distance between superconducting CuO_2 block layers is longer than ξ_c below certain temperature, indicating superconducting layers can exist independently.

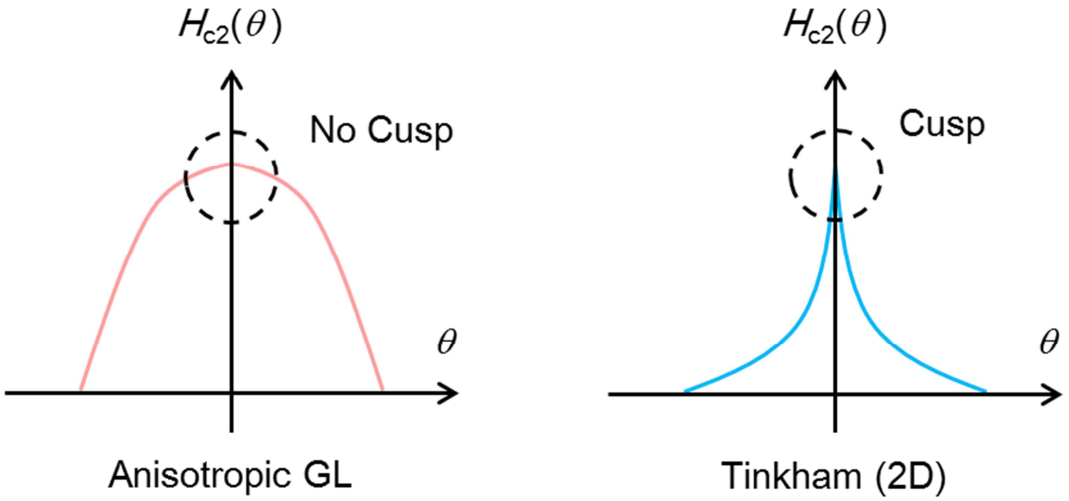

Fig. 6-3. Schematic picture of the anisotropic GL model (left) and Tinkham model (right).

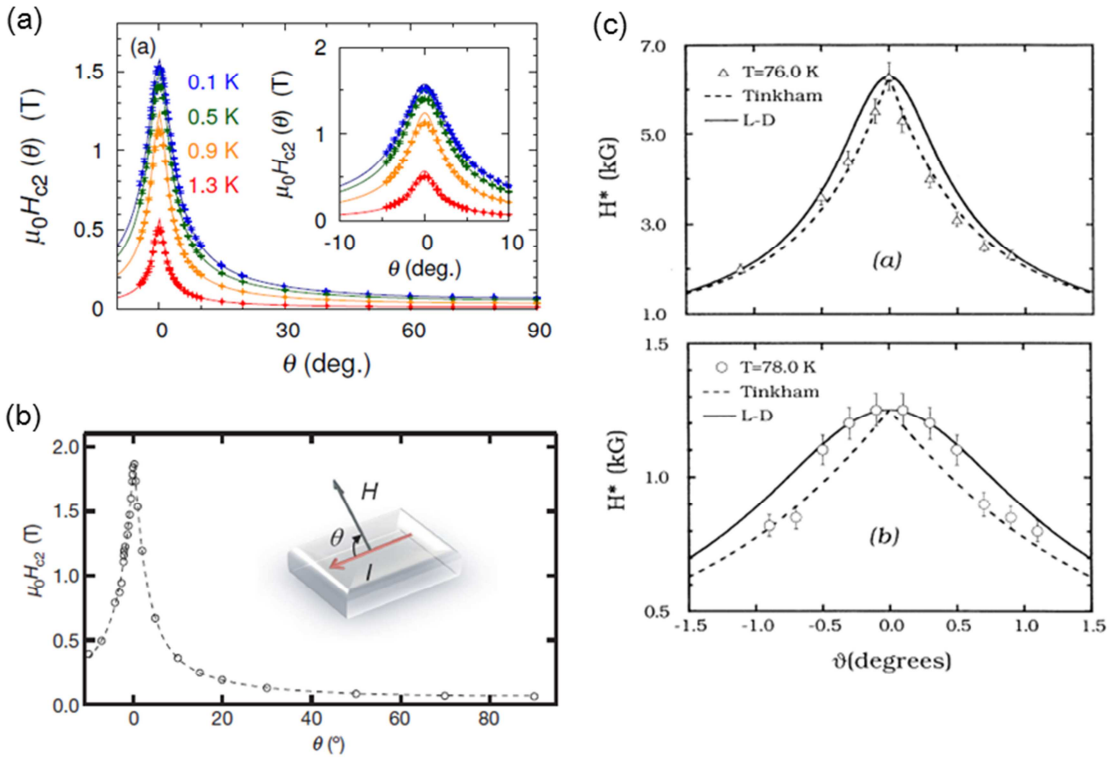

Fig. 6-4. Angular dependence of H_{c2} in some materials. (a) Sr_2RuO_4 [84]. (b) delta-doped structure of $SrTiO_3$ [85]. (c) $Bi_2Sr_2CaCu_2O_8$ [86].

Berenizinskii-Kosterlitz-Thouless Transition

In the low dimensional systems, the thermal fluctuations are strong. Such kind of strong fluctuation disturbs the occurrence of phase transitions. Mermin–Wagner theorem suggests that two-dimensional systems have no phase transition because the fluctuation prohibits the development of a long range order. However, in the two-dimensional system described by a *XY* model, a quasi-ordered phase without a long range order can be realized at low temperature. This phase transition is called as Berenizinskii-Kosterlitz-Thouless (BKT) transition [87-89]. First, superfluid helium film is found to undergo a BKT transition. After that, Beasley *et al.* reveals that this BKT framework can also apply to the thin film superconductors [90].

The fluctuation in the phase part of a wave function which describes the superconducting state generates vortex and antivortex. There is an attractive interaction between vortex and antivortex having logarithmic dependence to the distance between vortexes. Due to this attractive interaction, vortex and antivortex forms pairs at low temperatures. With increasing temperature, the thermal fluctuation starts to break vortex-antivortex pairs and generate freely moved vortexes at a BKT transition temperature (T_{BKT}). When the system has large fugacity, a high density of vortex-antivortex pairs is realized. In this condition, an ionic-like crystal of vortex-antivortex is predicted to be formed [91].

In two-dimensional superconductor, the transition into the superconducting state would also be a BKT transition, characterized by a transition temperature T_{KT}. The formation of the vortex-antivortex pairs realizes the zero-resistance state below T_{KT}. When freely moved vortexes are generated above T_{KT}, these vortexes induce non-ohmic conduction. Thus, the KT transition is supported by no-linearity in the current (I)-voltage (V) characteristics like $V \propto I^{\alpha(T)}$ with $\alpha(T_{BKT}) = 3$. Temperature dependence of electrical resistance is reflected by a BKT transition.

$$R(T) \propto R_0 \exp\left[-\frac{b}{(T - T_{BKT})^{1/2}}\right] \qquad \text{(Eq.6-7)}$$

where R_0 and b are a parameter depending on materials [88]. A BKT transition is observed experimentally in $LaAlO_3/SrTiO_3$ interface superconductivity. In this case, the good agreement of T_c and T_{BKT} is reported [60].

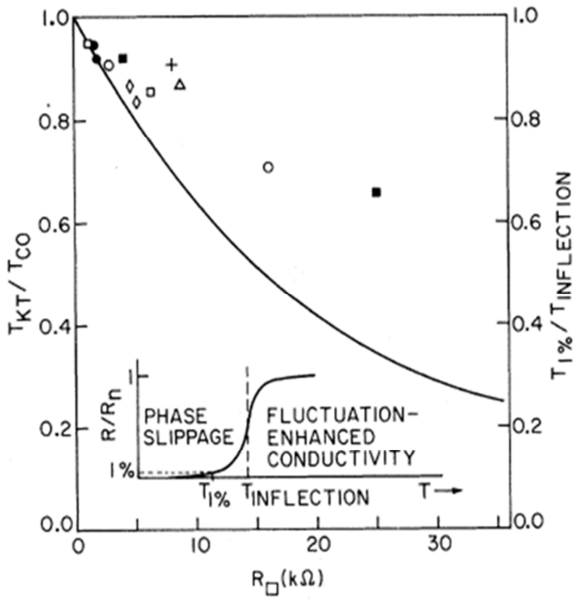

Fig. 6-5. Relationship between BKT transition temperature and electrical resistance [90].

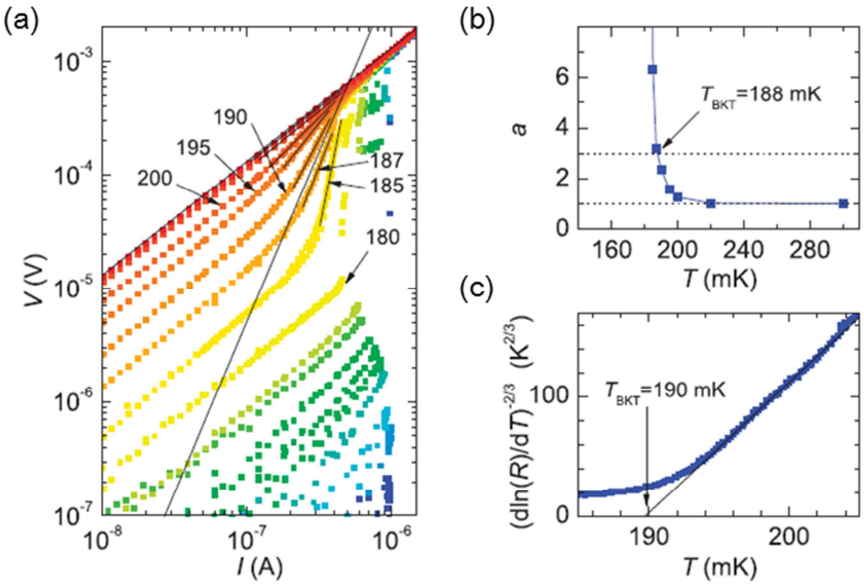

Fig. 6-6. BKT transition of $LaAlO_3/SrTiO_3$ interface superconductivity [60] (a) Current-voltage characteristics at several temperatures. (b) Temperature dependence of *a*. (c) Temperature dependence of $(d\ln(R)/d\,T)^{1/2}$.

6.2.2 Angular Dependence of Upper Critical Field of $BaPbO_3/BaBiO_3/MgO$

Two-dimensional character of the superconductivity revealed by detailed characterization supports that a superconducting transition occurs at an interface. As shown in Fig. 6-7 (a), the upper critical field H_{c2} of BPO_{25}/BBO_{75}/sub measured at 2.0 K showed a strong angular dependence, which is characteristic for superconductors confined in the narrow region. This measurement was performed in the sample of #1 in Fig 6-2. The penetration of quantum flux parallel to the plane is suppressed if the thickness of a superconductor decreases below a Ginzburg-Landau (GL) coherence length as explained in the section of 6.2.1. Thus, H_{c2} of superconducting films has a maximum value when the magnetic field is applied parallel to the film, and reduces monotonically with increasing the angle between the superconducting plane and the magnetic field. Moreover, Fig. 6-7 (b) shows a cusp in the angular dependence of H_{c2} around 0 degree which is the characteristic feature for two-dimensional superconductors, described by Tinkham model. In anisotropic three-dimensional superconductors, the angular dependence of H_{c2} does not have any cusp around 0 degree, explained by the effective-mass model based on GL theory. Our experimental data are reasonably fitted by Tinkham model better than effective-mass model (Fig. 6-7 and Fig. 6-8), proofing the two-dimensional superconductivity at BBO/BPO interface.

From Tinkham model, the thickness of superconducting layer d_{Tinhkham} and the superconducting coherence length in the plane ξ_{para} are estimated to be 8.3 nm (~ 19 unit cells) and 17 nm at 2.0 K, respectively. The ratio of $\xi_{\text{para}} / d_{\text{Tinhkham}}$ is ~ 2 at BBO/BPO interface, which is smaller than ~ 7 at $LaAlO_3/SrTiO_3$ interface superconductivity [67]. This difference in two-dimensionality between $LaAlO_3/SrTiO_3$ and BBO/BPO might be originated from the orbital characters that 6s orbital of Pb or Bi is less anisotropic than 3d orbital of Ti. The thickness of superconducting layer of 8.3 nm is reasonable to understand the existence or non-existence of superconductivity in BBO_{75}/BPO_{25}/sub and BPO_{25}/BBO_{75}/sub. From the discussion in the section of 5.4, the BBO/BPO interface in BBO_{75}/BPO_{25}/sub was expected to have irregularity ~ 11 nm at maximum, while BPO_{25}/BBO_{75}/ sub could show irregularity ~ 4 nm around

BPO/BBO interface. Thus, in only BBO_{75}/BPO_{25}/sub, superconductivity was considered to be be realized due to small roughness at interface.

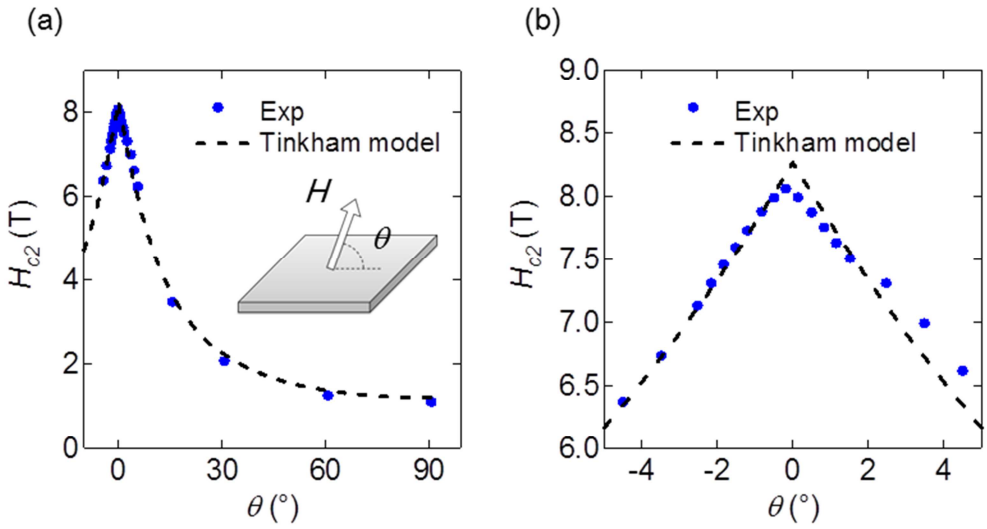

Fig. 6-7. Angular dependence of upper critical field in BPO_{25}/BBO_{75}/ sub at 2K. Broken line indicates Tinkham model. (a) Wide range of θ. (b) θ around 0 degree.

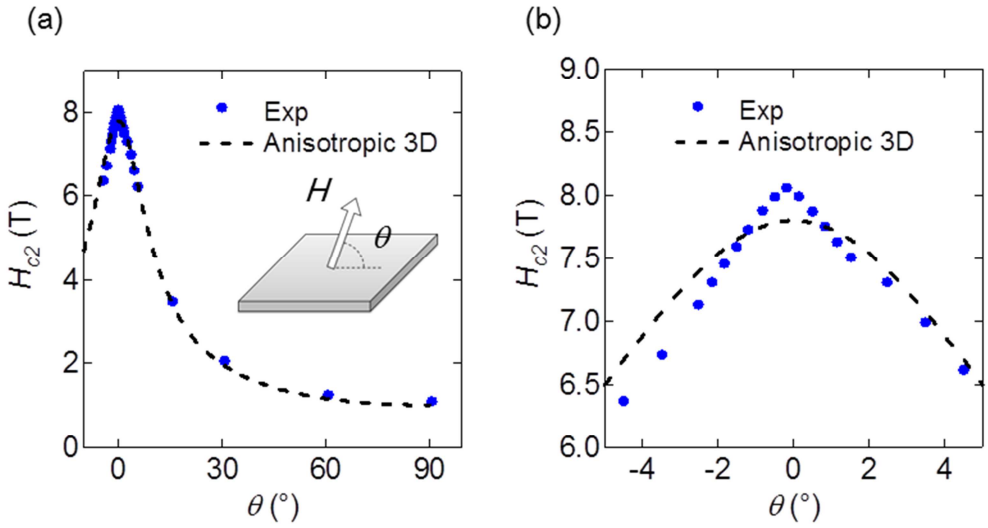

Fig. 6-8. Angular dependence of upper critical field in BPO_{25}/BBO_{75}/ sub at 2K. Broken line indicates the anisotropic mass model. (a) Wide range of θ. (b) θ around 0 degree.

6.2.3 Current-voltage Characteristics in $BaPbO_3/BaBiO_3/MgO$

In a two-dimensional system, the transition into the superconducting state is anticipated to be a Berenizinskii–Kosterlitz–Thouless (BKT) transition, where a transition temperature is defined as T_{BKT}. As mentioned in the introduction of this chapter, the intrinsic large fluctuations with a two-dimensional system generate vortexes and antivortexes, which form pairs below T_{BKT}. The BKT transition is supported by no-linearity in the current (I)-voltage (V) characteristics as V is proportional to I^a with $a(T_{BKT}) = 3$. We observed the no-linearity in the I-V measurement of BPO_{25}/BBO_{75}/sub, which can be explained by a BKT transition. This suggests that T_{BKT} is located between 2.6 K and 2.7 K in Fig. 6-7 (a). This measurement was done with the sample of #2 where zero resistance was realized below 2.5 K, as shown in Fig 6-2.

In addition at temperatures close to T_{BKT}, temperature dependence of electrical resistance is known to behave like $R_s = R_o \exp(-b/(T - T_{BKT})^{1/2})$, where R_o and b are material parameters. In Fig. 6-7 (b), electrical resistance of BPO_{25}/BBO_{75}/sub displayed this temperature dependence, meaning that a BKT transition expected to occur as in the I-V measurement, and T_{BKT} was estimated to be about 2.7 K These two analysis yield the almost same T_{BKT}, indicating that this two-dimensional superconductor undergoes a BKT transition at ~ 2.7 K. In BPO_{25}/BBO_{75}/sub, T_{BKT} is comparable with T_c in the temperature dependence of sheet resistance , as observed in $LaAlO_3/SrTiO_3$ interface superconductivity [60].

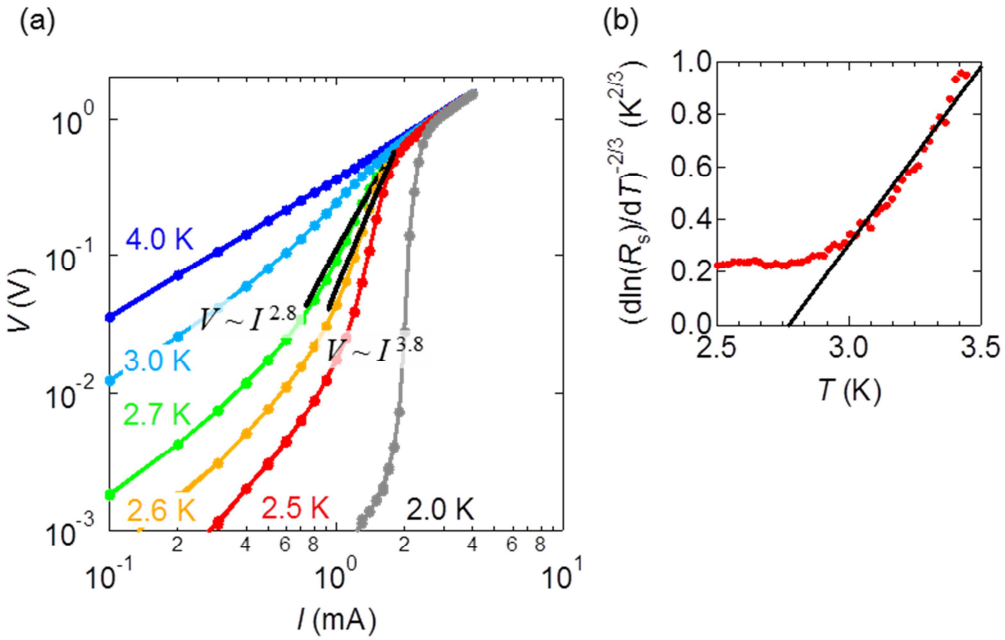

Fig. 6-9. (a) Current-voltage characteristics of BPO_{25}/BBO_{75}/MgO at several temperatures. (b) Temperature dependence of $(d \ln(R_s)/d T)^{-2/3}$ in BPO_{25}/BBO_{75}/MgO. The solid line is the fitting for a BKT transition with T_{BKT} = 2.7 K

6.3 Summary of This Chapter

First, the signature of charge transfer was observed by the comparison of transport properties between BBO_{75}/BPO_{25}/sub and BPO_{25}/sub. A superconducting transition with T_c = 2.5 K ~ 3.6 K was demonstrated in BPO_{25}/BBO_{75}/sub. The demonstration of superconductivity only in BPO_{25}/BBO_{75}/sub suggests that BPO_{25}/BBO_{75}/sub realized the higher quality of BBO/BPO interface than BBO_{75}/BPO_{25}/sub. This agrees with the prediction from the surface morphology of BBO_{75}/sub and BPO_{25}/sub in chapter 5.

Two dimensionality of superconductivity in BPO_{25}/BBO_{75}/sub was confirmed by an angular dependence of H_{c2} described by Tinkham model and a current-voltage characteristics indicating a BKT transition. This two-dimensional nature supports strongly that superconductivity was realized at BBO/BPO interface. Tinkham model suggested that the thickness of superconducting layer was estimated to be 8.3 nm (~ 19 unit cells).

Chapter 7

Characterization of Superconducting $BaBiO_3/BaPbO_3$ Interface

In the previous chapter, we found a superconducting transition in BPO/BBO/sub. This superconductivity seemed to occur at BBO/BPO interface, because detailed analysis provided the evidences of two-dimensionality.

In this chapter, we discussed the origin of superconductivity at BBO/BPO interface. There are two possibilities about the origin of this interface superconductivity. One is charge transfer at BBO/BPO interface without the inter-site mixing. The other is the formation of a solid-solution superconductor at BBO/BPO interface by cation interdiffusion. Thus, we would like to consider which a realistic scenario is by utilizing the experimental data. In order to clarify the atomic distribution near BBO/BPO interface, a STEM-EDS measurement was conducted. In a solid–solution BPBO superconductor with the thickness about 8.6 nm, transport properties were investigated. At last, we considered charge transfer quantitatively from the calculated transport properties at BBO/BPO interface.

7.1 Real Space Image of Cross-sectional $BaBiO_3/BaPbO_3$ Interface

Interface superconductivity is expected to occur only at atomically sharp interface. In order to clarify the atomic profile of BBO/BPO interface, STEM measurement was demonstrate on the cross-section of BPO_{25}/BBO_{75}/sub. The distribution of Ba, Pb, Bi, and O atoms near the cross-sectional BBO/BPO interface was also investigated by EDS analysis. Figure 7-1 shows a high-angle annular dark field (HAADF) image of BPO_{25}/BBO_{75}/sub which has a MgO capped layer . The capped layer played a role to protect the sample from the damage in the processing for the measurement. HAADF image show a clear boundary line between BBO and BPO. EDS mapping of Pb and Bi indicates that the cation interdiffusion is not likely to occur. The depth

dependence of counts suggests that the thickness of intermixing layer was seemed to be ~ 2 nm at most, as shown in Fig. 7-2. However, it is difficult to understand the depth dependence of counts, because the count of X-ray must be included from the neighbor atoms excited by scattered electron beam. This indicates that the area of cation interdiffusion could be less than 2 nm. Thus, in BPO_{25}/BBO_{75}/sub, the effect of inter-site mixing is consider to be negligibly weak, because the thickness of superconducting layer was calculated to be 8.3 nm (= $d_{Tinkham}$) in chapter 6.

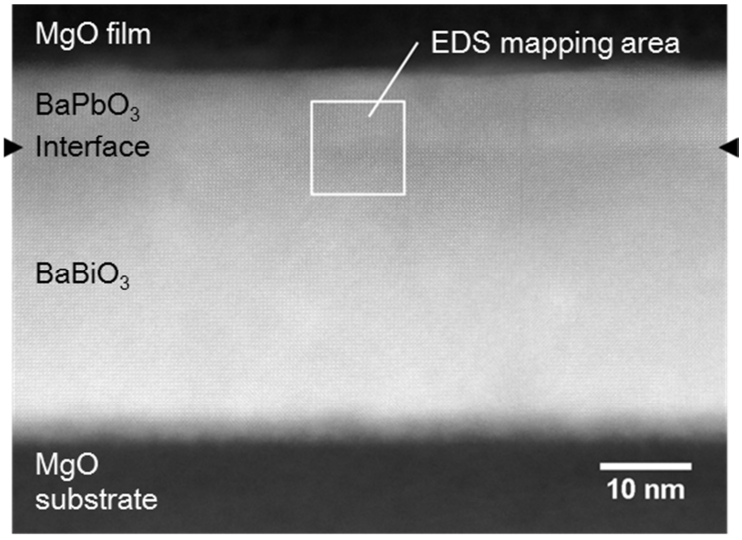

Fig. 7-1. HAADF image of cross sectional BBO/BPO interface in BPO_{25}/BBO_{75}/sub.

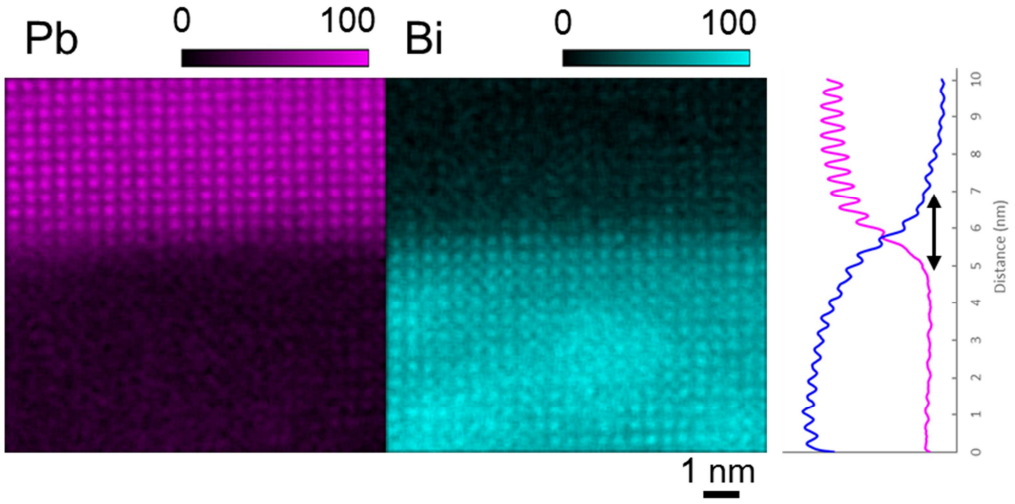

Fig. 7-2. EDS mapping of cross-sectional BBO/BPO interface. Purple dots and blue dots indicate Pb and Bi, respectively.

7.2 Electrical Resistance of $Ba(Pb_{1-x}Bi_x)O_3$ Film

In order to clarify the effect of inter-site mixing at BBO/BPO interface, transport properties was investigated on the thin film including the layer of solid-solution $Ba(Pb_{0.75}Bi_{0.25})O_3$ which has the highest T_c in bulk BPBO. Superconducting BBO/BPO interface was covered with a BPO layer which making the surface scattering weaker. Thus, BPO capped $Ba(Pb_{0.75}Bi_{0.25})O_3$ film is valid to evaluate the effect of cation interdiffusion at BBO/BPO interface. Figure 7-3 shows that in $BPO_{15}/BPBO_{20}$ (~ 8.6 nm) film, electrical resistance was higher than $h/(2e)^2$ (= 6.5 kΩ) which is a critical value of superconductor-insulator transition [92], and superconductivity did not appear. These behaviors suggest that disorder by solid solution induces the localization of conduction electrons. This localization effect which is often seen in two-dimensional systems, is considered to cause the high electrical resistance. Therefore, it is difficult to consider that the superconductivity at BBO/BPO interface originates from accidentally formed BPBO by inter-site mixing, because the angular dependence of H_{c2} yield a estimation of the thickness of superconducting layer to be 8.3 nm (= $d_{Tinkham}$).

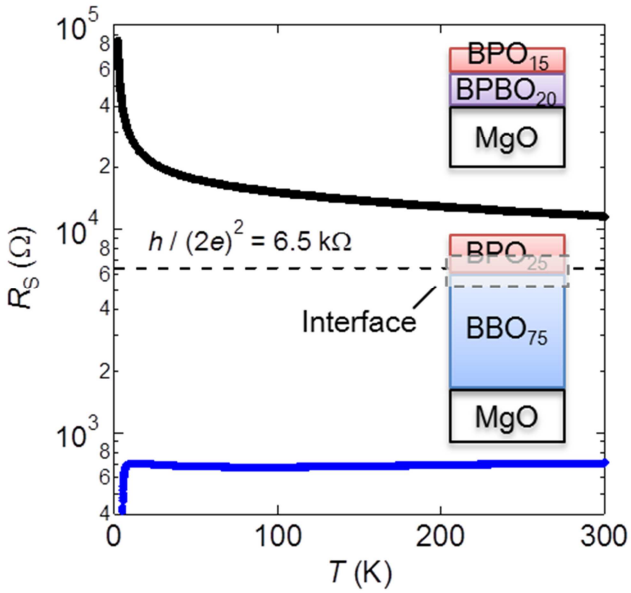

Fig. 7-3. Electrical resistance of a BPBO film capped by BPO. Black line is $BPO_{15}/BPBO_{20}$, and blue line is BPO_{25}/BBO_{75} superconductor. Broken line indicates $h/(2e)^2$ (= 6.5 kΩ) which is a critical value of superconductor-insulator transition.

7.3 Estimation of Transport Properties at $BaBiO_3/BaPbO_3$ Interface

In order to clarify the origin of two-dimensional superconductivity at BBO/BPO interface quantitatively, we performed the evaluation of transport properties at the interface. This evaluation was done by using the difference in transport properties between BPO_{25}/sub and BPO_{25}/BBO_{75}/sub. The absolute values of the electrical resistance and Hall resistance for BPO_{25}/BBO_{75}/sub were smaller than those of BPO_{25}/sub. BBO/BPO interface is considered to enhance electrical conduction, because BBO_{75}/sub is highly insulating. Thus, we assume that BPO_{25}/BBO_{75}/sub is composed of three parts, namely, a semi-metallic layer (BPO), a superconducting layer (BBO/BPO interface) and an insulating layer (BBO). Since only BPO and BBO/BPO interface contribute to the transport properties in this structure, the conduction carriers are supposed to exist in BPO and at BPO/BBO interface. Here, the interface part is assumed to be equally distributed on BPO and BBO, and the total thickness of BBO/BPO interface is fixed as d_{Tinkham} (= 8.3 nm), which was the thickness of a superconducting layer estimated from the angular dependence of H_{c2}. The resistivity and the carrier density of BBO/BPO interface were calculated by using the parallel resistance model and the two carrier model [93] (Fig. 7-4).

The carrier density at BPO/BBO interface is around 1.4×10^{21} cm^{-3} which is twice larger than that in BPO_{25} film, as shown in Fig. 7-5 (a). This indicates that charge accumulation occurs at BBO/BPO interface. The carrier density of 1.4×10^{21} cm^{-3} correspond to 1.2×10^{15} cm^{-2} as a sheet carrier density, indicating two electrons per unit cell.

In the assumption of uniform distribution, interface has 0.1 electrons. However this is different from ideal value of 0.5 electrons. In bulk BPBO, carrier density is not explained by the simple band picture in the region of large Bi content.At BBO/BPO interface, similar situation might occur.

In addition, Fig. 7-5 (b) shows the estimated resistivity of BPO/BBO interface is smaller than that of BPO_{25} film, supporting that carrier doping is realized at BBO/BPO interface. Even if the positon where the interface region distributes changes, the enhancement of carrier density and the reduction of resistivity are still confirmed at BBO/BPO interface. These

modulations of carrier density and resistivity at BBO/BPO interface are considered to induce two-dimensional superconductivity.

This quantitative estimation of transport properties at BBO/BPO interface is suggestive of charge transfer at the interface, because these behaviors of BBO/BPO interface are different from those of solid-solution BPBO in bulk. In solid-solution BPBO system, the resistivity is known to be lowest at $x = 0$ (BPO) and rises monotonically with increasing x (Bi content), while the carrier density as a function of x shows a maximum value at $x = 0.25$, corresponding to the highest T_c [13]. This x dependence of transport properties in BPBO solid solutions implies that the chemical substitution realizes the carrier-doping, accompanying the increase of resistivity due to the introduction of disorder. Therefore, the formation of solid-solution superconductor at the interface by inter-site mixing cannot explain the decrease of resistivity and the increase of carrier density at BBO/BPO interface, maintaining that BBO/BPO interface demonstrates two-dimensional superconductivity due to charge transfer.

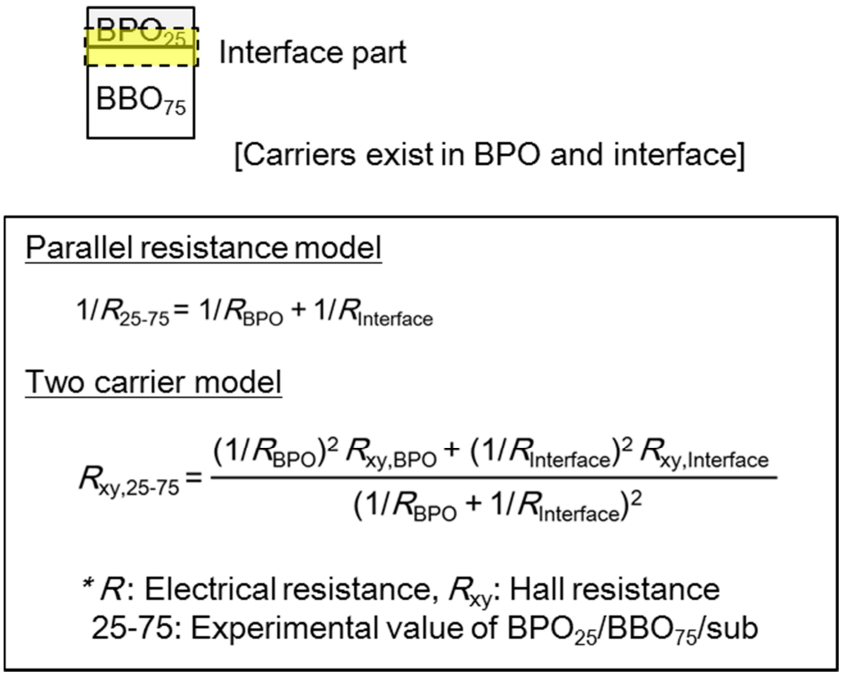

Fig. 7-4. Schematic figure of the analysis for transport properties of BBO/BPO interface (parallel resistance model and two carrier model).

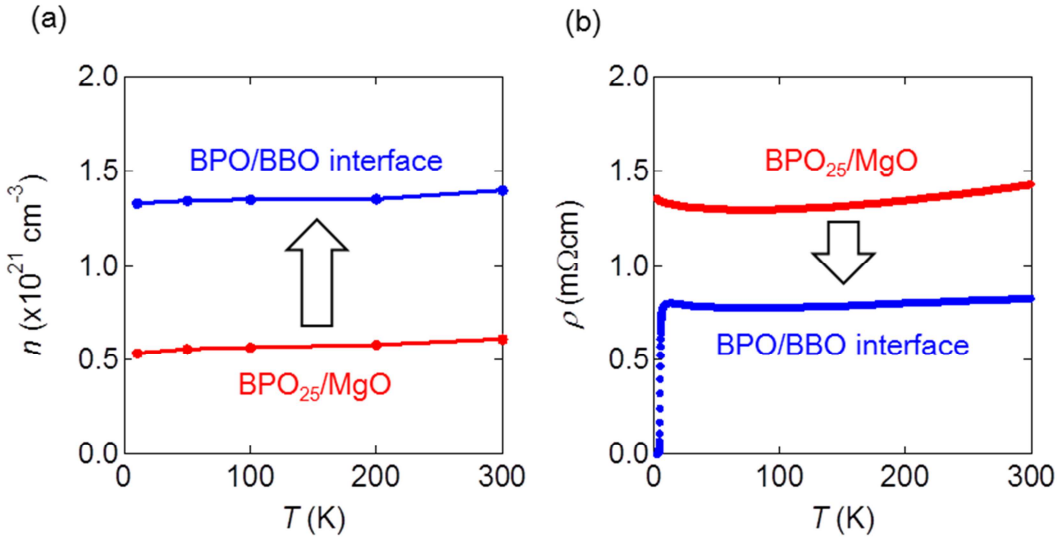

Fig. 7-5. Transport properties of BBO/BPO interface. (a) Temperature dependence of resistivity. (b) Temperature dependence of resistivity. Blue line shows BBO/BPO interface, and red line indicates BPO_{25}/sub.

7.4 Summary of This Chapter

STEM-EDS analysis of a cross-sectional BBO/BPO interface revealed that the cation interdiffusion was not likely to occur. In a solid-solution BPBO film, superconductivity disappeared due to disorder of solid-solution, when the film thickness was 8.6 nm (~ 20 unit cells). These observation of STEM-EDS and transport properties of BPBO film suggest that a superconducting transition at BBO/BPO interface is not originate from inter-site mixing near the interface, by considering that the thickness of superconducting layer was estimated to be 8.3 nm from angular dependence of H_{c2}.

In the estimated transport properties at BBO/BPO interface, charge accumulation at the interface was confirmed quantitatively. Moreover, decrease of resistivity and enhancement of carrier density at BBO/BPO interface was not explained by solid solutions. This also implies that this two-dimensional superconductivity was originated from charge transfer at BBO/BPO interface.

Chapter 8

Enhancement of Superconducting T_c in $BaBiO_3/BaPbO_3$ Superlattices

In chapter 6 and 7, BBO/BPO interface was found to show two-dimensional superconductivity due to the charge transfer. The superconducting transition temperature T_c of BBO/BPO interface did not exceed the maximum value of bulk BPBO systems. A reason about this lower T_c is considered to be the fluctuation of two-dimensional system. The carrier density induced by the charge transfer across interface might be not enough high to surpass T_c of bulk BPBO. In this chapter, we discuss the enhancement of T_c by utilizing BBO/BPO superlattice structure which intends the recovery of three-dimensionality and the enhancement of the carrier density due to the overlap of interface states.

8.1 Fabrication of $BaBiO_3/BaPbO_3$ Superlattices

From the discussion of chapter 4, the nominal compositions of target materials were selected to be Ba:Bi = 1.15:1 ($Ba_{1.15}BiO_{3+\delta}$) for BBO and Ba:Pb = 1:1.20 ($BaPb_{1.20}O_{3+\delta}$)for BPO, in order to compensate the re-evaporation of Ba and Pb. During the deposition, the substrate temperature and oxygen pressure were kept at 650 °C and at 190 mTorr, respectively. In the fabrication of $BaBiO_3/BaPbO_3$ superlattices, BBO was deposited on MgO substrate at first, because BBO was found to have the flatter surface than BPO from chapter 5. While the total thickness of superlattices was fixed to be around 50 nm, the period of superlattice was changed as a function of *m*, which means the number of BBO layers in a single supercell. In the synthesis of superlattices, the depositions of BBO and BBO were performed alternatively by controlling the number of laser pulses. The chemical composition of superlattices was set to be $Ba(Pb_{0.75}Bi_{0.25})O_3$ which shows the highest T_c in solid-solution BPBO system. Figure 8-1 indicates the schematic picture of synthesized BBO_mBPO_{3m} superlattices.

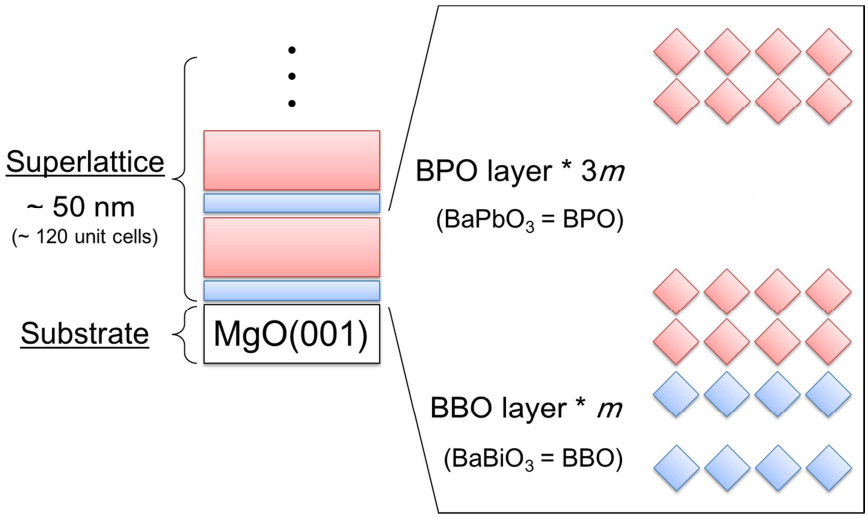

Fig. 8-1. Schematic picture of the fabricated BBO_mBPO_{3m} superlattice.

Figure 8-2 (a) indicates 2θ-θ scan of XRD pattern for fabricated BBO_mBPO_{3m} superlattices (m = 2 ~ 7). Epitaxial growth along [001] direction was confirmed at m = 2 ~ 7. From the peaks of 002 reflection, the lattice constants along c-axis are calculated to be 4.283 Å, which is the almost same value as bulk $Ba(Pb_{0.75}Bi_{0.25})O_3$. This lattice constant is considered to be close to the average value of three BPO unit cells and a BBO unit cell, indicating that each BBO and BPO layers in superlattice were not affected by the strain from MgO substrate.

The superlattice peaks were observed in 2θ–θ scan of XRD pattern, and these peaks were never seen in the bulk BPBO films as shown in Fig. 8-2 (b). Figure 8-3 indicates that the superlattice periods which were estimated from the positon of superlattice peaks are similar to $4m$ which is the ideal value of the period. SEM-EDS measurement revealed that the chemical composition of all superlattices was found to be Pb:Bi = 3:1, which is consistent with the composition of BBO_mBPO_{3m} superlattices. The content of Ba was almost the same as that of the summation of Pb and Bi. The content of O atom was not considered, because MgO substrate contributed to the spectrums of EDS and it was difficult to estimate the amount of O in BBO_mBPO_{3m} superlattices. The periods and chemical composition of superlattice indicated these BBO_mBPO_{3m} superlattices were synthesized as intended. These fabrications are a little bit surprising, because Bi is next to Pb in the periodic table, implying that the modulation of electron density between BBO and BPO is essentially small.

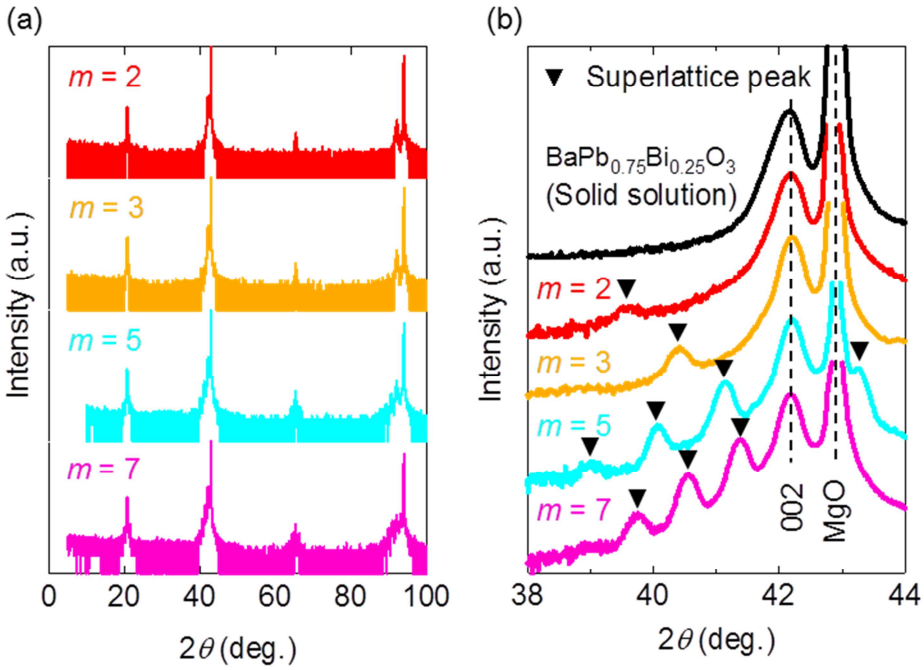

Fig. 8-2. 2θ–θ scan of XRD pattern of BBO_mBPO_{3m} superlattices. (a) Wide range scan. Epitaxial growth is checked. (b) Peaks around 002 reflection.

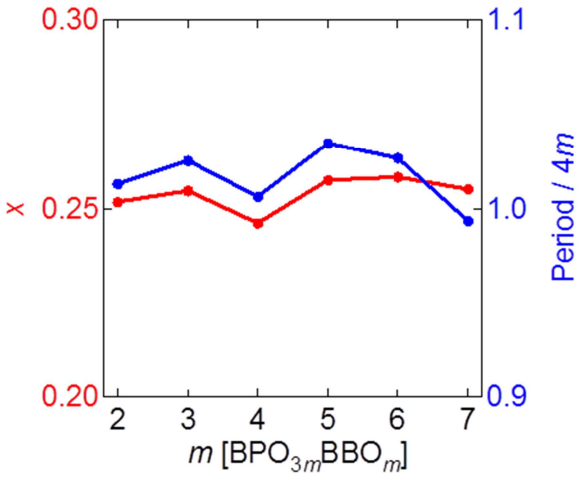

Fig. 8-3. Red line and value mean the ratio of Bi in the total amount of Bi and Pb. x = 0.25 is an ideal value. Blue line and value indicate the superlattice period divided by 4*m*. The superlattice periods are calculated by the position of superlattices peaks. If "Period/4*m*" is 1, the superlattice is fabricated as designed.

8.2 Superconducting Properties of $BaBiO_3/BaPbO_3$ Superlattices

In order to investigate the superconducting properties of BBO_mBPO_{3m} superlattices, the resistivity of BBO_mBPO_{3m} superlattices were measured. Figure 8-4 (a) shows the temperature dependence of the resistivity of BBO_mBPO_{3m} superlattices and a $Ba(Pb_{0.75}Bi_{0.25})O_3$ film. Compared with a $Ba(Pb_{0.75}Bi_{0.25})O_3$ film, the value of resistivity clearly decreased in BBO_mBPO_{3m} superlattices. That is, the introduction of superlattice structures removed disorder from solid solutions, indicating that the mean free path of conduction electrons become longer.

All the superlattices show superconductivity, as shown in Fig. 8-4 (b). Zero-resistance was realized at m = 2, 3, but the resistivity did not goes down to the zero at m > 4. Here, T_c is defined as a temperature of onset for a superconducting transition. m dependence of T_c in Fig. 8-5 indicates the systematic behavior as follows. At $m \geq 5$, T_c seems to be saturated around 4 K, and T_c increases monotonically to 6.9 K with decreasing m from 5 to 2. The constant value of T_c at large m suggests that the superconducting properties are dominated by the BBO/BPO interface. In the case of $m \geq 5$, the distance between BBO/BPO interfaces is enough large for interface itself to behave independently. On the other hand, below m = 4, the interface region start to overlap, resulting the enhancement of T_c. That is considered to be originated from the recovery of three-dimensionality and the increase of the net carrier density due to the overlap of interface. More interestingly, at m = 5, one supercell is composed by 20 unit cells of BBO and BPO. The length of 20 unit cells is comparable to the $d_{Tinkham}$ ~ 19 unit cells which is the thickness of superconducting layer at BBO/BPO interface, estimated from the angular dependence of H_{c2} in chapter 6. Therefore, m = 5 is considered to be valid for the boundary that interface state overlap or not.

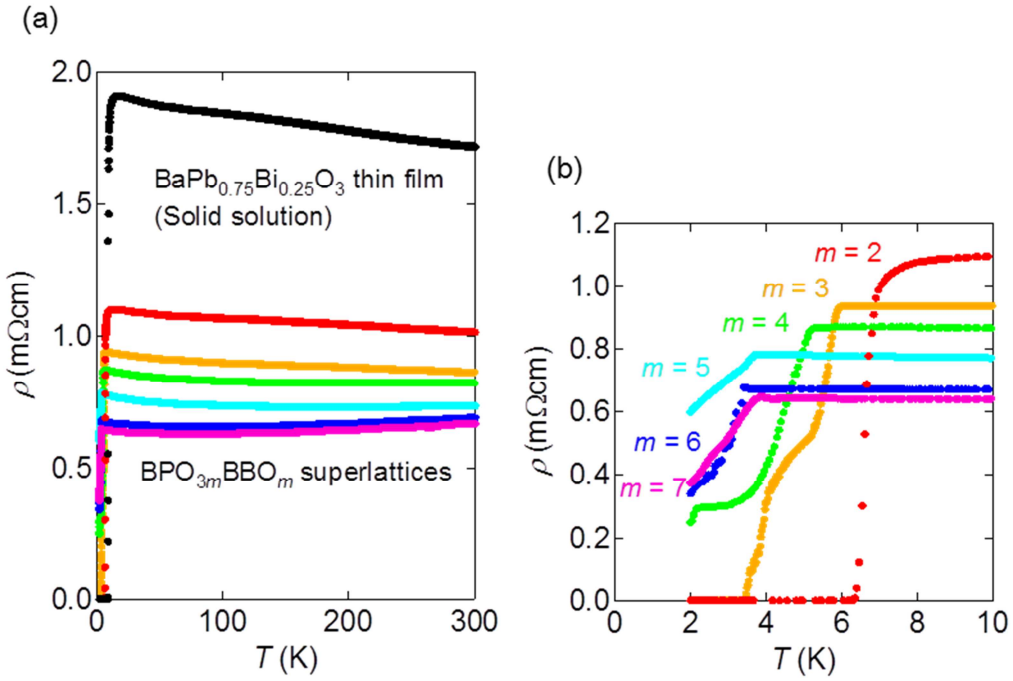

Fig. 8-4. (a) Resistivity of BBO_mBPO_{3m} superlattices and $Ba(Pb_{0.75}Bi_{0.25})O_3$. The measurements were done from 300 K to 2 K. (b) Resistivity of BBO_mBPO_{3m} superlattices at low temperatures

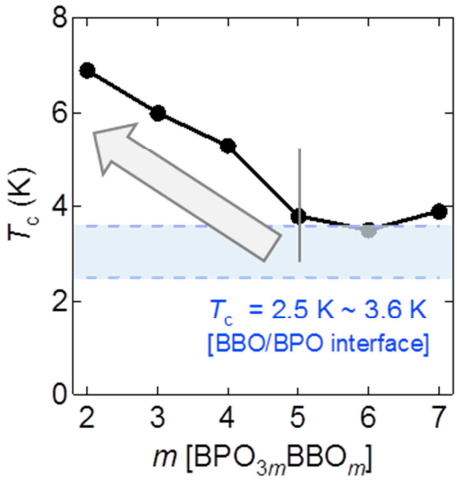

Fig. 8-5. m dependence of T_c in BBO_mBPO_{3m} superlattices. Blue area indicates the range of T_c at single BBO/BPO interface.

8.3 Summary of This Chapter

We aimed at increasing the superconducting transition temperature T_c in BBO/BPO superlattice structure since BBO/BPO interface was found to show two-dimensional superconductivity in chapter 6. The advantages to introduce superlattice structure are considered to be the recovery of three-dimensionality and the enhancement of the net carrier density.

The fabrications of BBO_mBPO_{3m} superlattices (m = 2 ~ 7) were confirmed by XRD and SEM-EDS measurements. All BBO_mBPO_{3m} superlattices show superconductivity. At $m \geq 5$, T_c was saturated, indicating that the superconducting properties were dominated by BBO/BPO interface. With decreasing m from 5, T_c tends to increase, implying that three-dimensionality is recovered and the net carrier density is enhanced due to the overlap of interface state. Interestingly, m = 5 corresponds to 20 unit cell whose length is about d_{Tihnkham} ~ 8.3 nm, which is the thickness of superconducting BBO/BPO interface, estimated from the angular dependence of H_{c2}. This critical length ~ 20 unit cell is consistent with the explanation that the interface states overlap or not.

Chapter 9

Conclusion

9.1 Realization of Two-dimensional Superconductivity at $BaBiO_3/BaPbO_3$ Interface

BBO/BPO interface was found to undergo a superconducting transition below 3.6 K. The angular dependence of the upper critical field H_{c2} was fitted well by Tinkham model, indicating this superconductor has two-dimensional character. BKT transition was also confirmed in the current-voltage characteristics, supporting that BBO/BPO interface displays two-dimensional superconductivity.

Form the observation of RHEED and AFM, a superconducting BBO/BPO interface is expected to be atomically flat. STEM-EDS mapping of a cross-sectional interface also suggests that BBO/BPO interface is found to have smoothness at atomic-scale in a real-space image.

The solid-solution BPBO film did not show superconductivity with the thickness of d_{Tinkham}, which is the thickness of superconducting layer estimated from the angular dependence of H_{c2}. In the quantitative estimation of transport properties of BBO/BPO interface, resistivity of BBO/BPO interface was smaller than that of BPO film, and the carrier density of BBO/BPO interface enhance. These behaviors imply the realization of charge transfer, and indicate that the cation interdiffusion was not likely to occur at BBO/BPO interface.

The enhancement of T_c is expected by creating heterointerfaces due to the removal of disorder which is generally considered to reduce T_c. Indeed, the recent study suggests that T_c increase if disorder is removed in solid-solution BPBO. However, T_c = 3.6 K and $n = 1.4 \times 10^{21}$ cm^{-3} at BBO/BPO interface is comparable to $T_c \sim 4$ K and $n \sim 2 \times 10^{21}$ cm^{-3} of bulk BPBO superconductor [34], indicating that the fluctuation with two-dimensional system might compensate the effect of eliminated disorder.

The realization of superconductivity in a disorder-removed BBO/BPO system is important to develop superconducting properties of BBO/BPO heterostructure. The fabrication

of BBO/BPO superlattices, which is removed the disorder from BPBO solid solutions, might enhance a superconducting transition temperature, because the overlap of the interface region recover three-dimensionality and increase carrier density.

9.2 Enhancement of Superconducting T_c in $BaBiO_3/BaPbO_3$ Superlattices

Based on the realization of superconductivity at a single BBO/BPO interface, we aim at increasing T_c in the system with multiple BBO/BPO interface. BBO_mBPO_{3m} superlattices (m = 2 ~ 7) were fabricated on MgO substrate. The analysis of XRD and SEM-EDS showed that the period and the composition of superlattices were as intended. All BBO_mBPO_{3m} superlattices (m = 2 ~ 7) showed superconductivity. T_c was saturated at $m \geq 5$, while the enhancement of T_c was realized with reducing from m = 5. This m dependence of T_c is explained by the control of distance between interfaces. The constant T_c at $m \geq 5$ suggests that the superconducting properties were dominated by BBO/BPO interface, since the distance between interfaces is long enough to behave independently. On the other hand, the increase of T_c below m =5 indicates that the overlap of conductive BBO/BPO interface state recover three-dimensionality and increase the carrier density in the area between interfaces.

Modulation of T_c by introducing the superlattice structure is significant to develop superconducting properties in oxide heterostructures. Previously, the dimensionality of superconductor was controlled by changing the thickness of films [84], but T_c has never modulated. This study reveals that the distance of interface could be a parameter to determine T_c, opening the door to develop superconductor by utilizing oxide heterostructures

9.3 Possibility to Exceed Superconducting T_c of Solid-solution BPBO by Eliminating Disorder

The BBO/BPO interface superconductivity was realized by charge transfer across the interface, and BBO_mBPO_{3m} superlattices also showed superconductivity. T_c of BBO/BPO superlattice increased from that of a single BBO/BPO interface with reducing the distance between interfaces, implying the overlap of interface state recover three-dimensionality and enhance carrier density. However, T_c does not exceed bulk maximum value of 12 K in $Ba(Pb_{0.75}Bi_{0.25})O_3$.

Removal of disorder is confirmed by the reduction of resistivity in superlattices, suggesting that disorder might not be responsible for lower T_c of BPBO than that of BKBO. Crystal symmetry is considered to be significant for the superconducting properties in bulk BPBO. Recently, the relationship between polymorphism and superconductivity in $Ba(Pb_{1-x}Bi_x)O_3$ has been discussed. This polymorphism means the coexistence of tetragonal phase and orthorhombic phase in superconducting BPBO. Tetragonal phase is reported to be origin of superconductivity. By comparison with BKBO, the tilting distortion of BiO_6 octahedrons is suggested to demonstrate higher T_c of BKBO than that of BPBO. In BBO/BPO heterostructures, the crystal structures of BBO and BPO are considered to take a cubic symmetry without the tilting distortion. Thus, T_c of BBO/BPO superlattice might exceed that of bulk BPBO superconductors if disorder is removed to keep the crystal symmetry of bulk BPBO. In thin films, epitaxial strain can be controlled by crystal distortions. Therefore, BBO/BPO heterostructures have chances to realize high T_c by further investigation about the crystal growth of BBO and BPO.

9.4 Perspective in $BaBiO_3$ Heterostructures and Other Oxides

This study demonstrated charge transfer and superconductivity in BBO/BPO heterostructures which are epitaxially grown along [001] direction on MgO substrate. The control of crystal growth orientation is considered to enhance superconducting properties. In BBO, the layers of Bi^{3+} and Bi^{5+} are stacked alternatively along [111] direction. If the thickness of BBO becomes thinner and the number of BBO layers is even, charge order state can be modulated spontaneously. For example, let's consider three layers of BBO along [111] direction, implying that the layers of Bi^{3+} , Bi^{5+}, and Bi^{3+} are stacked, In this case, the average valence of Bi atoms is calculated to be 3.7 + [= (3 + 5+ 3)/3], which is not consistent with 4+ from ionic limit. This disagreement of valence state indicates the possibility to destroy charge disproportionation in BBO, resulting superconductivity. This breaking of charge order does not accompany the introduction of disorder. Therefore, [111] orientation of BBO film has a potential to realize high T_c.

Electrostatic doping on BBO is also interesting to increase superconducting properties. In BBO/BPO heteroniterface, the accumulated charges at room temperature correspond to ~ 1.4 $\times 10^{15}$ cm^{-2} as a sheet carrier density. This carrier density is comparable to expected value in EDLT doping, but the thickness of charge distributed area is different between BBO/BPO interface and EDL. While the thickness of BBO/BPO interface is estimated to be 8.3 nm, that of EDL is expected to be a few nanometer, indicating the three-dimensional carrier density can be higher by using EDLT structure.

Moreover, the creation of heterojunction between BBO and other oxides different from BPO can be a platform to demonstrate higher T_c. The amount of accumulated carrier at the interface is considered to be a key to define superconducting properties. The carrier density at the interface is determined by the difference of chemical potential of materials which are constituents of heterointerface. Therefore, by the combination of materials with a large difference in chemical potential, there are chances to realize high T_c. by constructing heterostructures.

Acknowledgment

First of all, I would like to express the deepest gratitude to Prof. H. Takagi. He gave me the opportunity to challenge the thin film project, and my research has been accelerated by his constrictive comments. I have been encouraged very much by his attitude toward science and insight to grasp the essence. He also allowed me to receive the training of thin film research from Dr. J. Matsuno at RIKEN in the first year of my doctoral course. Due to this training, I learned about the growth and characterization of thin films, which were the most important basis for my Ph. D. thesis.

Second, I am sincerely grateful to Dr. J. Matsuno and Dr. D. Hirai. During my Ph. D. course, they supported my study in all the aspects; experimental techniques, extensive discussions about the results, how to give a presentation and write papers in journals. I could not complete my doctor thesis without their help.

This work was performed by the kind support from scientists in the University of Tokyo and Max-Plank institute. I thank for Prof. Y. Ikuhara, Prof. N. Shibata, Dr. A. Kumamoto, and Ms. N. Saito about STEM-EDS measurement and discussion about the results. I appreciate Dr. T. Takayama for assisting *I-V* measurement.

Thanks to many members of Takagi laboratory, I really enjoyed my research life of doctoral program for three years. First, I acknowledge staff members Dr. Y. Nakamura, Prof. K. Taniguchi, Dr. W. Andreas, Dr. Y. Katsura, and Dr. G. Alexdra for useful discussions. Next, I appreciate secretaries, Ms. K. Yashima, Ms. K. Ichikawa, Ms. M. Imahori, Ms. R. Nagashima, and Ms. K. Fillson for various kinds of help. At last, I thank many students Dr. Y. Gu, Dr. H. Oki, Mr. Y. Lu, Mr. T. Fukamichi, Ms. A. Mtsumoto, Mr. Y. Tashiro, Mr. Y. Yokota, Mr. A. Kato, Mr. R. Kawakami, Mr. M. Nakamura, Mr T. Yoshino. Mr. K. Hayama, Mr. K. Kono, Mr. O. Osawa. Ms. T. Shimura, Mr. Y. Hayashi, Mr. M. Matsui, Ms. Y. Shirai, and Ms. N. Ulrike for refreshment.

I want to show my greatest appreciation to Prof. Z. Hiroi, Prof. T. Shibauchi, Prof. M. Lippmaa, and Prof. H. Mizokawa for giving me insightful comments in my Ph. D. defense.

This work was supported by Global COE Program “the Physical Sciences Frontier” at the University of Tokyo.

Finally, I would like to thank my family and my friends for support and encouragement through my Ph. D. course.

Hideyuki Kawasoko

Reference

[1] H. Kamerlingh. Onnes, *Leiden Comm.* **120b**, **122b**, **124c** (1911).

[2] M. Tinkham, *Introduction to Superconductivity Second Edition* (McGraw-Hill, New York 1996).

[3] G. Bednorz and K. A. Muller, *Z. Phys.* **B64** 189 (1986).

[4] Kyle M. Shen and J. C. Seamus Davis, *Materials Today* **11**, 14 (2008).

[5] S. Tanaka, *Jpn. J. Appl. Phys.* **45**, 9011 (2006).

[6] J. Bardeen, L. N. Cooper, and J. R. Schrieffer, *Phys. Rev.* **106**, 162 (1957).

[7] W. L. McMillan, *Phys. Rev.* **167**, 331 (1968).

[8] 日本物理学会誌 **66**, 747 (2011).

[9] J. Nagamatsu; N. Nakagawa, T. Muranaka; Y. Zenitani, J. Akimitsu, *Nature* **410**, 63 (2001).

[10] K. Tanigaki, T. W. Ebbesen, S. Saito, J. Mizuki, J. S. Tsai, *Nature* **352**, 222 (1991).

[11] R. J. Cava, B. Batlogg, J. J. Krajewski, R. Farrow, L. W. Rupp, Jr., A. E. White, K. Short, W. F. Peck, Jr., and T. Kometani, *Nature* **332**, 814 (1988).

[12] V. Meregalli and S. Y. Savrasov, *Phys. Rev. B* **57**, 14453 (1998).

[13] A.W. Sleight, J. L Gillson, and P. E. Bierstedt, *Solid State Commun.* **17**, 27 (1975).

[14] K. Luna, P. Giraldo-Gallo, T. Geballe, I. Fisher, and M. Beasley, *Phys. Rev. Lett.* **113**, 177004 (2014).

[15] D. Cox and A. W. Sleight, *Solid State Commun.* **19**, 969 (1976).

[16] S. Tajima, S. Uchida, A. Masaki, H. Takagi, K. Kitazawa, S. Tanaka, and S. Sugai, *Phys. Rev. B* **35**, 696 (1987).

[17] C. Varma, *Phys. Rev. Lett.* **61** 23 (1988).

[18] T. D. Thanh, A. Koma, and S. Tanaka, *J. Appl. Phys.* **22**, 205 (1980).

[19] I. B. Bischofs, V. N. Kostur, and P. B. Allen, *Phys. Rev. B* **65**, 115112 (2002).

[20] T. Thonhauser and K. M. Rabe, *Phys. Rev. B* **73**, 212106 (2006).

[21] Y. Wakabayashi, D. Bizen, H. Nakao, Y. Murakami, M. Nakamura, Y. Ogimoto, K. Miyano, and H. Sawa, *Phys. Rev. Lett.* **96**, 017202 (2006).

[22] K.Inumaru, H. Miyata, and S. Yamanaka, *Phy. Rev. B* **78**, 132507 (2008)

[23] D. E. Cox and A. W. Sleight, in Proceedings of the Conference on Neutron Scattering, Gatlinburg, Tennessee, edited by R. M. Moon (National Technical Information Service, Springfield, VA, 1976).

[24] A. W. Sleight and D. E. Cox, *Solid State Commun.* **58**, 347 (1986).

[25] D. T. Marx, P. G. Radaelli, J. D. Jorgensen, R. L. Hitterman, D. G. Hinks, Shiyou Pei, and B. Dabrowski, *Phys. Rev. B* **46**, 1144 (1992).

[26] Y. Khan, K. Nahm, M. Rosenberg and H. Willner, *Phys. Status Solidi A* **39**, 79 (1977).

[27] M. Oda, Y. Hadika, A. Katsui and T. Murakami, *Solid State Commun.* **55**, 423 (1985).

[28] M. Oda, Y. Hadika, A. Katsui and T. Murakami, *Solid State Commun.* **60**, 897 (1986); Y. Enomoto, M. Oda and T. Murakami, *Phase Trans.* **8**, 129 (1987).

[29] H. Asano, M. Oda, Y. Endoh, Y. Hidaka, F. Izumi, T. Ishigaki, K. Karahashi, T. Murakami and N. Watanabe, *Jpn. J. Appl. Phys.* **27**, 1638 (1988).

[30] J. Ihringer, J. K. Maichle, W. Prandl, A. W. Hewat and T. Wroblewski, *Z. Phys. B* 82, 171 (1991).

[31] E. Climent-Pascual, N. Ni, S. Jia, Q. Huang, and R. J. Cava, *Phys. Rev. B.* **83**, 174512 (2011).

[32] P. Giraldo-Gallo, Y. Zhang, C. Parra, H. C. Manoharan, M. R. Beasley, T. H. Geballe, M. J. Kramer, and I. R. Fisher, arXiv:1407.7611.

[33] S. Uchida, K. Kitazawa, and S. Tanaka, *Phase Transit.* **8**, 95 (1987).

[34] L. F. Mattheiss and D. R. Hamann, *Phys. Rev. B* **28**, 4227 (1983).

[35] S. Tajima, K. Kitazawa and S. Tanaka, *Solid State Commun.* **47**, 659 (1983).

[36] T. Tani, T. Itoh and S. Tanaka, *J. Phys. Soc. Jpn.*, **49**, 309 (1980).

[37] K. Kitazawa, M. Naito, T. Itoh, and S. Tanaka, *J. Phys. Soc. Jpn.* **54**, 2682 (1985).

[38] S. Tajima, S. Uchida, A. Masaki, H. Takagi, K. Kitazawa, S. Tanaka and A. Katsui, *Phys. Rev. B* **32**, 6302 (1985).

[39] T. Itoh, K. Kitazawa and S. Tanaka, *J. Phys. Soc. Jpn.* **53**, 2668 (1984).

[40] T. M. Rice and L. Sneddon, *Phys. Rev. Lett.* **47**, 689 (1981).

[41] E. Jurczek and T. M. Rice, *Europhys. Lett.* **1**, 225 (1986).

[42] D. Yoshioka and H. Fukuyama, *J. Phys. Soc. Jpn.* **54**, 2996 (1985).

[43] A. Bahrotti, A. P. Menushenkov, N. Motta, and J. Puran, *Solid State Commun.* **49**, 887 (1984).

[44] G. K. Wertheim, J. P. Remeika, and D. N. E. Buchanan, *Phys. Rev. B* **26**, 2120 (1982).

[45] C. Chaillout, J. P. Remeika, A. Santro, and M. Marezio, *Solid State Commun.* **56**, 829 (1985).

[46] S. Uchida, S. Tajima, A. Masaki, S. Sugai, K. Kitazawa, and S. Tanaka, *J. Phys. Soc. Jpn.* **54**, 4395 (1985).

[47] S. Sugai, S. Uchida, K. Kitazawa, S. Tanaka and A. Katsui, *Phys. Rev. Lett.* **55**, 426 (1985); *Jpn. J. Appl. Phys.* **24**, 13 (1985).

[48] A. Pretre and T. M. Rice, *J. Phys. C: Solid State Phys.* **19**, 1363 (1986).

[49] P. W. Anderson, K. A. Muttalib, and T. V. Ramakrishnan, *Phys. Rev. B* **28**, 117 (1983).

[50] H. Fukuyama, H. Ebisawa, and S. Maekawa, *J. Phys. Soc. Jpn.* **53**, 1919 (1984).

[51] B. L. Altshuler and A. G. Aronov, *Solid State Commun.* **30,** 115 (1979)

[52] J. M. Graybeal and M. A. Beasley, *Phys. Rev. B* **29**, 4167(1984).

[53] D. Belitz, *Phys. Rev. B* **35**, 1636 (1987).

[54] D. Belitz, *Phys. Rev. B* **36**, 47 (1987).

[55] D. Belitz, *Phys. Rev. B* **40**, 111 (1989).

[56] G. Hertel, D. J. Bishop, E. G. Spencer, J. M Rowell, and R. C. Dynes, *Phys. Rev. Lett.* **50**, 743 (1983).

[57] P. Zubko, S. Gariglio, M. Gabay, P. Ghosez, and J.-M. Triscone, *Annu. Rev. Condens. Matter Phys* **2**, 141 (2011).

[58] S. Gariglio and J.-M. Triscone, *C. R. Physique* **12**, 591 (2011).

[59] H. Y. Hwang, Y. Iwasa, M.Kawasaki, B. Keimer, N. Nagaosa and Y. Tokura., *Nature Mater.* **11**, 103 (2012).

[60] N. Reyren, S. Thiel, A. D. Caviglia, L. Fitting Kourkoutis, G. Hammerl, C. Richter, C. W. Schneider, T. Kopp, A.-S. Rüetschi, D. Jaccard, M. Gabay, D. A. Muller, J.-M. Triscone, and J. Mannhart, *Science*. **317**, 1196 (2007).

[61] A. Gozar, G. Logvenov, L. F. Kourkoutis, A. T. Bollinger, L. A. Giannuzzi, D. A. Muller, and I. Bozovic, *Nature* **455**, 782 (2008).

[62] P. A. Salvador, A.-M. Haghiri-Gosnet, B. Mercey, M. Hervieu, and B. Raveau, *Appl. Phys. Lett.* **75**, 2638 (1999).

[63] K. S. Takahashi, M. Kawasaki, and Y. Tokura, *Appl. Phys. Lett.* **79**, 1324 (2001).

[64] A. Tsukazaki, A. Ohtomo, T. Kita, Y. Ohno, H. Ohno, and M. Kawasaki, *Science* **315**, 1388 (2007).

[65] A. Tsukazaki, S. Akasaka, K. Nakahara, Y. Ohno, H. Ohno, D. Maryenko, A. Ohtomo, and M. Kawasaki, *Nature Mater.* **9**, 889 (2010).

[66] A. Ohtomo and H. Y. Hwang, *Nature* **427**, 423 (2004).

[67] N. Reyren, S. Gariglio, D. Caviglia, D. Jaccard, T. Schneider, and J.-M. Triscone, *Appl. Phys. Lett.* **94**, 112506 (2009).

[68] A. D. Caviglia, S. Gariglio, N. Reyren, D. Jaccard, T. Schneider, M. Gabay, S. Thiel, G. Hammerl, J. Mannhart, and J.-M. Triscone, *Nature* **456**, 624 (2008).

[69] G. Logvenov, A. Gozar, and I. Bozovic, *Science* **326**, 699 (2009).

[70] Y. Tokura and H. Y. Hwang, *Nature Mater.* **7**, 694 (2008).

[71] C. H. Ahn, J.-M. Triscone, and J. Mannhart, *Nature* 424, 1015 (2003).

[72] H. T. Yuan, H. Shimotani, A. Tsukazaki, A. Ohtomo, M. Kawasaki, and Y, Iwasa, *Adv. Funct. Mater.* **19**, 1046 (2009).

[73] K. Ueno, S. Nakamura, H. Shimotani, A. Ohtomo, N. Kimura, T. Nojima, H. Aoki, Y. Iwasa, and M. Kawasaki, *Nature Mater.* **7**, 855 (2008).

[74] J. T. Ye, S. Inoue, K. Kobayashi, Y. Kasahara, H. T. Yuan, H. Shimotani, and Y. Iwasa, *Nature Mater.* **9**, 125 (2010).

[75] K. Ueno, S. Nakamura, H. Shimotani, H. T. Yuan, N. Kimura, T. Nojima, H. Aoki, Y. Iwasa, and M. Kawasaki, *Nature Nanotech.* **6**, 408 (2012).

[76] A. T. Bollinger, G. Dubuis, J. Yoon, D. Pavuna, J. Misewich, and I. Božović, *Nature* **472**, 458 (2011).

[77] J. T. Ye, Y. J. Zhang, R. Akashi, M. S. Bahramy, R. Arita, and Y. Iwasa, *Science* **338**, 1193 (2012).

[78] Y. Yamada, K. Ueno, T. Fukumura, H. T. Yuan, H. Shimotani, Y. Iwasa, L. Gu, S. Tsukimoto, Y. Ikuhara, M. Kawasaki, *Science* **332**, 1065 (2011).

[79] M. Nakano, K. Shibuya, D. Okuyama, T. Hatano, S. Ono, M. Kawasaki, Y. Iwasa, Y. Tokura, *Nature* **487**, 459 (2012).

[80] Web site of “PASCAL CO., LTD” (http://www.pascal-co-ltd.co.jp/solutions/index.html).

[81] S. Kobayashi, F. Komori, Y. Ootuka, and W. Sasaki, *J. Phys. Soc. Jpn.* **49**, 1635 (1980).

[82] 家 泰弘, 「超伝導」 (朝倉書店, 2005).

[83] M. Tinkham, *Phys. Rev.* **129**, 2413 (1963).

[84] S. Kittaka, T. Nakamura, Y. Aono, S. Yonezawa, K. Ishida, and Y. Maeno, *Phys. Rev. B* **80**, 174514 (2009).

[85]Y. Kozuka, M. Kim, C. Bell, B. G. Kim, Y. Hikita, and H. Y. Hwang, *Nature***462**, 487 (2009).

[86] R. Fastampa, M. Giura, R. Marcon, and E. Silva, *Phys. Rev. Lett.***67**, 1795 (1991).

[87] J. M. Kosterlitz andD. J.Thouless, *J. Phys. C Solid State Phys.***6**,1181 (1973).

[88] J. M.Kosterlitz, *J. Phys. C Solid State Phys***7**, 1046 (1974).

[89]B. I.HalperinandD. R. Nelson, *J. Low Temp. Phys.***36**, 599 (1979).

[90] M. R. Beasley, J. E. Mooji, and T. P. Orlado, *Phys. Rev. Lett*. **42**, 1165 (1979).

[91] M. Gabay and A. Kapitulink, *Phys. Rev. Lett*. **71**, 2138 (1993).

[92] R. C. Dynes, A. E. White, J. M. Graybeal, and J. P. Garno,*Phys. Rev. Lett.***57**, 2195 (1986).

[93] N. W. Ashcroft and N. D. Mermin, *Solid State Physics* (Holt,Rinehart and Winston, New York, 1976).